Space Sci Rev (2020) 216:75
https://doi.org/10.1007/s11214-020-00704-8

SIMBIO-SYS: Scientific Cameras and Spectrometer for the BepiColombo Mission

G. Cremonese[1] · F. Capaccioni[2] · M.T. Capria[2] · A. Doressoundiram[3] · P. Palumbo[4] · M. Vincendon[5] · M. Massironi[6] · S. Debei[7] · M. Zusi[2] · F. Altieri[2] · M. Amoroso[8] · G. Aroldi[9] · M. Baroni[9] · A. Barucci[3] · G. Bellucci[2] · J. Benkhoff[10] · S. Besse[11] · C. Bettanini[7] · M. Blecka[12] · D. Borrelli[9] · J.R. Brucato[13] · C. Carli[2] · V. Carlier[5] · P. Cerroni[2] · A. Cicchetti[2] · L. Colangeli[10] · M. Dami[9] · V. Da Deppo[14] · V. Della Corte[2] · M.C. De Sanctis[2] · S. Erard[3] · F. Esposito[15] · D. Fantinel[1] · L. Ferranti[16] · F. Ferri[7] · I. Ficai Veltroni[9] · G. Filacchione[2] · E. Flamini[17] · G. Forlani[18] · S. Fornasier[3] · O. Forni[19] · M. Fulchignoni[20] · V. Galluzzi[2] · K. Gwinner[21] · W. Ip[22] · L. Jorda[23] · Y. Langevin[5] · L. Lara[24] · F. Leblanc[25] · C. Leyrat[3] · Y. Li[26] · S. Marchi[27] · L. Marinangeli[28] · F. Marzari[29] · E. Mazzotta Epifani[30] · M. Mendillo[31] · V. Mennella[15] · R. Mugnuolo[32] · K. Muinonen[33,34] · G. Naletto[29] · R. Noschese[2] · E. Palomba[2] · R. Paolinetti[9] · D. Perna[30] · G. Piccioni[2] · R. Politi[2] · F. Poulet[5] · R. Ragazzoni[1] · C. Re[1] · M. Rossi[9] · A. Rotundi[35] · G. Salemi[36] · M. Sgavetti[37] · E. Simioni[1] · N. Thomas[38] · L. Tommasi[9] · A. Turella[9] · T. Van Hoolst[39] · L. Wilson[40] · F. Zambon[2] · A. Aboudan[7] · O. Barraud[3] · N. Bott[3] · P. Borin[1] · G. Colombatti[7] · M. El Yazidi[7] · S. Ferrari[7] · J. Flahaut[41] · L. Giacomini[2] · L. Guzzetta[2] · A. Lucchetti[1] · E. Martellato[4] · M. Pajola[1] · A. Slemer[14] · G. Tognon[7] · D. Turrini[2]

Received: 12 December 2019 / Accepted: 6 June 2020
© The Author(s) 2020

Abstract The SIMBIO-SYS (Spectrometer and Imaging for MPO BepiColombo Integrated Observatory SYStem) is a complex instrument suite part of the scientific payload of the Mercury Planetary Orbiter for the BepiColombo mission, the last of the cornerstone missions of the European Space Agency (ESA) Horizon + science program.

The SIMBIO-SYS instrument will provide all the science imaging capability of the BepiColombo MPO spacecraft. It consists of three channels: the STereo imaging Channel (STC), with a broad spectral band in the 400-950 nm range and medium spatial resolution (at best 58 m/px), that will provide Digital Terrain Model of the entire surface of the planet with an accuracy better than 80 m; the High Resolution Imaging Channel (HRIC), with broad spectral bands in the 400-900 nm range and high spatial resolution (at best 6 m/px), that will pro-

The BepiColombo mission to Mercury
Edited by Johannes Benkhoff, Go Murakami and Ayako Matsuoka

✉ G. Cremonese
gabriele.cremonese@inaf.it

1 INAF-Osservatorio Astronomico di Padova, Padova, Italy

2 INAF-IAPS, Roma, Italy

3 LESIA, Observatoire de Paris, Université PSL, CNRS, Université de Paris, Sorbonne Université, Meudon, France

Published online: 17 June 2020

vide high-resolution images of about 20% of the surface, and the Visible and near-Infrared Hyperspectral Imaging channel (VIHI), with high spectral resolution (6 nm at finest) in the 400-2000 nm range and spatial resolution reaching 120 m/px, it will provide global coverage at 480 m/px with the spectral information, assuming the first orbit around Mercury with periherm at 480 km from the surface. SIMBIO-SYS will provide high-resolution images, the Digital Terrain Model of the entire surface, and the surface composition using a wide spectral range, as for instance detecting sulphides or material derived by sulphur and carbon oxidation, at resolutions and coverage higher than the MESSENGER mission with a full co-alignment of the three channels. All the data that will be acquired will allow to cover a wide range of scientific objectives, from the surface processes and cartography up to the internal structure, contributing to the libration experiment, and the surface-exosphere interaction. The global 3D and spectral mapping will allow to study the morphology and the composition of any surface feature. In this work, we describe the on-ground calibrations and the results obtained, providing an important overview of the instrument performances. The calibrations have been performed at channel and at system levels, utilizing specific setup in most of the cases realized for SIMBIO-SYS. In the case of the stereo camera (STC), it has been necessary to have a validation of the new stereo concept adopted, based on the push-frame. This work describes also the results of the Near-Earth Commissioning Phase performed few weeks after the Launch (20 October 2018). According to the calibration results and the first commissioning the three channels are working very well.

Keywords BepiColombo · Mercury

[4] Dept. Physics, Univerisity Parthenope, Napoli, Italy

[5] Université Paris-Saclay, CNRS, Institut d'Astrophysique Spatiale, 91405, Orsay, France

[6] Dept. Geosciences, University of Padova, Padova, Italy

[7] CISAS, University of Padova, Padova, Italy

[8] ASI, Roma, Italy

[9] Leonardo spa, Campi Bisenzio, Firenze, Italy

[10] ESA, Estec, Noordwijk, The Netherlands

[11] ESA-ESAC, Madrid, Spain

[12] Space Research Center, Academy of Science, Warsaw, Poland

[13] INAF-Osservatorio di Arcetri, Firenze, Italy

[14] CNR-IFN, Padova, Italy

[15] INAF-Osservatorio di Capodimonte, Napoli, Italy

[16] Dept. Earth Sciences, University Federico II, Napoli, Italy

[17] IRSPS-D'Annunzio University Chieti-Pescara, Chieti, Italy

[18] Dept. of Engineering and Architecture, University of Parma, Parma, Italy

[19] Institut de Recherche en Astrophysiques et Planetologie, Toulouse, France

[20] UFR de Physique, Université Denis Diderot Paris 7, Paris, France

[21] Planetengeologe am DLR-Institut fur Planetenforschung, Berlin, Germany

[22] Institute of Astronomy and Space Science, National Central University, Chung Li, Taiwan

[23] Laboratoire d'Astrophysique de Marseille, Marseille, France

Acronyms

AIV	assembly integration and verification
AMA	absolute model ages
APID	application process identifier
ASI	Agenzia Spaziale Italiana
ASW	application software
AT	along track
BB	broad band
BSW	boot software
CaSSIS	color and stereo surface imaging system
CFRP	carbon fiber reinforced polymer
CPCU	command and process control unit
CT	cross track
CTIA	capacitance transimpedance amplifier
DC	dark current
DN	digital number
DOF	degree of freedom
DPU	data processing unit
DSNU	dark spatial non-uniformity
DTM	digital terrain model
EDDS	ESA ground operation system's data dissemination system
EGSE	electrical ground segment equipment
ESA	European space agency
EEPROM	electrically erasable programmable read-only memory

[24] Instituto de Astrofisica de Andalucia CSIC, Granada, Spain

[25] LATMOS/IPSL, Sorbonne Université, UVSQ, CNRS, Paris, France

[26] Suzhou vocational University, SuZhou, China

[27] SWRI, Boulder, USA

[28] Dept. of Psychological, Humanisti and territorial Sciences, University d'Annunzio, Chieti, Italy

[29] Dept. of Physics and Astronomy, University of Padova, Padova, Italy

[30] INAF-Osservatorio Astronomico di Monte Porzio, Roma, Italy

[31] Center for Space Physics, University of Boston, Boston, USA

[32] ASI, Matera, Italy

[33] Dept. of Physics, University of Helsinki, Helsinki, Finland

[34] Finnish Geospatial Research Institute FGI, National Land Survey, Masala, Finland

[35] Dept. of Sciences and Technologies, University Parthenope, Napoli, Italy

[36] Dept. of Cultural Heritage, University of Padova, Padova, Italy

[37] Dept. of Earth Sciences, University of Parma, Parma, Italy

[38] Dept. Physics, University of Bern, Bern, Switzerland

[39] Royal Observatory of Belgium, Brussels, Belgium

[40] Institute of Environmental and Biological Sciences, University of Lancaster, Lancaster, United Kingdom

[41] Centre de Recherches Pétrographiques et Géochimiques (CRPG), CNRS Université de Lorraine, Vandeuvres-lés-Nancy, France

EMC	electromagnetic compatibility
FE	conversion factor, electrons over energy
FOP	flight operation procedure
FoV	field of view
FPA	focal plane assembly
FPGA	field programmable gate array
FPN	fixed pattern noise
GCP	ground control points
MPO	mercury planetary module
HK	housekeeping
HRIC	high resolution imaging channel
ICU	internal calibration unit
IFoV	instantaneous field of view
IG	inverse gain
IS	integrating sphere
IT	integration time
ITO	indium tin oxide
ITR	integrate then read
LHB	late heavy bombardment
LRM	low reflectance material
MDIS	mercury dual imaging system
ME	main electronic
MTF	modulation transfer function
NECP	near earth commission phase
NESR	noise-equivalent spectral radiance
OB	optical bench
OBCP	onboard control procedures
OBSW	onboard software
OGSE	optical ground support equipment
PDOR	payload direct operation request
PE	proximity electronic
PFM	proto flight model
PPD	pinned photo diode
PR	photo response
PRNU	photo response non-uniformity
PROM	programmable read-only memory
PSF	point spread function
PU	power unit
QE	quantum efficiency
RC	Ritchey-Chretien
RFM	rational function model
RMSE	root mean square error
ROIC	readout integrated circuit
RON	readout noise
RVS	raytheon vision systems
SC	spurious charge
SIMBIO-SYS	Spectrometer and Imaging for MPO BepiColombo Integrated Observatory SYStem
SNR	signal to noise ratio

STC	stereo channel
SVS	stereo validation team
TC	telecommand
TEC	thermoelectric cooler
TIRD	thermal infrared rejection device
TM	telemetry
TVC	thermal vacuum chamber
UT	unit tester
VIHI	visible and near-infrared hyperspectral imaging
VIRS	visible/infrared spectrometer

1 Introduction

The Spectrometer and Imagers for MPO Bepicolombo Integrated Observatory SYStem (SIMBIO-SYS) is a suite of three independent optical heads that will provide images and spectroscopic observations of Mercury's surface. The SIMBIO-SYS instrument on board the Mercury Planetary Orbiter (MPO), one of the two modules of the BepiColombo mission, is composed of HRIC (High Resolution Imaging Camera), STC (STereo Channel), and VIHI (Visible and Infrared Hyperspectral Imager). The scientific objectives at mission level are to obtain a global mapping of the surface with STC and VIHI in the first 6 months of the nominal mission. Both channels will provide data on the surface composition, the surface geology as well as Digital Terrain Models (DTMs) of the entire planet in the first 6 months of the nominal mission. Since the MPO orbit will be less elliptical than the MESSENGER orbit (starting orbits: 480 $\times$ 1500 km vs. 200 $\times$ 15000 km), the spatial resolution of the images at the periherm and at the poles, the main orbit arc used for the global mapping, differs only by a factor of two. The observing strategy of SIMBIO-SYS is based on the global mapping requirement and includes high-resolution images of 20% of the surface (HRIC). In the second 6 months of the nominal mission, STC and VIHI will fill in gaps possibly left in the global mapping. In this phase, VIHI will observe selected regions at a spatial resolution of a factor of four better than during the previous phase. STC will acquire 4 color images of selected regions and, as during the global mapping, will acquire stereo pairs using the two panchromatic filters.

SIMBIO-SYS has been selected in 2004, together with all the instruments on board BepiColombo. Soon thereafter, Leonardo SpA in Florence (Italy) has been selected as the prime contractor of the instrument. It has been funded by two space agencies, ASI (Italian Space Agency) and CNES (French Space Agency) and it is the result of the collaboration between more than 80 scientists and engineers of 12 different countries from all over the world.

It is the first time that a planetary mission has three remote sensing instruments integrated in a system sharing some hardware components. The Main Electronics (ME) and the onboard software are the same, allowing for synergistic management of operations, data handling, and compression of all the acquired data. A single factory provided all the detectors that are similar for the three cameras. From an engineering point of view, the systemic approach to the design has had several advantages:

- the technical management structure allowed the management of the developing and testing phases with the main target of optimizing the overall performance and capabilities of SIMBIO-SYS;
- the integration of the common parts allowed a better control and the optimization of the resources as mass and power;

– mechanical, thermal, and electrical interfaces towards the spacecraft have been handled at a unified level.

From a scientific point of view, the systemic approach with the same management will provide many advantages:

– cross-calibration and co-alignment of the three channels is seamless;
– co-registration and data fusion are enabled;
– common science planning is easier.

On one hand, it adds complexity to the operations and the observing strategy, but, on the other hand, the data of three remote sensing instruments put together will increase the scientific return, as there are no problems of cross-calibration and sharing of the data.

The present work provides an updated summary of the science goals and describes the on-ground calibrations performed at channel and system levels. It provides an overview of the results and the instrument performances. The last sections describe the preparation and the results of the Near-Earth Commissioning Phase (NECP).

2 Science Goals

The SIMBIO-SYS integrated package aims to provide answers, in a coordinated effort with other instruments, such as the thermal infrared spectrometer MERTIS (Hiesinger et al. 2020, this issue), the UV spectrometer PHEBUS (Quemerais et al. 2020, this issue), the laser altimeter BELA (Hussmann et al. 2020, this issue), the X-ray spectrometer MIXS (Bunce et al. 2020, this issue), and the neutron spectrometer MGNS (Mitrofanov et al. 2020, this issue), to almost all the main scientific questions of the BepiColombo mission concerning the Mercury surface and composition, and to provide important contributions to the understanding of its interior and exosphere. The main scientific questions of the BepiColombo mission are detailed in dedicated papers of this volume (Rothery et al. 2020, this issue; Milillo et al. 2020, this issue; Hussmann et al. 2020, this issue); we highlight here those related to the main SIMBIO-SYS science objectives. In the following subsections, the science questions are groupedaccording to the following topics:

– shape and morphology;
– crustal mineralogy;
– geological mapping and stratigraphy;
– volatiles;
– interior;
– Hermean extreme environment;
– exosphere;
– surface changes;
– opportunity science.

Most of the scientific goals are rooted within one of these topics, but some of them involve several topics that will be highlighted when needed.

2.1 SIMBIO-SYS Scientific Objectives – Topography and Morphology

The SIMBIO-SYS instrument will devote many measurements to the global topography of the planet. In particular, the STC channel will deliver a global DTM with a grid resolution

better than 120 m/pixel, while HRIC will provide updates of the reference system and prime meridian by selecting and observing specific topographic targets during the mission. Both channels will concur in creating a global context for the BELA range measurements between the spacecraft and the Hermean surface. All these observations are fundamental to the comprehension of Mercury interior and surface. Surface morphology will be analyzed in two dimensions at different scales and resolution using STC and HRIC images; in addition, 3D patterns will be delivered by using the STC stereo datasets. The STC global stereo mapping and the HRIC targeted high-resolution images will represent an important step forward in the geomorphological characterization of the Hermean surface, also providing topographic and high-resolution information on the southern hemisphere, less covered by MESSENGER. Geomorphological analyses will be mainly devoted to understanding planetary evolution, by looking at the current state of the surface. In the case of Mercury, this implies answering to the following questions, partly raised by MESSENGER and reported in Rothery et al. (2020, this issue):

– what are the history and mechanisms of effusive and explosive eruptions;
– what is the nature, causes, and timing of tectonic features;
– which are the processes related to impact cratering and post-impact modifications on Mercury?

The surface of Mercury has been proven to be almost completely covered by secondary crust, either pertaining to the smooth plains or to the inter-crater plains, which are the most extensive units of Mercury surface (Denevi et al. 2013, 2018; Mancinelli et al. 2015). This means that multiple effusive events have lasted billions of years. Indeed, the oldest inter-crater plains seem to have been emplaced soon after the Late Heavy Bombardment (LHB) (Marchi et al. 2013), extensive formation of smooth plains has vanished at around 3.5 Gy (Byrne et al. 2016) and localized effusions have lasted until the recent past (e.g. Rachmaninoff basin, Prockter et al. (2010)).

The general framework, provided by the MESSENGER data, requires recognizing, through morphological and color boundaries, as well as crater chronology, the different effusive events to constrain the magmatic evolution, the effusion rates through time and the physical properties of the lavas. STC stereo and color images are needed for distinguishing the different magmatic units (either effusive or intrusive, if present) and Atheir related Absolute Model Ages (AMA), whereas HRIC high-resolution and color images would detect potential volcanic sources, dikes, lava fronts and lava flow morphologies, shading light on their physical properties and mechanisms of emplacement (lava sheets vs. inflation). Whereas the sources of the effusive lava flows have not yet been observed, the pyroclastic deposits are often associated to distinct vents, showing locally a compound structure indicating multiple events (Rothery et al. 2014).

However, the different events associated to any single source and their variegation around the planet have not been yet surveyed, hence becoming a pivotal objective of the HRIC targeted high-resolution acquisitions and STC DTMs. Explosive volcanism is thought to be successive to the effusive one, which in turn should have been mostly extinct because of the competing contractional cooling of the planet (Goudge et al. 2014; Thomas et al. 2014b). It is however likely that pyroclastic volcanism was at least coeval with the more localized effusions characterizing the late geological history of the planet, although the connection between the two kinds of volcanism has not been yet explored. In addition, the relation between volcanic activity, either explosive or effusive, and tectonism is not yet well understood, because of timing uncertainties on both geological units and structures and the lack of high-resolution images (in particular on the southern hemisphere) able to constrain the overlapping and cross-cutting relationship among different geological features.

STC aims to provide the broad view and HRIC the needed details to determine relative ages among the different geomorphological units and features.

Mercury tectonism has still open questions on the geodynamic controlling factors and on fault mechanics driving lobate scarps nucleation and propagation. Although it is generally accepted that Mercury global tectonism is dominated by radius contraction (e.g. Di Achille et al. (2012); Byrne et al. (2014)), the fault arrangement and geometries suggest that other geodynamic processes as tidal despinning (Klimczak et al. 2015) and mantle convection (Massironi et al. 2015) might have played an important role during the Hermean geological evolution. Most uncertainties concern the timing of fault nucleation and propagation: several major fold and thrust belts were well developed at around 3.7 Ga (Giacomini et al. 2015; Galluzzi et al. 2019), i.e. in the very early stage of global contraction predicted by the thermal models, if not before. On the other hand, only minor faulting, unquestionably due to radial contraction, have lasted up to recent times (<100 Ma) (Banks et al. 2015; Watters et al. 2016). The low dip angles of fault planes (as small as 7-10°) measured on deformed craters along lobate scarps (Galluzzi et al. 2015, 2019) and/or inferred large frontal thrusts bounded by long lateral ramps (Rothery and Massironi 2010) pose serious question marks on Mercury crustal mechanics. In fact, critical taper principles should not allow slip on such low dipping angles, unless invoking fluid overpressure or ductile behavior along the shear zones. Both these processes can be favored by magmatism and related gas and/or magma injections within fault zones, but this is still to be proven by direct observations. Low dipping thrust faults, if confirmed throughout the planet, would imply also additional radius contraction with respect to the 7 km derived by MESSENGER data (Byrne et al. 2014); this would require a revision of the existing thermal models.

Such geodynamic and geomechanical conundrums can be solved if fault geometries, kinematics, and timing will be globally constrained through STC global DTMs (not affected by illumination bias) and high-resolution observations of fault systems, including their kinematics, mutual cross-cutting relationship, and stratigraphic relationship with volcanic units. Finally, nucleation of large and minor fault systems has been recently proposed to be controlled by rheological boundaries of the crust either at the rim-infill contact of middle (Fegan et al. 2017) and large size basins or at the boundaries of the high-Mg region (Galluzzi et al. 2019). To further test this hypothesis, additional observations at high-resolution and DTMs coupled with compositional and geophysical data are required.

Differing from the lunar evolution, on Mercury, the primary crust may have been a thin carbon rich layer, which was immediately covered by volcanic emplacements giving rise to the early crust (Denevi et al. 2018). Hence the early formed basin was rapidly buried by lavas and the LHB impacts easily triggered volcanic infilling within the newly formed basins (Marchi et al. 2013), which indeed appear with an uneven distribution, less uniform than on the Moon (Fassett et al. 2012). In addition, post-impact deformations within basins were probably deeply affected by the global tectonism and volcanic emplacements and the low viscosity of a Mg-rich mantle should have favored, through time, the uprising of magma on plumping systems opened by impact craters of various sizes. This means that the interplay between impact cratering, volcanic emplacement, and tectonism on planet Mercury has been exceptionally intimate. This framework, delineated by MESSENGER findings, poses a series of challenging objectives to be faced by the BepiColombo mission such as: inferring the location of old buried basins and their control on fault nucleation and propagation; understanding, how global geodynamic strain and volcanic emplacements affect the post-impact deformations within basins; distinguishing between impact melts and lava infilling within crater floors.

Finally, the higher impact velocities on planet Mercury might require refinements in the distinction of the different impact morphologies and makes it more difficult to discriminate

among primary and secondary craters for dating purposes. SIMBIO-SYS will contribute to clarifying all these points with STC, which will give the needed synoptic view and the 3D reconstruction of middle and large-size impact morphologies to be related to gravity and crustal thickness maps, with VIHI, which should retrieve the composition of the smooth materials infilling basins and craters, and, with HRIC, which unravels details enabling the discrimination among impact and volcanic-related deposits and morphologies.

2.2 SIMBIO-SYS Scientific Objectives – Crustal Mineralogy

BepiColombo aims at providing information about the origin and evolution of Mercury that can be retrieved by answering to a series of main questions extensively discussed in Rothery et al. (2020, this issue):

- what is the mineralogical composition of the crust?
- what are the history and mechanisms of crustal formation?
- what can we deduce about processes of magmagenesis?

The elemental composition derived by MESSENGER XRS (Nittler et al. 2011) and the river-like appearance of lava flows on the north-polar region (Head et al. 2011; Byrne et al. 2013) have pointed out a Mg-rich crust, mostly made up of wide picritic-basanitic deposits represented by the dominant smooth and inter-crater plain units. In between these units, the graphite-bearing Low Reflectance Material (LRM) excavated from depths by major impacts is exposed; it is thought to be representative of Mercury early crust (Denevi et al. (2018) and references therein). In addition, MESSENGER GRS and XRS data have shown at least 6 geochemical regions indicating different mantle magma sources evolving through time (Weider et al. 2015; Peplowski et al. 2015; Lawrence et al. 2015). Despite such accurate general description, no direct mineralogical information has been provided by MESSENGER MASCS spectra, but for some absorption around 0.6 μm and a change of spectral slope at 1 μm, interpreted as possibly related to Cr-rich pyroxenes in the bulk rock of hollow-rich sites (Lucchetti et al. 2018). The difficulties in retrieving mineralogical information are likely due to the low iron content in silicates of the Mercury crust and the enhanced space weathering effect on Mercury surface, in addition to limited S/N and to the shorter spectral range of MASCS in the visible and near infrared (300-1450 nm). The VIHI hyperspectral imaging system, with its improved wavelength range of acquisition up to 2.0 μm, a S/N $>$ 100, and a resolution $<$500 m/pixel (and even better than 100 m/pixel in targeted areas), should be able to partly overcome such drawbacks and, together with the IR spectra of MERTIS (Hiesinger et al. 2020, this issue), provide the mineralogical assemblages information on effusive and explosive deposits and on potential intrusive bodies in order to infer Mercury magma-genesis and consequent crustal formation and evolution. Besides the distinction among volcanic products, SIMBIO-SYS will also have the goal of disentangling between impact melts and lava flows within crater floors by using color and spectral imaging. Such a distinction, which remained partly elusive to the MESSENGER instruments, will be essential in revealing volcanic sources of different ages or assessing volumes of melts produced by impacts. Metamorphic products from impacts (e.g., diaplectic glasses) as well as from intrusive contacts and related matosomatism (sulfides) can be investigated using the lower wavelengths of the VIHI hyperspectral channel.

The presence of metallic silicon alloys, hints of possible smelting reactions between magma and the primary crust of graphite (McCubbin et al. 2017) and of a specific optical maturation, will also be investigated thanks to the infrared part of VIHI spectra (see Rothery et al. 2020, this issue, for further discussion).

2.3 SIMBIO-SYS Scientific Objectives – Volatiles

The MESSENGER mission revealed that Mercury has a surface concentration of volatiles, unexpectedly comparable to that of Mars, despite its proximity to the Sun. Hence, understanding the history of volatile exhalation and recycling through the Mercury surface has become a priority target for BepiColombo and implies morphological and compositional analysis aimed at answering to the following main questions (Rothery et al. 2020, this issue):

– what are the characteristics of Permanently Shadowed Regions (PSR);
– what is the nature and expression of volatiles involved in volcanic eruption and other degassing activities?

MESSENGER has provided evidence of ice-bearing deposits within radar-bright PSRs on the Mercury north polar region (Lawrence et al. 2013). These deposits appear bright and bordered by dark, possibly organic materials (Chabot et al. 2014) and are thought to be derived from comets or volatile bearing asteroids impacted on Mercury surface. Nonetheless, recycling of volatiles related to planet outgassing and/or solar implantation, although considered less probable, are not yet excluded (Chabot et al. 2018). Indeed, the composition of such deposits is still not known, as well as their distribution on the whole planet. SIMBIO-SYS will play an important role in determining the nature and extent of polar deposits. The solar illumination conditions on Mercury are not those of a point source at infinite distance (parallel rays) but of an extended source at finite distance (diverging beams). This means that the projected shadow is bordered by a blurred transition area (penumbra), whose dimension depends on the apparent size of the Sun. This will allow SIMBIO-SYS HRIC and STC panchromatic imaging and VIHI reflectance spectroscopy in penumbra conditions. Hence, SIMBIO-SYS, as a whole, will provide a systematic survey for evaluating the extent of PSRs, the distribution of the hosted polar deposits, and the reflectance spectra of their penumbras.

Among the most surprising findings of the MESSENGER mission are hollows which are rimless flat-floored depressions, tens of meters wide, in general found on inner walls, floors, and central peaks of craters (Blewett et al. 2011, 2014; Thomas et al. 2014a). Often clustered in wide areas and constantly associated to spectra two to three times brighter than the surroundings, they are thought to be expressions of volatile depletion which might be still ongoing, although no evidence of active widening of hollows have been gathered so far. Their composition is still unknown although the Mercury Dual Imaging System (MDIS) multispectral data have indicated an absorption band at around 600 nm and a change in slope towards 1000 nm, which could indicate the presence of both sulfides and bedrock basaltic minerals (Vilas et al. 2016; Lucchetti et al. 2018). The data of interest for the study of hollows were those acquired by the Visible/InfraRed Spectrometer (VIRS), a point spectrometer with two linear array detectors, one covering the visible from 300 nm to 900 nm and a near-infrared detector covering 900 nm to 1450 nm, both at spectral resolution of 5 nm (McClintock and Lankton 2007; Izenberg et al. 2014). However, the data of the near-infrared detector ($900 - 1450$ nm) are known to be noisy (Besse et al. 2015), hence, the spectral behavior of hollows above 900 nm was not well studied. In this context, VIHI will improve the study of these features because it works in a wavelength range of $400 - 2000$ nm at spectral resolution of 6 nm. This extended spectral range coupled with the two other observing channels (STC and HRIC) will allow a detailed study of the spectral behavior of the hollows. As for the case of hollows, the compositional nature of the pyroclastic deposits has not been revealed yet (Kerber et al. 2009; Goudge et al. 2014). In this case, it will be important for VIHI to constrain the mineralogical composition of the deposits and the regions of their

vents for detecting minerals of possible hydrothermal genesis like sulfides, or identifying material derived by the sulphur and carbon oxidation which has been invoked to explain high Ca/S ratios and C depletion above faculas (Weider et al. 2016).

Other minor evidence that has been suggested as potential indication of a volatile-rich surface are down-slope streaks (Malliband et al. 2019) and the degradation of ejecta blocks in 1-100 km scales (Wright et al. 2019), but these observations definitely need HRIC to be verified.

2.4 SIMBIO-SYS Scientific Objectives – Stratigraphy and Geological Mapping

Stratigraphy and geological maps are the main tools to understand the geological evolution of the planetary crust. Hence, the science objectives reported in the former sections can be synthesized in stratigraphic charts and geological maps being able to provide information on geomorphology, stratigraphy, and composition of the Mercury crust. Particularly relevant in this case will be the identification of geological units and stratigraphic markers by combining the information of all the SIMBIO-SYS channels. The data provided by the three channels will allow to define geological units and sub-units, including the stratigraphic location of LRM, that will help obtain insights on

- the evolution of the volcanic effusions, in terms of composition and mode of emplacements;
- the stratigraphic relationship between major impacts and lava emplacements;
- the timing relation between tectonic deformations and volcanic and impact events;
- the link between basin and global tectonism;
- the structural environment and stratigraphic positions of the sources of hollows.

2.5 SIMBIO-SYS Scientific Objectives – The Interior

The global shape of the planet, retrieved by STC at less than 120 m/pixel, is pivotal for assessing information about its interior, from the extent and physical state of its core to the relationships between the mantle and the crust in terms of mutual thickness, strength, and isostatic compensation. Radio tracking of the MESSENGER spacecraft, providing the static gravity field of Mercury, together with Earth-based radar measurements of Mercury's spin properties and MESSENGER radio tracking and laser altimeter measurements, has revealed a core of about 2000 km in radius and about 440 km thick silicate shell (mantle + crust) (Margot et al. 2012; Hauck et al. 2013; Mazarico et al. 2014; Stark et al. 2015). Based on the MESSENGER radio science data, Genova et al. (2019) suggest that Mercury has a solid inner core with a radius of at least 600 km. SIMBIO-SYS HRIC, together with MORE and ISA (Iess et al. 2020, this issue), will contribute to the determination of the polar moment of inertia of the whole planet and of the silicate shell, with the aim to characterize the size and density of the crust, shell, molten outer core, and likely solid inner core. In particular, HRIC will target about 50 surface features, twice during the mission, contributing to the determination of the angle between the spin and the orbital axes. Due to these measurements, HRIC will be also able to assess the amplitude of the physical librations in longitude. This will enable the retrieval of the fractional polar moment of inertia of the outer layers that constrains the depth of the mantle and the crust. Indeed, if Mercury core is still to be well constrained, much more can be done to assess crustal-mantle boundary. Based on the MESSENGER data, the thickness of the crust has been estimated to be on average between 20 km and 50 km. It shows substantial variation, with the crust being thicker at low

northern latitudes and thinner (15-30 km) at the high northern smooth plain and at major impact basins, such as Caloris, Odin Budh, Borealis, and Rachmaninoff (within the inner peak ring) (Smith et al. 2012; Padovan et al. 2015; Phillips et al. 2018; Beuthe et al. 2020). Based on MESSENGER geochemical data and gravity and topography maps, Beuthe et al. (2020) show that the crustal thickness variations correlate with lateral variations in mantle melt production.

However, very limited data have been provided by MESSENGER about the southern hemisphere and direct information about potential mantle inhomogeneities and the relationship between geochemical terrains or tectonic features (isolated lobate scarps, fold and thrust belts, long-wavelength undulation) and Mercury interior is still lacking. By contributing to the determination of obliquity and rotation variations of the outer silicate shell of Mercury, HRIC observations will complement the gravity information retrieved by the synergistic action of ISA and MORE and the surface topography provided by STC and BELA in order to reach BepiColombo's goal to characterize the interior structure of Mercury from the inner core to the lithosphere and crust. It will also contribute to establishing the degree of isostatic compensation of different surface features over the entire planet.

An additional HRIC contribution to the comprehension of Mercury geophysics will be the more accurate measurement of the planet's rotational period from optical tracking of surface landmarks. This will be important in the quest of understanding how and when Mercury was captured in the 3:2 spin-orbit resonance (Hussmann et al. 2020, this issue).

2.6 SIMBIO-SYS Scientific Objectives – Hermean Extreme Environment

The Hermean harsh environment is determined by an enhanced space weathering regime and an extreme variability of insolation and temperatures over time and from one location to another. In particular, the effect of reddening and darkening over time due to space weathering has been estimated to be four times that on the Moon (Braden and Robinson (2013)). The SIMBIO-SYS strategy to investigate space weathering will be based on: (i) understanding the relationship between mineralogical composition and environment properties, by characterizing material response and regolith properties (e.g., texture, thickness, reflectance properties, albedo) at different locations and comparing the data with independent mineralogical and elemental measurements from MERTIS, MIXS, and MGNS; (ii) measuring surface reflectance of heavily gardened regions with the highest spatial resolution allowed by all the three channels (i.e., <120 m/pixel for STC; <480 m/pixel for VIHI, <12 m for HRIC). During these observations, particular attention will be paid to regolith glasses, which can be attributed to quenching, impacts, and weathering. Glasses can show diagnostic absorption in the VNIR due to the presence of transitional elements, e.g., Fe_2^+, and in the MidIR due to the diagnostic absorption around 10 μm (e.g., Carli et al. (2016), Carli et al. (2018), Morlok et al. (2020)).

Insolation and high temperatures on Mercury can trigger volatile depletion, produce regolith through thermal stress and/or volatile release, and elastically change the crystal cells and related spectral response of the minerals from one location to another and over time (in particular, in the thermal infrared wavelength ranges, Helbert et al. (2013)). The first two effects will be surveyed on targeted features with HRIC, and the second effect will be tested with specific acquisitions in concert with MERTIS at different latitudes, longitudes, and over time.

2.7 SIMBIO-SYS Scientific Objectives – Exosphere

Some of the main elements in the Hermean exosphere are Na, Mg, and Ca, each of them displaying a different behavior, indicating possible different source and transport mecha-

nism. In particular, Na shows a dawn/dusk asymmetry (Schleicher et al. 2004) and some features varying along the Mercury's year (Leblanc and Johnson 2010), Ca presents a strong decreasing gradient from dawn to dusk, while Mg shows a similar but less pronounced gradient. The release process is thought to be mainly photon stimulated desorption in the case of Na, whereas Mg and Ca need more energetic processes such as impact vaporization. Whatever the release processes are (micrometeoroids and photons impacts, ion sputtering, thermal release, potential intrinsic volatile exhalation), most of the exospheric particles are thought to remain close to the source region (Milillo et al. 2020, this issue). In the case of Na there is some evidence for a day-night migration in the exosphere. This is why the nature of surface releases determined by SERENA-STROFIO (Orsini et al. 2020, this issue) and PHEBUS (Quemerais et al. 2020, this issue) will be related also with the SIMBIO-SYS mineralogical and physical mapping of the surface.

In addition, particularly effective will be the off-nadir limb observations, where the composition of the exosphere can be directly surveyed also by VIHI.

2.8 SIMBIO-SYS Scientific Objectives – Surface Changes

BepiColombo will have the unique chance of recording potential surface changes occurring since the MESSENGER mission or during the BepiColombo mission itself. This goal will be pursued by HRIC on the following specific targets (some of them to be previously detected through the synthetic view of the STC image mosaics):

- fields of hollows, to verify their possible ongoing enlargement by volatile depletion;
- pyroclastic deposits and vents, to verify possible ongoing activity;
- ejecta blocks, to verify their possible degradation through thermal stress and/or ablation of the volatile component;
- slope streaks and other gravitational features, to evidence their possible current activity and eventually identify their triggering agents (impacts, volatile sublimation, seismic activity);
- new impact craters and associated ejecta, to analyze the impact processes on Mercury;
- the site where the MESSENGER orbiter impacted, to study the weathering of the potentially exposed fresh material.

2.9 SIMBIO-SYS Scientific Objectives of Opportunity

SIMBIO-SYS will take the opportunity of observing with its three channels any Solar System body (e.g., comets or asteroids) which may eventually be observed, while BepiColombo will orbit around Mercury. During the nominal mission, it will be possible to ask for off-nadir pointings that may be used to observe a comet as it happened for the MESSENGER mission, when it observed comet ISON in November 2013.

3 Instrument Description

SIMBIO-SYS consists of three optical heads and common Main Electronics (ME), as it will be described in the following sections. The two channels STC and VIHI share the same structure and have been assembled together, including detectors and Proximity Electronics, while HRIC and ME have been mounted in the spacecraft separately (see Fig. 1).

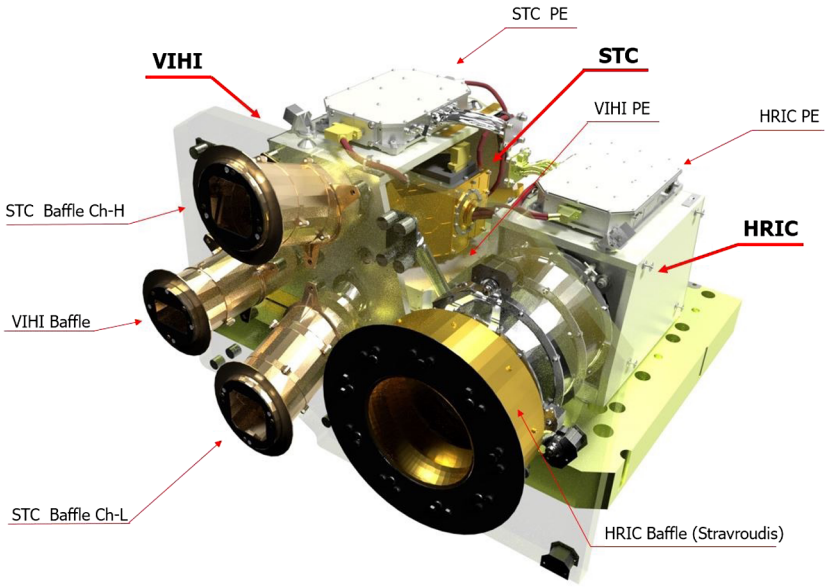

Fig. 1 The three channels together representing SIMBIO-SYS, including the Proximity Electronics (PE)

3.1 HRIC Description

HRIC is the high-resolution multi-color imager within SIMBIO-SYS. The main drivers for the HRIC design were the strong constraints in terms of mass and volume and good optical quality in the harsh thermal environment of the Mercury orbit. The last issue was particularly critical due to the high temperature of Mercury's surface, the gradients within the instrument caused by the environment, the S/C thermal conditions, and the variability in time of these conditions. The instrument design also had to cope with the requirements to reach a ground-sampling distance of the order of 6 m/pixel at the periherm, from 16° latitude North up to 25° latitude South, and to have a Signal to Noise Ratio (SNR) of the order of 100.

3.1.1 Optical Design

The HRIC layout is based on a catadioptric optical design and consists of a modified Ritchey-Chretien (RC) configuration with a dedicated corrector (see Fig. 2). Both mirrors have hyperboloid profiles and are coupled with three corrector lenses aimed at correcting the astigmatism and the FoV curvature aberrations of the RC configuration. The design of the HRIC telescope has been driven by the possibility to achieve the required alignment of the optical elements by means of optomechanical tolerances only. A dedicated fine alignment was required only for the secondary mirror to reach the defined focus position and for the detector, which could be translated and tilted to achieve the best fitting of the focal plane position within the entire field of view. The optical configuration has been optimized minimizing the diameter of the secondary mirror, to reduce the light losses due to central obscuration. A 30% (in diameter) relative obscuration between primary and secondary mirrors has been achieved to provide a good energy transfer to the telescope exit pupil. The instrument has a focal length of 800 mm and is equipped with a dioptric image corrector adapting the FoV to a 2048 x 2048 pixels detector with a pixel size of 10 µm. The focal ratio

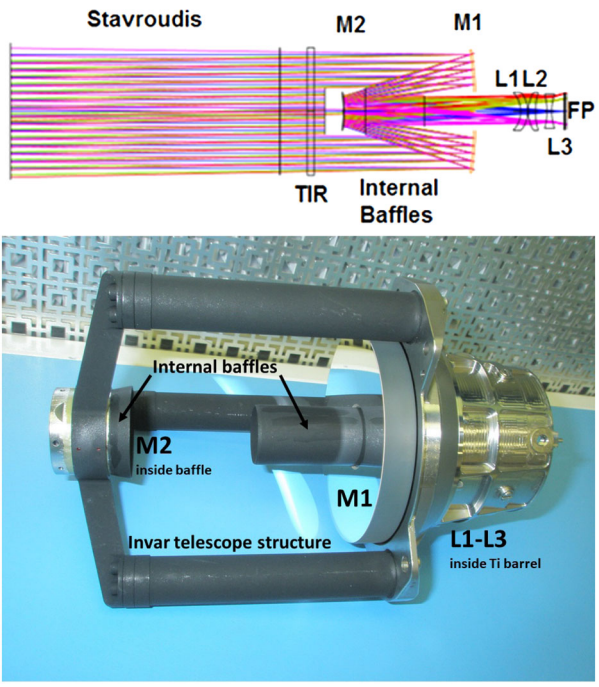

Fig. 2 HRIC optical layout and telescope optomechanics. The Ritchey-Chretien configuration includes primary and secondary mirrors (M1 and M2) and a corrector of three lenses (L1 to L3) close to the Focal Plane Assembly (FPA) which includes a window with filters (here included in the FPA). Two lines between M1 and M2 give the position and diameter of the internal baffles. The position and dimensions of the external baffle (Stavroudis) and the TIRD filter are also given (see text for more details). The Invar structure (dark grey) and the Titanium barrel (on the right) supporting the corrector are clearly visible in the picture

Table 1 Main optical parameters of HRIC

Parameter	Description
Optical concept	Modified Ritchey-Chretien with hyperboloid mirrors and 3 spherical lenses for dioptric correction
Observation strategy	Snapshot or push-frame
Maximum FoV (across track)	1.47°
IFoV	12.6 µrad
Focal length	800 mm
Focal ratio	F/8.9
Optical distortion	0.06%
Optical MTF (at Nyquist frequency)	0.4-0.37 (across the FoV)
Spectral range	400-900 nm
Pupil size	89 mm
Detector type	SiPIN CMOS
Full well	90300 electrons
Quantum efficiency 450 / 850 nm	91% / 83%
Pixel size	10 µm (100% fill factor)
A/D conversion	14 bits/pixel

is F#8.9, to be diffraction limited at 400 nm and to optimize radiometric flux and overall mechanical dimensions; the main optical parameters are reported in Table 1.

To compensate the thermomechanical distortions coming from the high thermal gradient, specific materials have been selected: fused silica has been used for all dioptric and catoptric elements, whereas Invar has been adopted for the telescope mechanical structure and Titanium for the lense supports, spacers, and Focal Plane Assembly (FPA) mechanics. A Carbon Fiber Reinforced Polymer (CFRP) external structure forms an envelope for the internal telescope structure and acts as the mechanical I/F with the S/C optical bench. To reduce the thermal gradients on the optical elements, two non-standard solutions have been adopted: a Thermal Infrared Rejection Device (TIRD) filter and an external baffle properly designed to reject the out-of-field radiation (Cucciarre' 2013; Friso 2010). The TIRD, with a transmitted-wavefront error RMS $\leq$ 230 nm, is placed at the entrance of the instrument. This filter is made of a BK7-G18 substrate with Indium Tin Oxide (ITO) coating with high transmittance in the HRIC spectral range (>80% in the full range, >90% in the 450-770 nm range) and low transmittance at longer wavelengths (< 5% above 2 μm), also due to high reflectivity (>60% above 2 μm). The TIRD filter allows the limitation of the thermal radiation from the target, as Mercury surface easily reaches 700 K, and the gradients within the telescope that would worsen the optical quality due to thermoelastic effects. The external baffle differs from the usual black-coated cylindrical baffle. Based on the Stavroudis geometrical concept (Stavroudis and Foo 1994), the baffle allows to reflect back the out-of-field radiance from the Mercury surface. It uses highly reflective hyperbolas and elliptical surfaces to reject the incoming radiation misaligned with respect to the optical axis. As it reaches high temperatures, it is mechanically and thermally decoupled from the telescope.

3.1.2 Focal Plane Assembly

The small heliocentric distance and the hot Hermean surface make the environment harsh for the BepiColombo payload. The high radiation dose and the high temperature required to select an intrinsic radiation hardness detector based on the CMOS technology. It is a global shutter SiPIN CMOS 2048×2048 with 10- μm pixels developed by Raytheon Vision Systems (RVS). The detector is integrated with a Peltier device aimed at controlling the detector temperature at the nominal value of -5 ± 0.1 °C in order to maintain stable electrical performance. STC uses the same type of detector and one of the SIMBIO-SYS spare models has been used for the Colour and Stereo Surface Imaging System (CaSSIS), the stereo camera on board the ExoMars Trace Gas Orbiter mission (Thomas et al. 2017).

The sensor was designed to achieve high sensitivity as well as low readout noise ($< 100e^-$) for space-based, low-light conditions. It must also maintain its performance in a total ionizing dose environment up to 70 kRad (Si) as well as resistance to Single Event Effects, such as latch-up and single-event upset. For CMOS detectors, the readout of the charge from each pixel is done by readout electronics integrated into the pixel itself. It means that it is able to select windows on the detector, to select filters and detector areas and to perform binning of 2×2 or 4×4 pixels. The on-chip windowing allows lower readout time if a fraction of the detector has to be acquired. The detector and its control, readout, and signal digitization electronics, which is placed in a small box mechanically fixed to the top of the telescope CFRP structure, allow snapshot image acquisition with a minimum integration time around 400 ns and full frame readout time below 1 s, with an integration-then-read approach. The FPA integrates a butcher-block filter deposited onto the detector window, also aimed at contamination control during the Assembly Integration and Verification (AIV) following the design given in Fig. 3.

A panchromatic filter (400-900 nm) provides the highest signal-to-noise images, while three band-pass filters (with central wavelengths at 550, 750, and 880 nm and with 40-nm

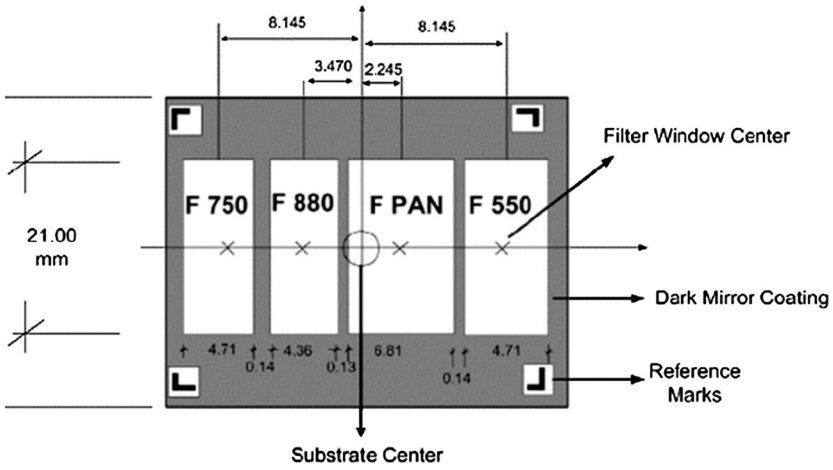

Fig. 3 Design of the detector window including the dimensions of the filters deposited onto the window. Dimensions are in mm. Once in the telescope optical path, the filters are projected on 4 strips on the detector, with dimensions of 384 × 2048 (F750, F880, and F550) and 640 × 2048 pixels (FPAN). The four filter strips are separated by three narrower strips (85 × 2048 pixels) below the absorbing mask

bandwidth) allow the acquisition of color images. The filters are deposited directly on the detector window, in four strips separated by stripes of an absorbing mask which prevents ghosts and well separates different filter areas on the detector. Typical integration times constrained by the S/C motion (i.e., to avoid smearing) are between 0.5 and 7 ms, depending on the position along the orbit and on the filter used. Table 2 summarizes the measured filter characteristics, depending on the observation geometry. The results are very close to specifications.

3.1.3 Observing Strategy

HRIC will operate during the BepiColombo nominal mission to perform targeted high-resolution observations of specific areas of interest, which will be selected according to the scientific analysis and questions mentioned in Sect. 2 and on the data acquired from STC and/or VIHI in the first phase (global coverage during the first six months of the mission). We expect to observe up to 20% of the Mercury surface through selected observations. In principle, HRIC will operate in a wide range of true anomalies of Mercury, i.e., in a wide range of solar incidence angles and latitudes, that will be taken into account according to the specific scientific objective of the observations (e.g., albedo features study, tectonic structure detection and morphology, radiance vs. phase angle). Due to the limited FoV and swath, images acquired in one orbit are not contiguous with images acquired in the following orbit; longitude coverage of an area of interest shall be completed after an entire planet rotation or by tilting the S/C and needs to be carefully planned. Latitude coverage is more easily obtained with a push-frame approach. An example of HRIC observation parameters are reported in Table 3.

HRIC will routinely operate in the PAN mode and full spatial resolution, acquiring in push-frame only the detector area corresponding to the PAN filter. Full color mode is also possible, by acquiring in push frame the four filter windows, allowing the acquisition of the same region in the four filters. In the latter case, the images acquired in F550, F750, and F880 filters will be 2×2 binned, due to the maximum allowed detector readout rate.

Table 2 HRIC filter characteristics; CT means Cross Track, AT means Along Track. The Integration Times (IT) depend from the expected SNR during the nominal phase. T_{peak} is maximum transmittance in the filter band and T_{outave} the average value of transmittance out of the filter band

Filter ID	Spectral and optical characteristics	Filter size on detector [px]	FoV (CTxAT)	IT [ms]
FPAN	Central wl: 652.3 nm FWHM: 504.9 nm $T_{peak} = 98.6\%$ $T_{outave} = 0.018\%$	640 × 2048	0.46° × 1.47°	0.5-3.5
F550	Central wl: 549.3 nm FWHM: 40.4 nm $T_{peak} = 99.1\%$ $T_{outave} = 0.013\%$	384 × 2048	0.25° × 1.47°	1-7
F750	Central wl: 752.9 nm FWHM: 39.6 nm $T_{peak} = 99.7\%$ $T_{outave} = 0.012\%$	384 × 2048	0.25° × 1.47°	1-7
F880	Central wl: 880.1 nm FWHM: 39.8 nm $T_{peak} = 98.9\%$ $T_{outave} = 0.009\%$	384 × 2048	0.25° × 1.47°	1-7

Table 3 HRIC observation parameters in the PAN filter for the first aphelion MPO orbit around Mercury. In this case, the periherm argument is at 16° N latitude, while the south pole case is considered at 83° S latitude

Parameter	Periherm	Pole
S/C altitude [km]	480	966.7
Pixel on ground [m]	6.0	12.1
Swath CT [km]	12.3	24.8
Swath CT [°]	0.30	4.78
Swath AT [km]	3.8	7.7
Swath AT [°]	0.09	0.18

HRIC can also acquire stereo pairs thanks to the possibility to observe the same surface area with different viewing angles in different orbits. Being rigidly integrated on the S/C, off-nadir pointing may be needed to acquire the target by a roll or a pitch of the S/C during the same orbit or the subsequent one. These special pointings need to be carefully planned as they affect the nominal S/C attitude which implies nadir pointing of all remote sensing instruments.

3.2 STC Description

STC represents one of the first push-frame stereo cameras on board a planetary mission. Based on a new concept, STC integrates the compactness of a single-detector telescope with the photogrammetric capabilities of bidirectional cameras. Two separate incoming optical paths oriented at ±20° with respect to nadir allow the instrument to acquire images of the

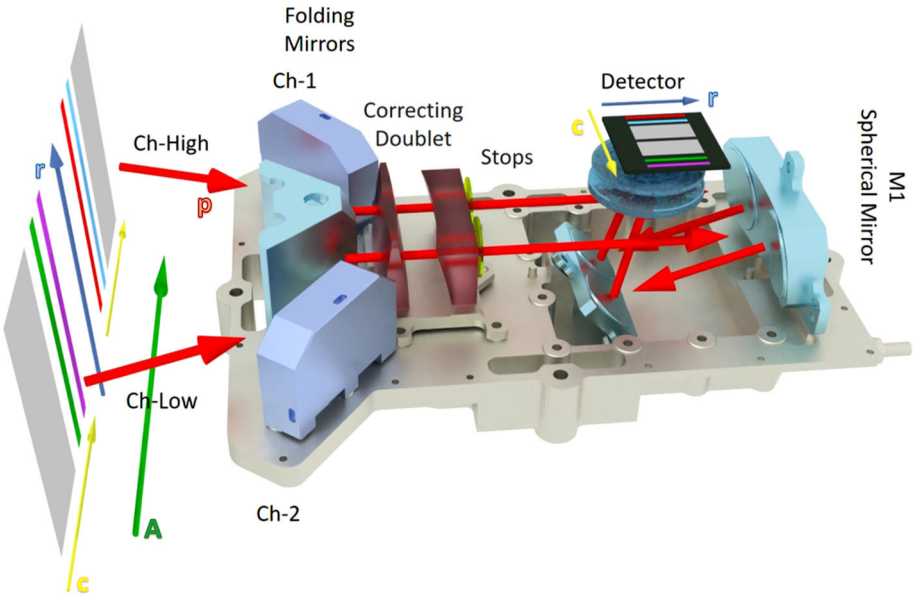

Fig. 4 STC schematic optical layout. From left to right: the on-ground FoV for all the filter frames is shown together with the projected directions of the detector rows (r) and columns (c). The green (A) and blue arrows (r) show, respectively, the along-track and cross-track directions. The optical path (p), through the camera to the detector, is depicted in red. On the detector, the directions of columns (c) and rows (r) are shown. The AT direction, A in green, changes at perihelion and aphelion, when the flip of the MPO will occur

same surface region with a different viewing angle at two very close moments, taking advantage of the along-track movement of the S/C.

3.2.1 Optical Design

The STC camera consists of two sub-channels, named High (H) and Low (L) with respect to the mounting interface on the S/C. Some of the optical elements are specific to each sub-channel, but most of them are common (Da Deppo et al. 2010). The STC optical design is basically composed of two principal units:

- a front unit, which consists of two independent fore-optics modules, one for each sub-channel;
- a common telescope unit.

Each of the fore-optics unit consists of a couple of plane-folding mirrors that are able to redirect the light beams coming from the planet (respectively at $-20°$ and $+20°$ for each sub-channel) to the second common unit (see Fig. 4).

The common unit is a modified Schmidt telescope with a focal length of 95 mm. A correcting doublet lens replaces the classical Schmidt plate. This design results in a compact and light instrument with a length reduced by about a factor of 2 with respect to the classical Schmidt design. The incoming light beams are focalized by the spherical mirrors on a 10 μm pixel size SiPIN hybrid CMOS detector. Before reaching the detector, the light rays are folded by a plane mirror and pass through a field-correcting doublet and the filter assembly. The system is an off-axis configuration (both in the AT and CT directions). The absence

Table 4 Main optical and digital parameters of STC

Parameters	Description
Optical concept	off-axis modified Schmidt, unobstructed
Strategy	Stereo-push frame
Maximum FoV (Cross Track)	5.38°
IFoV	105 μrad
Mean focal length	95.2 mm
Focal ratio	F/6.3
Optical distortion	<0.3%
Optical MTF	0.65-0.69
PSF (FWHM)	1.36/1.45 px
Pupil size	15 mm
Detector type	SiPIN CMOS
Full well	90300 electrons
Quantum efficiency 450/850 nm	91% / 83%
Pixel size	10 μm
A/D conversion	14 bits/pixel

of central obstruction and support structures (i.e., spiders) allows to obtain an optical Modulation Transfer Function (MTF) of about 0.65-0.69 and a Point Spread Function (PSF) of 1.36/1.45 px. The main instrument parameters are reported in Table 4.

3.2.2 Focal Plane Assembly

The STC detector allows snapshot image acquisition with a minimum integration time of 400 ns. According to the present radiometric model of Mercury (Slemer et al. 2018) the PAN filter acquisitions may arrive at 5.2 ms of integration time. Its capability of direct downloading of only specific pixels of the whole FPA allowed to select six specific windows, corresponding to the areas of each filter. The filter windows definition is shown in Fig. 5. This also permits to acquire a small area outside the illuminated part (bottom left part of the detector) called Window X. Window X will be used as a dark current monitor (Slemer et al. 2018); its position and dimension are defined to reduce the readout time and the dimensions of the buffer/data storage unit. Finally, the fast readout allows to avoid the presence of mechanical shutter, adopting the Integrate Then Read (ITR) strategy, and to achieve the short exposure times that are required for Mercury observations.

STC allows the acquisition of three quasi-continuous surface regions for each subchannel. These regions correspond to four broad-band and two panchromatic filters having specific wavelength bands in the range of 400-940 nm. Filter names, spectral bands, and dimensions and Field of View (FoV) in the AT and CT directions are reported in Table 5. The filters are listed in the order they appear on the detector from top to bottom (see Fig. 5).

Table 5 reports also the mean and maximum integration times predicted by the STC radiometric model (Slemer et al. 2018) and the angular direction of each boresight with respect to the nadir direction (Simioni et al. 2017a). The AT boresight direction of the panchromatic filters is about ±21° while those of the broad-band (BB) filters are about ±18° and ±19°.

Fig. 5 Focal Plane Assembly of STC. Vertical coordinates are expressed in pixels. Horizontal coordinates are expressed in pixels and in strips (1 strip = 64 pixels)

3.2.3 Observing Strategy

STC will work in the range of Mercury true anomalies between 138° and 222° (i.e., around aphelion, when the MPO will have the periherm above the sunlit hemisphere) and it will change the on-ground parameters according to the elliptical MPO orbit and its changing periherm argument. Table 6 reports an example of ground parameters, specifically for the first MPO orbit.

STC will adopt two operative modes: Stereo Mapping and Color Mapping (Fig. 6).

During the Stereo Mapping, that will be performed in the first six months of the nominal mission, the entire surface of the planet will be covered by both PAN filters. In this phase, STC will acquire images with a compression factor of 7 (bit rate of 2 bit/px). At the first periherm distance (480 km), the baseline of the stereo acquisition block will be 455.7 km providing a vertical accuracy of 80 m, assuming a conservative 1-pixel accuracy in the image matching.

For each MPO orbit (2.3 h), Mercury rotates by 0.595°, which corresponds to 25.3 km at the equator. It means that a FoV of 3.6° is required to obtain two successive camera

Table 5 STC filters and their main parameters

Name	Spectral band [nm]	Filter size on detector [px]	FoV (CTxAT)	Mean IT [ms]	Max IT [ms]
F920	Central wl: 923.8 nm FWHM: 20.5 nm $T_{peak} = 97.2\%$ $T_{outave} = 0.0081\%$	64 × 896	0.38° × 5.38°	6.5	40.0
F550	Central wl: 550 nm FWHM: 20.4 nm $T_{peak} = 97.9\%$ $T_{outave} = 0.005\%$	64 × 896	0.38° × 5.38°	6.8	40.3
PANL PANH	Central wl: 699.5 nm FWHM: 204.3 nm $T_{peak} = 99.5\%$ $T_{outave} = 0.011\%$	384 × 896	2.31° × 5.38°	0.8	5.2
F420	Central wl: 420.6 nm FWHM: 20.7 nm $T_{peak} = 98.7\%$ $T_{outave} = 0.005\%$	64 × 896	0.38° × 5.38°	9.4	43.0
F750	Central wl: 749.6 nm FWHM: 20.8 nm $T_{peak} = 99.9\%$ $T_{outave} = 0.0086\%$	64 × 896	0.38° × 5.38°	5.3	37.8

Table 6 Main on-ground parameters for the first-aphelion MPO orbit around Mercury. In this case, the periherm argument is at latitude 16° N, while the south-pole case is considered at latitude 83° S

	Periherm	Poles
S/C altitude [km]	480	966.7
Pixel on ground [m]	58	121.8
Swath CT [km]	48.3	100.96
Swath CT [°]	1.19	7.9
Swath AT [km]	23.3	52.5
Swath AT [°]	0.55	1.2

swaths with no gaps at the equator. Since STC has a FoV of 5.38°, there will be always overlap between adjacent orbits, that is important to improve the image matching in the mosaicking. The cross track FoV decreases as the latitude increases, in order to maintain the same percentage of overlap.

The Color Mapping will be performed in the second six months of the nominal mission and will provide target-oriented acquisitions of multiband images with the four broad-band filters. To limit the loss of data volume, STC will acquire images with a channel at a time, maintaining the overlap between two consecutive acquisitions between 10% and 15%. The images (corrected for phase angle) will provide mosaicked multiband cubes.

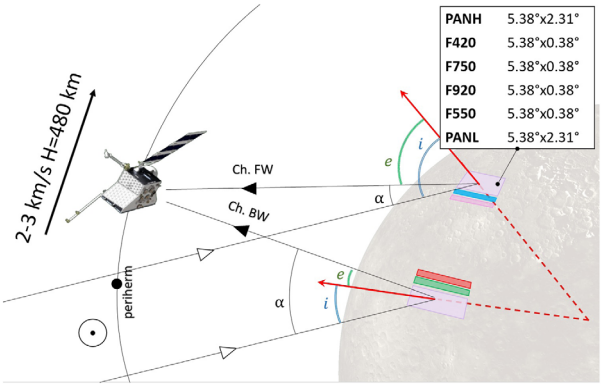

(a) .

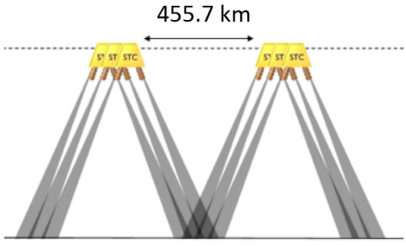

(b) .

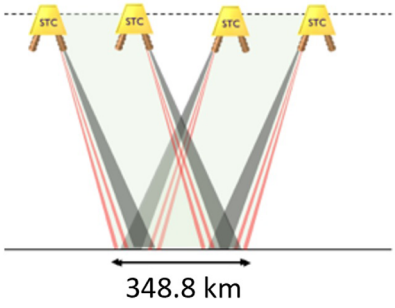

(c) .

Fig. 6 Main acquisition strategies of STC. In (a), the nominal on-ground FoV with the external PAN filters and internal BB filters. The phase, incidence, and emission angles are shown. In (b) and (c), the acquisition schemes for the global mapping (stereo mode) and color imaging (color mode) are respectively depicted

3.3 VIHI Description

The VIHI channel has been designed to perform hyperspectral imaging observations of the whole Hermean surface in the VIS-NearIR range (Flamini et al., 2010).

The channel concept is based on a collecting telescope and a diffraction-grating spectrometer ideally joined on the telescope focal plane, where the spectrometer entrance slit is located. The image of the slit is dispersed by the diffraction grating on a bi-dimensional detector. The instantaneous acquisition on the bi-dimensional detector consists of the slit image diffracted by the grating over the spectral range. The image itself is built in time by subsequent slit acquisitions, matching the S/C track speed with the slit size projected on ground (push broom mode). The final result is an hyperspectral cube, which associates a

Table 7 Summary of VIHI optics and detector's characteristics, including the Thermoelectric Cooler (TEC)

Optical parameters	Value
Aperture [mm]	25
Focal length [mm]	160
f/#	6.4
Etendue [m^2 sr]	3.1×10^{-11}
Field of View [°×°]	3.67×0.01
Pixel IFoV [µrad × µrad]	250×250
Pixel scale [m/px]	120 @ 480 km
Spectral range [nm]	400-2000
Spectral dispersion [nm/px]	6.25
Detector	
Pixel pitch [µm]	40
Quantum efficiency [%]	> 50
Full well capacity [e^-]	2×10^6
Operating temperature [K]	< 225
A/D conversion [bits/pixel]	14
Cooling power TEC [W]	4.5

VIS-NearIR spectrum to each pixel on ground. VIHI has been designed to achieve an IFoV of 250 µrad (corresponding to 120 m @ 480 km altitude) and to cover a spectral range of 400-2000 nm with a spectral sampling of 6.25 nm.

VIHI allows great flexibility of operations being capable of satisfying the global coverage resolution need (better than 500 m) throughout the orbit around Mercury using different operative modes (pixel binning). The instrument field of view of 3.67° cross-track is such that global coverage of the planet can be reached well within the first six months of the nominal mission. The second six months of the nominal mission shall be devoted to the detailed investigation of selected locations (about 10% of the surface) at VIHI's maximum spatial and spectral resolution. The major characteristics of the VIHI channel are listed in Table 7.

The channel itself is housed in a single box mounted on a common structure with the STC channel. VIHI consists of several subsystems: the optical system (Telescope plus Spectrometer), the FPA (containing the bi-dimensional detector and the thermoelectric cooler), and the proximity electronics, the shutter, the Internal Calibration Unit (ICU).

3.3.1 Optical System

The telescope is based on a modified Schmidt design which includes a dioptric doublet to correct aberrations. Its aperture and focal length have been chosen to obtain the desired spatial scale on the detector while being diffraction limited across the full spectral range (400-2000 nm). The telescope is followed by a slit and spectrometer, designed in Littrow configuration, adopting a flat grating. A quasi-linear spectral dispersion is obtained through a slit and a flat grating. All the optical power is due to the telescope (spatial scale), being only the spectral scale on the detector determined by the spectrometer. A layout of the optical design is represented in Fig. 7 (from Capaccioni et al. (2010)), where a single detector, covering both visible and infrared ranges, is folded out of the plane of the figure for reasons of space. The whole design has been driven by the necessity to reduce the volume (and

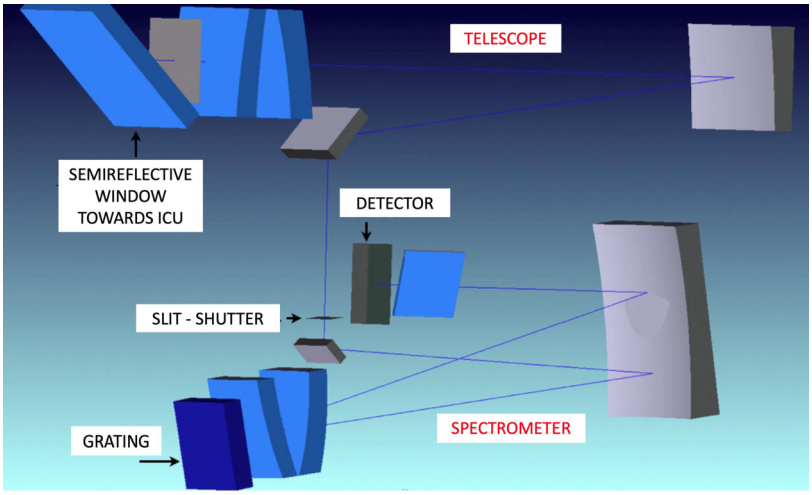

Fig. 7 VIHI Optical Layout (courtesy of Leonardo SpA)

consequently the mass) of the instrument as much as possible, with limited degradation of performance.

3.3.2 The Focal Plane Assembly

The heart of the instrument is its FPA which contains the order-sorting filters on the closure window, the detector itself along with a two-stage thermoelectric cooler (TEC, a Peltier cell) used to cool the detector to its operative temperature below 220 K. The VIHI detector has been provided together with those of STC and HRIC, from the same factory.

The complexity of the package lies in the need to guarantee a very high thermal conductivity to the S/C cold finger (temperature range 210-260 K) for maximum heat dissipation and, at the same time, to provide a very effective thermal resistance towards the instrument structure (temperature required in the range of 250-300 K) to minimize the parasitic heat to the TEC. The 256×256 pixels detector array is built through hybridization of cadmium-mercury-telluride (HgCdTe) sensors with the dedicated CMOS Read-Out Integrated Circuit (ROIC). The single pixel is 40×40 µm and the input circuit is a Capacitance Transimpedance Amplifier (CTIA) working in snapshot integration mode and allowing to readout while integrating. This feature is essential to guarantee the high acquisition speed required by the observation plan of the BepiColombo mission.

The spectral range of 400-2000 nm has been selected after a trade-off between the scientific needs and the technical constraints. Scientific objectives required a minimum wavelength of about 400 nm, while standard Hybrid CMOS HgCdTe array detectors have a cut-off at 800 nm; the opacity below 800 nm is due to the optical properties of the CdZnTe substrate (over which the sensitive HgCdTe crystal is grown) which becomes opaque to radiation below that wavelength. A technique to remove the CdZnTe substrate and substitute it with a transparent material has been developed by several companies. This approach allows to extend the spectral range down to the required 400 nm and to use a single detector to cover both visible and infrared ranges, reducing considerably the instrument volume and mass.

The long-wavelength operative limit of 2000 nm was mainly dictated by a balance between:

– the scientific need to cover as much as possible of the second Fe-transition in pyroxenes which causes an absorption band with a minimum located within 1900-2200 nm (depending on the Fe and Ca content of the pyroxenes);
– the need to minimize the dark current contribution to the detector noise in order to achieve a radiometric performance (SNR) of at least 100 throughout the spectral range, to be able to identify minerals present in the soils, and to determine their abundances.

As the dark current strongly depends on the operative temperature, as it follows the exponential diode-law, for a given cut-off wavelength, the analyses of the detector performances have shown that, at the operative temperature of 220K, an extension of the IR range from 2000 to 2200 nm would have caused an increase of at least a factor of 50 in the dark current level throughout the spectrum. For this reason, we dropped the option to extend the spectral range to 2200 nm.

The proximity electronics contains all the functional capabilities to interface the ME through a Space Wire protocol, to drive the FPAs, the shutter, the calibration unit, and the thermoelectric cooler, and to perform the acquisition and conversion of the science and house-keeping data.

3.3.3 Shutter

The instrument uses a single mechanical moving part, which is a shutter, located at the spectrometer slit. The shutter, a fail-open device, consists of a rotary solenoid holding a small metallic blade which covers the instrument slit. The shutter is essential to determine and remove the dark signal introduced by the detector and the background signal due to the spectrometer housing. Periodically along the orbit, during acquisition of science data, the shutter shall be closed and a dark/background acquisition shall be performed.

3.3.4 Internal Calibration Unit

The Internal Calibration Unit (ICU) is needed to periodically verify degradations, if any, of the performancs of the overall channel with respect to the absolute calibration performed on ground and the spectral registration. This implies a set of measurements with known sources to monitor the spectral and radiometric response and the flat field (including defective pixels). The basic requirements for the ICU are a full and uniform illumination of VIHI's pupil and a radiometric flux of the same order of magnitude of the flux entering the pupil from Mercury. The adopted solution goes away with moving parts using a semi-reflective window located at the entrance pupil of the instrument (labelled as semi-reflective window in Fig. 7 and semi-reflective window in Fig. 8). The ICU design consists of two calibration sources and an optical system that is able to illuminate, with a uniform beam, the instrument's pupil. In order to guarantee a high signal across the entire spectral range (0.4-2.0 μm), two different sources are used: 1) a white bright LED for the VIS range (0.4-0.8 μm) and 2) an incandescent lamp for the 0.7-2.2 μm range. These sources are placed at 90° with respect to each other and illuminate a diffuser through a beam splitter (Fig. 8). The white LED source (model NJSW036 by NICHIA) is based on a chip-type design. The LED structure is made of ceramics for the package and silicone resin for the encapsulating element and lens. The internal electrodes are of gold. The incandescent lamp (model 01163 by HPX-Welch Allyn) uses a filament in krypton gas with a quartz bulb. Both sources are powered with stabilized currents by the PE; the sources electrical parameters are measured during the switch-on and transmitted to ground together with the instrument's telemetry. The incandescent lamp is

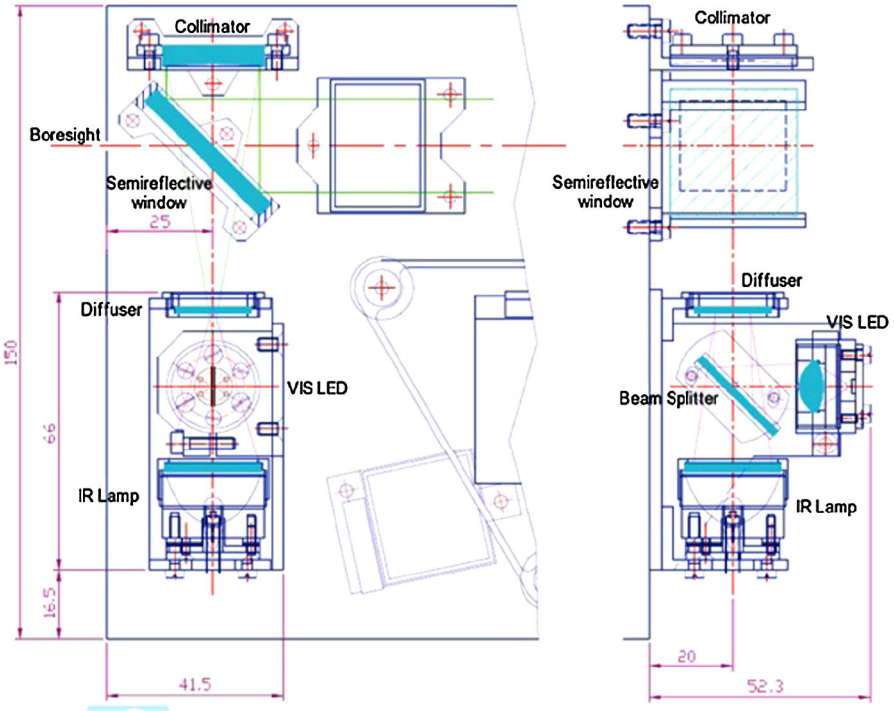

Fig. 8 VIHI Internal Calibration Unit layout describing the major components (all units in mm)

equipped with an elliptical concentrator to increase the energy of the emitted beam. In addition, a Didymium filter is deposited on the closure of the elliptical concentrator to add specific spectral absorption bands used to monitor the spectral registration. The LED uses a silicon lens, in which it is embedded, to improve its efficiency. A diffuser operating in transmission is placed along the ICU optical path, allowing the homogenization of the beam and removing any possible gradients due to image residuals of the lamp's filament and LED lens. After passing through the diffuser and through the semi-reflective window placed on the telescope's pupil, the beam coming from the internal sources is reflected by the collimator's mirror to match the entrance's pupil. The semi-reflective window has an efficiency of about 90% in transmission along the boresight (this is the nadir pointing direction toward Mercury); the efficiency along the ICU light path is then about 10%. Taking into account also the spectral reflection of the collimator, the sources radiation intensity entering the boresight is of the order of 8% of the emitted radiation. This is the penalty to be paid for avoiding moving parts in the light path still allowing all the optical elements to be verified by the in-flight calibration. The internal calibration shall be performed when the BepiColombo spacecraft observes the nightside of the planet, and no light is entering the boresight.

4 Main Electronics and Onboard Software

4.1 Main Electronics Overview

The ME is a self-standing module composed of three boards: a nominal Data Processing Unit (DPU), a redundant DPU, and a Power Unit (PU). These three boards are placed on

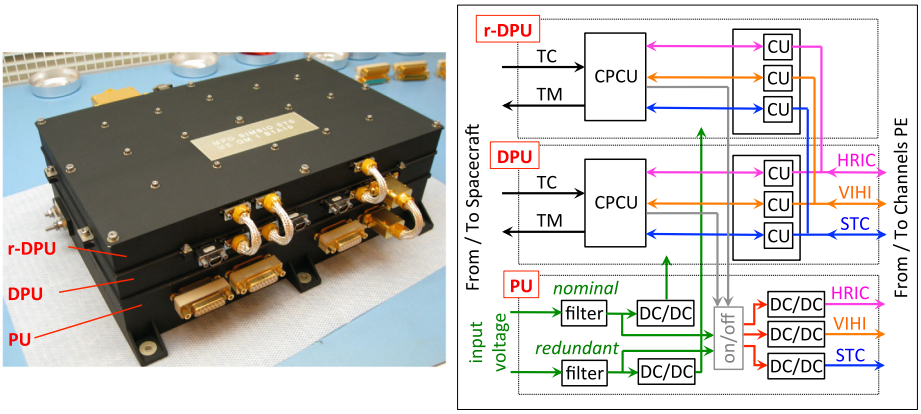

Fig. 9 Main Electronics. The ME qualification model (left) showing the three electronics boards within their housing (from top to bottom, redundant DPU "r-DPU", DPU, and PU) and a simplified ME functional Block Diagram (right). See text for acronyms

top of each other and enclosed in an aluminium alloy structure ensuring housing, heat dissipation, and ElectroMagnetic Compatibility (EMC). The structure is composed of three separated belts surrounding the three electronic boards for protective housing and heat dissipation, one internal metallic plate separating the power unit from the two other boards, thereby ensuring electromagnetic insulation of the power unit board, and, finally, top and bottom covers for closing the ME case. An overview of the ME is presented in Fig. 9.

4.2 Data Processing Unit

The DPU ensures the experiment control/command tasks, the data handling, and the onboard data processing. It is divided into two elements (Fig. 9), the Command and Process Control Unit (CPCU) and the Compression Unit (CU).

The CPCU provides a high-level monitoring and handling of the three channels. It manages the interface to the spacecraft: reception, decoding, and execution of TeleCommands (TC), powering on and off of the three channels, synchronization with the onboard time, encoding, formatting, and transmission of telemetry (TM: science and housekeeping data) packets to the spacecraft. The CPCU is based on an AT7913E LEON-II core 32-bit processor.

The CU is composed of three sub-Compression Units (sub-CUs), each being dedicated to a single channel (VIHI, STC, or HRIC). Each sub-CU handles the data flow from its channel front-end electronics so as to generate TM data packets. Each sub-CU includes a LEON processor, a Field Programmable Gate Array (FPGA) unit which implements the wavelet transformation and a memory buffer.

The redundant DPU is similar to the nominal one, except that only one space wire link is implemented between the ME and the three proximity electronics (see Fig. 9).

4.3 Power Unit

The PU provides the required power supplies to the nominal and redundant DPU of the ME, and to the three proximity electronics units of VIHI, HRIC, and STC, respectively. It

is equipped with power-line input filters and DC/DC converters to provide the needed secondary voltages. Four independent DC/DC converters power the three proximity electronics and the nominal DPU. Similarly, a distinct redundant line within the PU independently powers the redundant DPU, with an independent EMC input filter and DC/DC converters.

4.4 Onboard Software

The ME onboard software (OBSW) is resident in the CPCU of the ME DPU. The main OBSW functions are: booting and initializing the ME software and hardware, establishing TC/TM link with the spacecraft, monitoring the three channels configuration, calibration, and science mode observation, and monitoring and handling instrument house-keeping and science data. The OBSW allow to control in parallel the activation and operation of the three channels of the instrument suite. It is composed of two programs, the Boot SoftWare (BSW) and the Application SoftWare (ASW).

The BSW is activated once the ME is *power on*. It is dedicated to the execution of self-check procedures relevant for the internal ME subsystems correct functioning, notably the DPU main memory and the spacecraft interface modules and local time synchronization. The BSW is located in the programmable read-only memory (PROM) of the DPU board and can therefore not be updated.

The ASW is the program that manages the operation and data acquisition of the instrument channels. It controls the acquisition, reception, formatting, and storage of the scientific data and of the relevant house-keeping data, and carries out the data delivery towards the spacecraft. The ASW is located in the erasable memory (EEPROM) and can thus be updated during flight. Two ASW images are stored in the erasable memory, which makes it possible to reduce risk in the case of updates, given that the new uploaded version replaces only one of the two images: if its fails, the previous version is still present onboard.

4.5 Compression Strategy

The CU performs data compression. Each frame transmitted by a given channel is first binned if requested by the TC parameters, and then stored by the FPGA of the corresponding CU. Once data acquisition is complete, the CU compresses and formats the data in series of TM packets with three possible processing approaches:

- bit-packing (no compression);
- lossless compression;
- lossy compression.

The HRIC and STC pixels are coded on 14 bits, while the VIHI pixels are coded on 16 bits due to dark subtraction. Bit-packing means that the pixel contents are not sent one by one but are packed in a continuous flow of bytes. Indeed, for HRIC and STC, 14 bits do not constitute two bytes (2 times 8 bits), thus, the transfer is not optimized if two bytes are used for 14 bits. For VIHI (16 bits/pixels), there is no effect from bit-packing. Both bit-packing and lossless compressions are implemented by the LEON processor of the sub-CU. When implementing the lossy compression algorithm, the FPGA of the sub-CU performs a wavelet transform on data sets with a size of 64×64, 64×128, or 128×128 data elements. The two dimensions are spatial for HRIC and STC, spatial and spectral for VIHI. For spatial-spectral data, a preprocessing stage takes advantage of the strong correlations between light variations in neighbor spectral bands for improving data quality. A speed-optimized entropy code by (Langevin and Forni 2000) derived from a tree-coding algorithm (Said et al. 1996)

is implemented by the LEON processor of the CU. The software of each sub-CU is uploaded from a PROM, hence it cannot be updated.

The choice of compression rates results from compromises between data volume availability and science requirements. Bit-packing will mainly be used for validation purposes. With lossless compression, the generated data volume depends on the entropy of the scene; typical volumes estimated on practical cases are 10 bits/pixel for HRIC/STC, reduced to 7 bits/pixel for VIHI thanks to dark subtraction. Even the bias removal for VIHI is done by dark subtraction.

The lossy compression scheme implemented on SIMBIO-SYS is rate controlled from 0.125 to $\sim$ 4 bits/pixel, with a TC defining the output in bits/pixels for each observation. For science observations, typical data allocations will be $\sim$ 2 bits/pixels (compression factor of 7) for images (STC and HRIC) and $\sim$ 3 bits/pixels for spectral images (VIHI). The impact of the choice of the compression factor on the derivation of science parameters has been evaluated prior to mission launch, e.g., for STC stereo retrievals (Re et al. 2017).

5 System Calibration

In order to properly extract and derive the relevant scientific information, in-depth characterization, calibration, and verification of instrumental performances are mandatory, from sub-system to integrated system levels during assembly, commissioning, cruise, and observation phases. The characterization and performance validation of SIMBIO-SYS have been performed through a sequential approach that followed the main instrumental development phases. These measurements have been performed at several stages:

- sub-system level for sensitive units to be integrated;
- on-ground calibration at channel levels (HRIC, STC and VIHI);
- on-ground calibration on the fully integrated instrument, performed prior to its delivery for integration on the S/C;
- S/C calibrations: measurements and tests performed on the instrument when integrated on the S/C, prior to its launch;
- in-flight calibrations during science operations (only functional tests can be performed during the cruise due to the Mercury Transfer Module on top the nadir wall of MPO).

The on-ground calibration at the SIMBIO-SYS level (previously listed step 3) has been performed at IAS (Institut Astrophysique Spatiale, Orsay, France) using specific facilities developed and mounted for this activity (Poulet et al. 2015). The measurements have been focused on the radiometric performance (radiometric cross-calibration and absolute radiometric calibration of the four apertures) and straylight investigations. Additional performance and functional tests were also performed by having the instrument under flight configuration from a thermal and electrical point of view.

The setup consisted of a thermal vacuum chamber simulating the space environment, an optical bench collecting calibration sources and optical elements that simulated the conditions of Mercury observations, mechanical interfaces (including an hexapod) used for positioning the three channels inside the vacuum chamber, thermal interfaces to explore the operating temperatures, and computer interfaces that synchronized the calibrations sequences with the status of the calibration device.

The measurements completed are listed in Table 8. Due to time constraints, the strategy was to automate, as much as possible, the calibration measurements. All the sequences were thus prepared, validated and simulated before the campaign. Nevertheless, a preparation

Table 8 List of measurements performed during the calibration campaign. Thermal configurations for major tasks are indicated

Tasks	Status
Radiometric cross-calibration	Completed under nominal thermal conditions (HRIC & STC @ 268K, VIHI @ 220K)
Absolute radiometric calibration	Completed HRIC @ 268K and TEC Off STC @ 268K, 273K and TEC Off VIHI @ 210, 220, 225K
Straylight monitoring	Completed for the four apertures at nominal temperatures
Spectral check on mineral samples	Completed for 6 samples with VIHI and 2 with HRIC (all filters); samples not focussed
Additional checks	STC Vignetting (nominal temperature) Operative modes Data compressor (HRIC, VIHI) EGSE functionalities Binning test for HRIC and VIHI STC detector offset investigations STC and HRIC straylight tests on air

phase of a few days was still necessary to tune instrumental parameters (such as integration time and number of frame acquisition) as well as device parameters (for instance, the position of the hexapods corresponding to different points on the STC and HRIC detectors and VIHI slit). Radiometric measurements have been performed at 3 thermal configurations (nominal, hot, and cold), while the other sequences have been acquired at nominal temperatures. A quick-look data analysis has been performed. We evaluated the following parameters for both STC and HRIC: map of spurious pixels, background evaluation, size of the illuminated spot, integrated flux for each filter of the cameras, and a first estimate of the transfer functions. However, as the data reduction of the radiometric measurements and the resulting derivation of an accurate Instrument Transfer Function (ITF) are the result of the full pipeline (including flat-field and linearity corrections) that is still under construction, we here only exemplify a few measurements. Figure 10 shows a typical image acquired by the visible channels of SIMBIO-SYS with the integrating sphere as the light source. Illumination of all filters with at least 2 positions per filter were obtained, which allowed to compare the profiles at different positions on the focal plane area. Small subtle differences are observed and are most likely due to the variation of the responsivity of the instrument across its field of view (Fig. 10C).

The straylight measurements are the subject of accurate analyses that will be included in the outcome of the data processing.

During the nominal mission, there will be the inflight calibrations that will be performed two times per Mercury year.

6 HRIC Calibration

HRIC calibration activities at channel level were performed at Leonardo SpA (Campi Bisenzio, Firenze; formerly Selex ES) premises in spring-summer 2014. These activities were per-

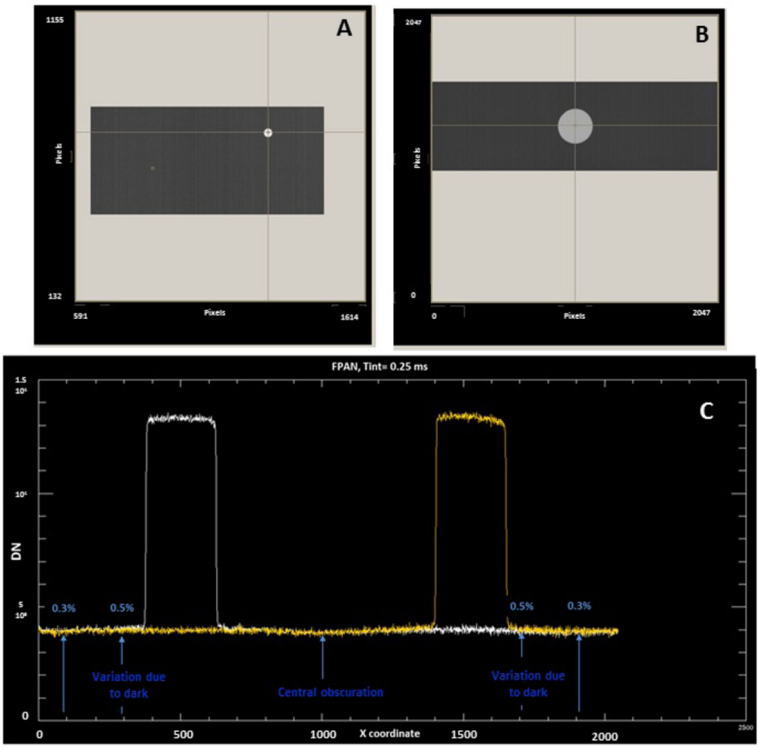

Fig. 10 Examples of frames acquired with the panchromatic filters (hereafter FPAN) of STC (A) and HRIC (B) channels using the integrating sphere as a light source. The diameter of the spot is, respectively, 27.5 STC pixels and 250 HRIC pixels. These values are close to the theoretical values (29 STC pixels and 260 HRIC pixels). (C) Profiles of two FPAN measurements using the integrating sphere. Small background variations are due to the instrumental noise (corresponding to standard deviation of about 0.3%). Additional noise in the background (about 0.5%) is observed near the source spot. The central obscuration and the decrease of the signal in one of the profiles (decreasing plateau) are attributed to the uncorrected instrument responsivity

formed at channel level (optical head + detector + proximity electronics), allowing full channel control and signal digitization. The analyses of the collected data allowed to check for the channel performances (i.e., image quality, radiometric and geometrical performance) and to define the calibration pipeline for image processing. During the development of HRIC and the SIMBIO-SYS instrument, other characterization activities have been performed, e.g., at the detector level (for flight detector selection and characterization) and at the SIMBIO-SYS level (Poulet et al. 2015), with all channels integrated and connected to the ME. In the following sections, only the results of the calibration at unit level will be presented. The results obtained include the measurements of both HRIC electrical parameters and radiometric performance. All the parameters have been measured at pixel level due to the relatively high variability of CMOS detector with respect to CCD. The final target was to obtain the calibration pipeline parameters correcting pixel-by-pixel the HRIC data.

An HRIC model (Zusi et al. 2008; Zusi 2009), linking the digital output to the specific physical quantity, was set up for the data conversion from Digital Number (DN) to physical quantities, which will be regularly checked in flight. This mathematical model describes HRIC behavior with respect to the following input parameters:

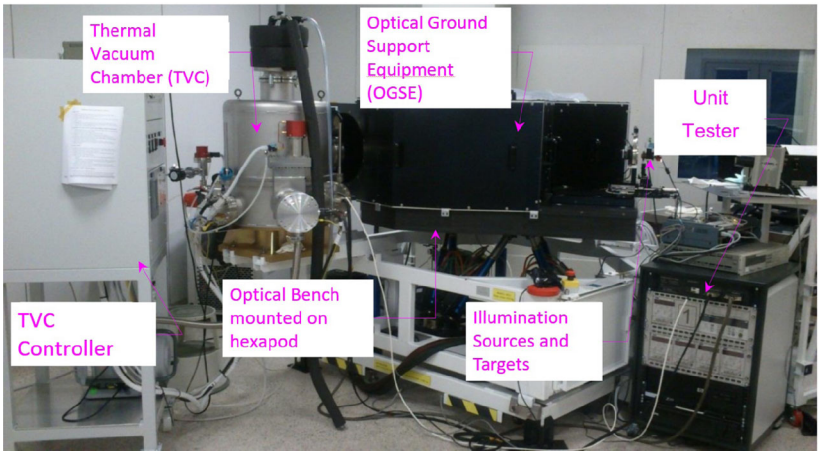

Fig. 11 Experimental setup used during the on-ground HRIC channel calibration campaign. The experimental setup was composed of the TVC, where HRIC was housed, the TVC controller used to maintain HRIC in the range of the operative temperatures, the OGSE with externals sources, targets, and collimating optics, and the UT to control both the HRIC proximity electronics and the OGSE

– P, i.e., the input flux coming from the planet surface under specific observation geometries (perihelion angle, latitude etc.);
– FE, i.e., the conversion factor (number of electrons over energy) to transform P in the number of electrons;
– n(e^-), i.e., the noise affecting the acquired signal of each sensor pixel.

The CMOS image sensor, as usual for integrated circuits, during the conversion process of light power into an electrical signal, is affected by temporal and spatial noise. The noise power can be estimated mathematically: by computing the fluctuation signal variance and the mean signal it is possible to determine the mean number of electrons (Tian 2000). The temporal noise, due to several different effects (e.g., Johnson noise, 1/f noise of the MOS transistors, kTC noise etc), corresponds to the variation in pixel response for a constant illumination over a period of time. The temporal noise can be evaluated by computing the standard deviation of every pixel response on many frames, acquired for a specific time and illumination. The spatial noise can be evaluated by computing the coefficient of variation across a frame, and, contrary to temporal noise, it can be corrected. The classification of noise outlined previously is based on the concept that noise in a digital image is composed of the photon shot (random) and pattern (deterministic) components. The process of averaging multiple images reduces, during the calibration procedures, the random shot/photon components and enhances the pattern noise, which remains constant across all images.

6.1 Calibration Setup

The entire HRIC Proto Flight Model (PFM) calibration campaign has been performed in a class 100,000 cleanroom where the HRIC Optical Ground Support Equipment (OGSE) and the Thermal Vacuum Chamber (TVC) have been operated. The performance test set-up employed is shown in Fig. 11. It mainly consists of:

– the TVC, where the PFM is mounted;
– the TVC control system;

– the Unit Tester (UT) to control HRIC during the test operative phases;
– the OGSE to provide calibrated optical input to the instrument inside the TVC.

The OGSE used for HRIC (Barilli et al. 2012), has the TVC mounted, insulated by ground, on the same mechanical support on which the Optical Bench (OB) with the collimator is mounted. The optical design of the collimator is all reflective, all spherical unobscured 4-mirrors Brunn configuration (with 3000 mm as focal length, and the pupil diameter of 250 mm). The collimator has been suitably developed by Leonardo SpA for the testing of HRIC. On its focal plane, it is possible to mount several source modules for radiometric, geometrical, and spectral test configuration. The OB can be moved with 6 degrees of freedom (DOF) by a large hexapod with 2-arcsec rotation pointing accuracy. A higher angular resolution is obtained by moving a pinhole within a range around the collimator focus in which the optical quality is maintained by means of two orthogonal piezo-translation-stage actuators.

6.2 Performed Measurements

During the on-ground calibration campaign, we performed both measurements with and without illumination sources. Measurements without illumination sources were devoted to the channel electrical characterization, while the measurements performed using external illumination sources (Barilli et al. (2012)) were mainly devoted to the radiometric calibration and spatial noise characterization. All the measurements have been performed at different detector temperatures in order to check the thermal behavior of the HRIC parameters.

The parameters characterized are the following:

– the Dark Current (DC) behavior;
– the detector Read-Out Noise (RON), i.e., the temporal noise, without illumination;
– the Fixed Pattern Noise (FPN), i.e., the spatial noise;
– the Photo Response (PR) and the Photo Response Non-Uniformity (PRNU), vs. radiation flux, integration time and wavelength;
– the overall radiometric performances.

6.3 Results

6.3.1 Dark Current

The DC is the low leakage current that flows in a photosensitive device when no photons are incident. In a CMOS image sensor, it is due to random generation of electrons and holes in a Pinned Photo Diode (PPD). As shown in Fig. 11, we found a double trend for the DC. For very short exposure times (IT $<$ 0.05 ms) the DC shows a high rate that can be fitted as a quadratic function of the exposure time (see Fig. 12). For IT $>$ 0.05 ms, the DC shows a smooth and relatively low linear rate, well within the requirements. The DC was also measured at temperatures higher than the operative value, showing the expected behavior (Fig. 12, right panel).

6.3.2 Read-Out Noise and Fixed-Pattern Noise

The RON is the inherent noise of an image sensor due to temporal variation in the pixel value over period of time, and it is associated with the signal-processing electronics. The RON is measured for a very short IT to avoid Dark Spatial Non-Uniformity (DSNU) and is

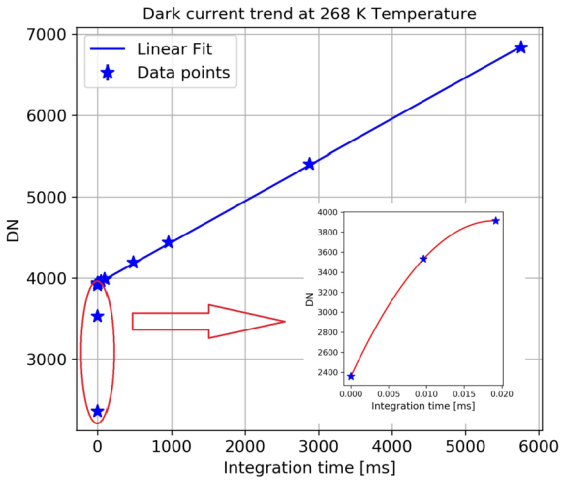

Fig. 12 DC behavior. The top panel shows the double rate of the DC, for very short IT < 0.05 ms, we obtain a parabolic trend, while a linear trend is measured for IT > 0.05 ms. The bottom panel reports the dependence of the DC as a function of the temperature

measured in darkness to keep photon shot noise at minimum. Due to the DC behavior, we evaluated the FPN and the RON at two different values of exposure time: for IT < 0.05 ms and for IT > 0.05 ms (Fig. 13 and Fig. 14). Considering the images taken at very short exposure time, we obtain the evaluation of the RON as the standard deviation of the DN registered for each pixel, and the FPN as the values of the mean of the DNs for each pixel. We also evaluated, for these two parameters, their temperature dependence, repeating the computations on images acquired at three different temperatures.

6.3.3 Photo Response and Photo Response Non-Uniformity

For an image sensor, the photon response is the measurement of the sensor's capability to convert optical incident power (i.e., the number of impinging photons for a given exposure time) into an electrical signal (i.e., the gain of the system multiplied by the number of electrons generated). The PR curve provides useful information on many characteristic parameters of the CMOS sensor, e.g., charge-to-voltage factor, if the Quantum Efficiency

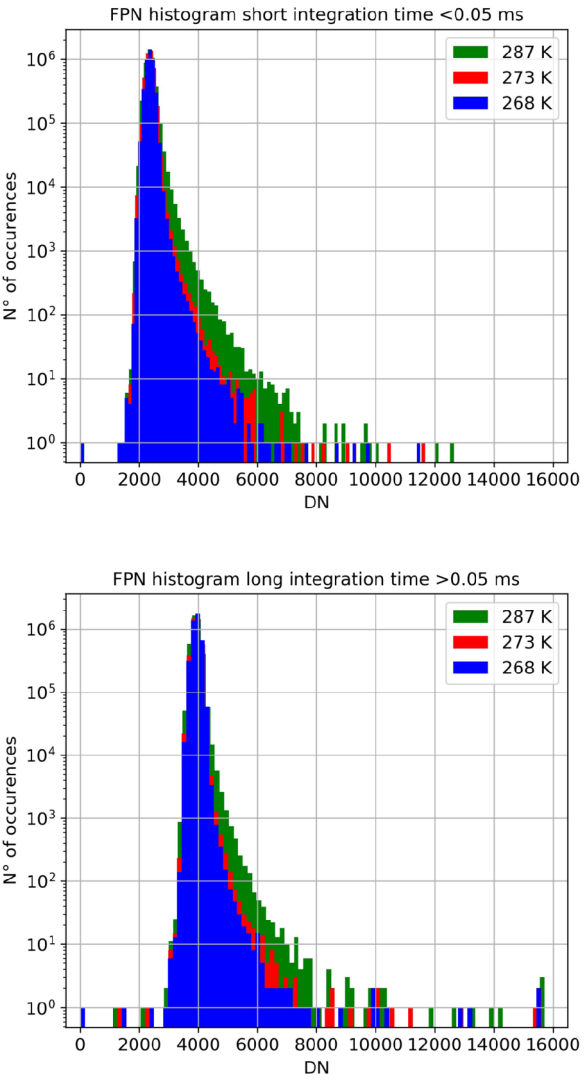

Fig. 13 FPN histograms. The distributions of the spatial non-uniformity of the pixel level for IT < 0.05 ms (top) and IT > 0.05 ms (bottom)

(QE) value is available, non-linearity, saturation voltage, and full-well capacity. The PR, depending on the wavelength, is generally characterized for a specific spectral range (mostly, around peak response wavelength). We characterized the PR of the panchromatic and the 3 broad-band filters. The PRNU is the result of variations in photo-responsivity of one pixel and it is proportional to the illumination. We can evaluate the radiometric characterization and calibration for one reference pixel and estimate the difference with the remaining pixels. A fitted curve of the obtained data can be calculated and used for correction (e.g., polynomial fit up to 3rd degree and splines).

6.3.4 Radiometric Performances

Absolute radiometric calibration, for a linear sensor, is performed by ratioing the DNs output from a sensor, with the value of an accurately known, uniform radiance field at its entrance

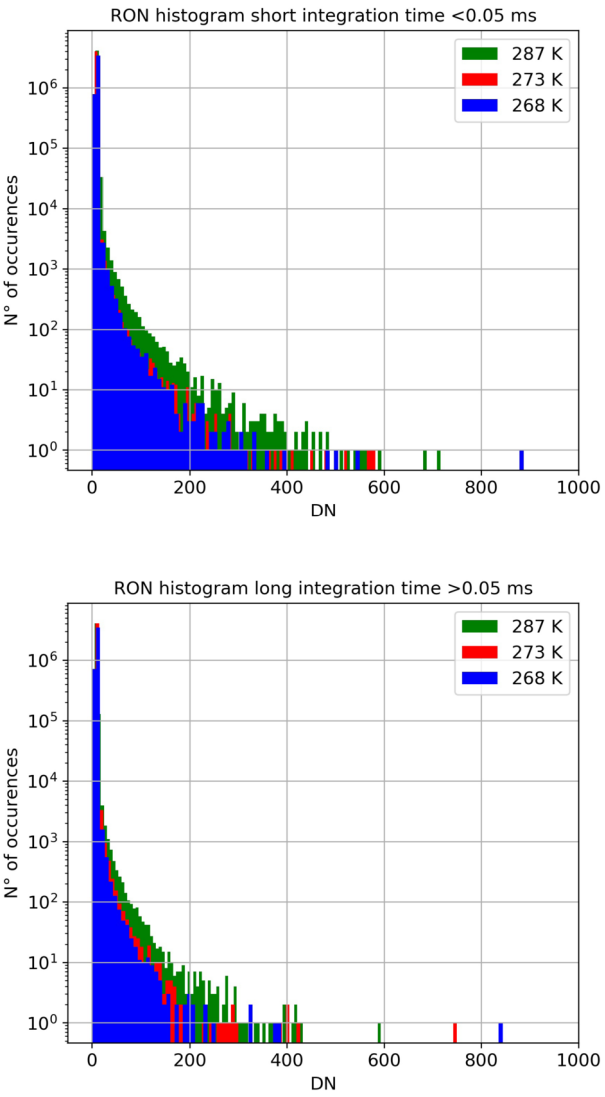

Fig. 14 Histograms of the RON distribution for the whole detector for IT < 0.05 ms (top) and IT > 0.05 ms (bottom). The distributions are reported for the 3 different temperatures

pupil. At best, in the solar spectral range, uncertainties are 3-5%, generally being highest at the extremes of the range. Ideally, a CMOS image sensor should have a linear behavior, i.e., it should respond linearly to the incident light (photons). Actually, due to nonlinear devices in the pixel and in the signal-processing units, the sensor deviates from a perfectly linear response. The response of each pixel was characterized as a function of the exposure time and the light flux intensity. HRIC has a response with respect to the flux very close to linearity, when considering about 80% of the available signal range. Moreover, the response characterization of each single pixel allows us to remove the PRNU from the images. The absolute radiometric calibration of the PRNU reference pixel has been derived by retrieving a fitting curve from the experimental data. To extend the dynamic range instead of a linear fit, a more complex function might be used, such as a cubic fit, as shown in Fig. 15. This approach becomes necessary for the radiometric characterization of the BB filters of HRIC,

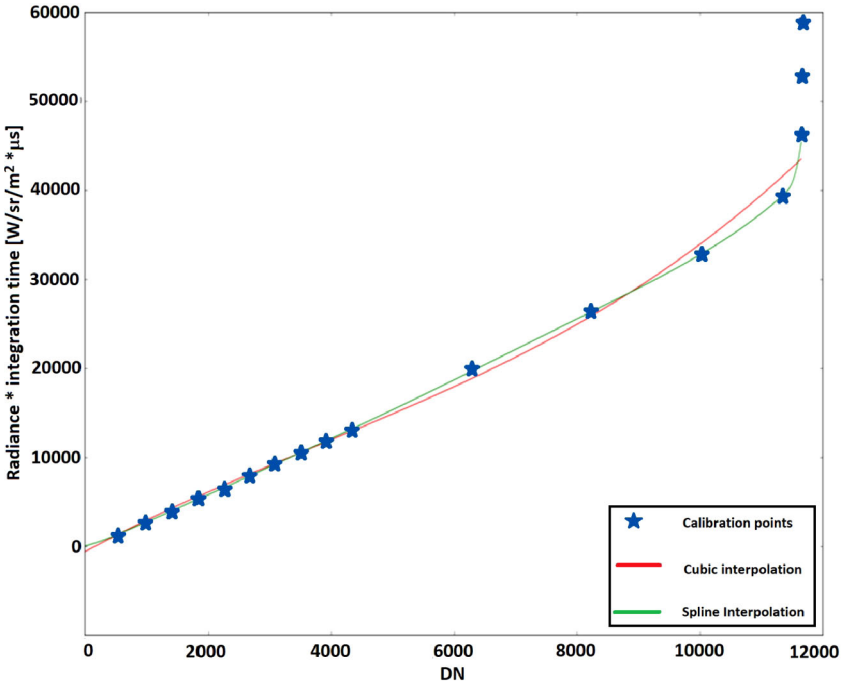

Fig. 15 Radiometric calibration curve for the panchromatic filter. The plot shows the measurements obtained with a calibrated source at different integration times. However, a linear region of the detector can be identified. We tried to work on the data with more complex fitting law to extend the dynamical range. We obtained good results using spline fitting. The same approach has been used for the 4 broad-band filters

as the analysis of the calibration measurements showed that the radiometric response was not well reproduced by a simple linear model. It has been necessary to apply a spline fitting to derive a satisfactory radiometric response curve.

The non-linear fit allows extending the dynamical range of the detector. In the case of the PAN filter, the cubic fit has been used extending the dynamic range of about 10%, taking into account also the relatively high level for the FPN, allowing to optimize the instrument observations. For the BB filters, the best results have been achieved by using the spline.

The radiometric performances will be checked during the mission with dedicated calibration acquisitions. These measurements will allow a characterization of the aging effects including radiation environment.

6.4 Summary

The calibration measurements performed on HRIC allowed to derive all the necessary electrical parameters, to evaluate the noise, and to characterize the radiometric performance (Table 9).

The values of the parameters obtained are compliant with the requirements imposed during the design phase and will allow fulfilling the scientific requirements. The next step will be the development of a workflow for the calibration of raw images. The workflow will be used to test the reliability of the correction approach identified and to verify the optical performance parameters of HRIC.

Table 9 Main calibrated parameters of HRIC. The Fixed-Pattern Noise is the average value for the whole detector and we report two values because of the detector behavior described in Sect. 6.3.2. The Read-Out Noise is the spatial average value on the detector and the dark current is the average value on the detector for the linear part described in Sect. 6.3.2

Parameter	Operative temperature 268 K
Full Well	$\simeq$ 11600 [DN]
Fixed-Pattern Noise	3932 ± 133 [DN] (int time $>$ 0.05 ms)
	2358 ± 135 [DN] (int time $<$ 0.05 ms)
Read-Out Noise	9 ± 1 [DN]
Dark current	0.5 [DN/ms] $\pm$ 0.05

7 STC Calibration

The STC pre-launch calibration has been performed to fully characterize the channel performance. As STC is a stereo camera composed of two identical sub-channels with some of the optical components and the detector in common, the calibration activities included measurements at sub-channel level and stereo calibration at channel level.

The full calibration campaign for the STC PFM took place in Leonardo SpA the SIMBIO-SYS prime industrial contractor. For the sub-channel calibration, a custom OGSE, designed by Leonardo SpA, has been used to determine the geometric, radiometric, and spectral performance. The stereo validation has been performed using the setup realized by the STC scientific team, and, through indoors acquisitions, the 3D reconstruction performance of STC has been evaluated (see Sect. 7.6). In the following sections, the results obtained for the standard calibration and the stereo validation will be presented and discussed. The stereo setup has been assembled and tested in the Padova laboratory before using it in Leonardo. A summary of the measurements completed in each calibration phase is reported in Table 10.

7.1 OGSE Calibration Set-Up

The core of the OGSE (Simioni et al. 2016) used for the calibration is a collimator lens with a focal length of 750 mm, chromatically corrected in the visible spectral range, coupled to a rotating plane-folding mirror, which can rotate in two directions to cover the FoV of each sub-channel, and a TVC mounted on a rotational stage to align the OGSE with one or the other sub-channel. Different sources have been placed in the collimator focus depending on the required measurements:

- a pinhole, as target source, for geometrical calibration;
- an integrating sphere, for the radiometric calibration (Da Deppo et al. 2014);
- a diffuser (spectralon) illuminated via a monochromator to derive the spectral response of the target.

7.2 Geometric Calibration Results

STC will perform complete global mapping of the Mercury surface in 3D, thus a fine geometrical calibration was performed on both sub-channels and for different temperatures.

Table 10 Sequence of calibration activities performed during the development and calibration phases for STC

Phase	Unit	Measurements	References
1a	Detector	System requirements validation	
1b	Detector	Full well capacity	
		Dark current	
		Noise	
		Conversion factor (T = 268 K)	
		Wavelength response (T = 268 K)	
2	Stereo calibration setup	Stereo Validation	Simioni et al. (2014)
3	FM	Boresight and reference mirror	Da Deppo et al. (2015)
		Geometric calibration	Simioni et al. (2019a)
		Radiometric calibration	Slemer et al. (2019a)
		Linearity, flat field	Slemer et al. (2019c)
		Spectral calibration	Slemer et al. (2019b)
		Stereo validation	Simioni et al. (2014), Re et al. (2015, 2017)
4	System level	Radiometric cross-calibration	Da Deppo et al. (2011)
		Radiometric absolute calibration	
		Straylight	
5	Dark check at room T		Simioni et al. (2017b)

Using the OGSE setup, a grid of point source images has been acquired for each filter to measure the distortion and its variation as a function of the temperature.

The measured distortion is quite low due to the Schmidt concept and the position of the aperture stop adopted in the optical design (Da Deppo et al. 2015; Simioni et al. 2017b). The distortion is higher in the left and right regions of the focal plane (see Fig. 16) in the limits of the cross-track field of view (corresponding to $\pm 2.69°$). In this case, the distortion reaches a maximum measured value of 0.3%, expressed as the percentage difference between the expected, with no distortion, and the real position of the image point, which means a maximum deviation of 1.5 pixels (Simioni et al. 2016). The STC layout is off-axis, as the input beam is not injected along the optical axis of the telescope, both in the AT and CT directions. This peculiar configuration does not allow the adoption of a classical distortion model (Da Deppo et al. 2015), hence a distortion map model based on Rational Function Model (RFM) (Claus and Fitzgibbon 2005), has been developed. In contrast to other existing methods, RFM is general enough to model several distortions with a synthetic description through 18 DOFs. The STC foreseen operative temperature range is $-10/+30°C$, all the mirror components and the OB have been made by using the same material (aluminum) to allow for automatic temperature compensation (Da Deppo et al. 2018). The RFM model was used to define the geometrical distortion of all the STC filters, for two different optical bench temperatures, i.e., 275 K (COLD) and 295 K (HOT). Until the commissioning phase at Mercury in 2025, the focal length, boresights, rotation matrices, and RFMs associated to each filter, representing the definition of the Instrument Kernel (IK) of STC, will be defined by the on-ground measurements. The determination of the geometrical model of each filter, at a specific temperature, will be derived by interpolating the data obtained at the two measurement temperatures.

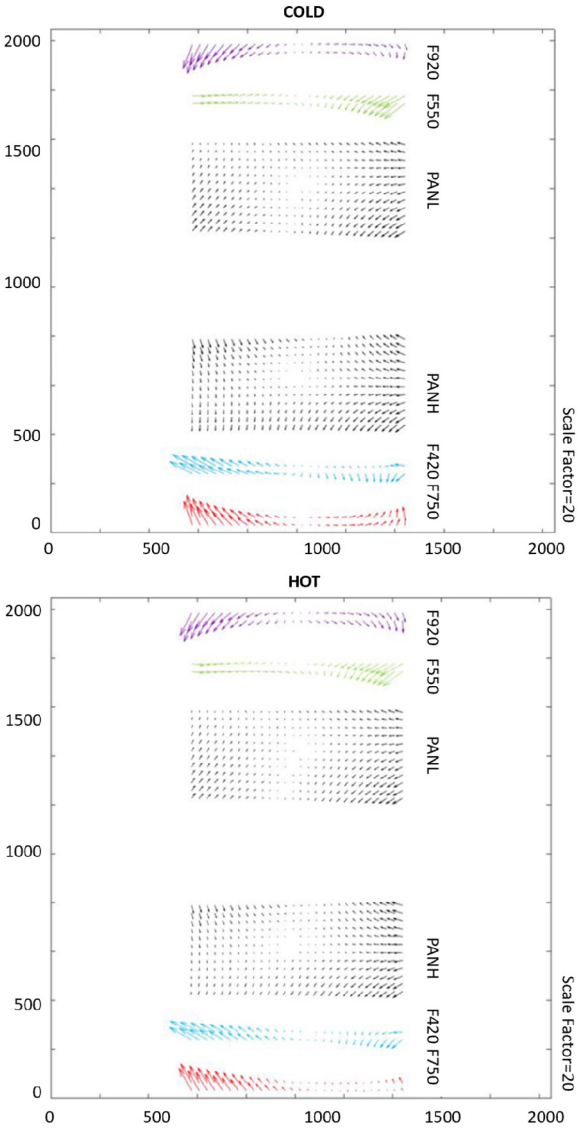

Fig. 16 Distortion modeled by RFMs on the six filters of STC. Vectors show the transformation from the distorted to the ideal image: (a) the COLD and (b) HOT cases

The model guarantees residuals uniformly distributed on the FPA with a mean value of 0.096 px and a standard deviation of 0.06 px (with a repeatability of the setup being better than 2 arcsec). In Fig. 16, the distortion modeled by the RFMs are shown for both the COLD and HOT cases.

7.3 Dark Measurements

7.3.1 Dark vs. Detector Temperature

For the STC channel, the dark current (see Fig. 17) has been measured as a function of the integration time and FPA temperature. ITs between 400 ns, i.e., the minimum IT that can

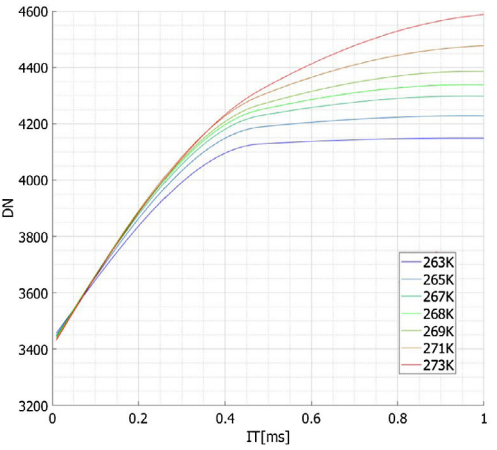

(a) .

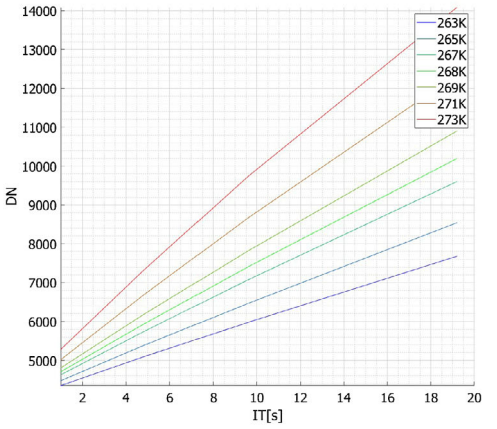

(b) .

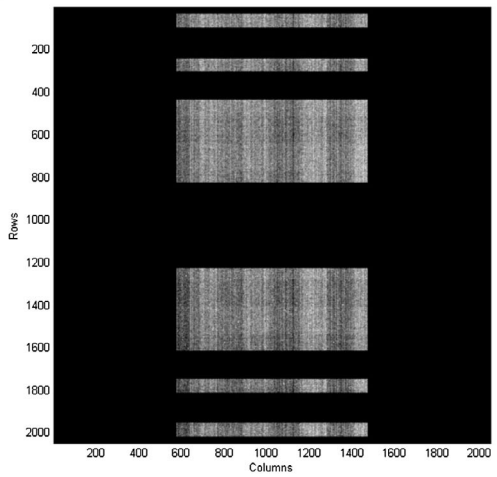

(c) .

Fig. 17 Mean detector dark current as measured in the temperature range of 263-273 K in 2-K steps depicted as a function of integration time (a & b). The plot in (a) shows The dark current is shown for integration times from 400 ns to 0.96 ms (a) and for integration times from 1 s to 19.6 s (b). The fixed-pattern noise of the detector is also depicted (c)

Table 11 Principal characteristics of the dark images. All the parameters are defined in DN according to A/D conversion of 14 bits/pixel. The main conversion parameters are reported

Temperature	263K	268K	273K
DSNU (IT < 10 ms)	<133.7 DN	<135 DN	134.4 DN
DSNU (IT > 10 ms)	<360 DN	<400 DN	<440 DN
RON (IT < 10 s)	7 DN	10 DN	15 DN
RON (IT > 10 s)	17 DN	23 DN	25 DN
Conversion capacity	21 μV/e^- typical		
Saturation charge capacity	<100000 e^-		
Average IG	7 e^-/DN		
Operability	99.63%	99.70%	99.88%

be commanded, and 19.2 s have been used. FPA temperatures in the range of 263-273 K, around the nominal value of 268K, have been tested.

7.3.2 Dark Signal Non Uniformity (DSNU)

STC has an FPA (Mills et al. 2009) housing a Hybrid Silicon PIN (Si PIN) detector with a 100% fill factor and backside illumination. This detector provides a QE higher than 80% over the entire 400-900 nm spectral range, but features a high FPN. The pixel full well is of the order of 10^5 electrons. The average Inverse Gain (IG), which is the number of electrons corresponding to one DN, has been estimated to be about 7 electrons/DN and is slightly pixel dependent. More precisely, the DSNU, defined as the standard deviation of a dark image, is limited to 135 DN corresponding to 20.8 mV for all the dark images acquired for ITs shorter than 10 ms independent of temperature.

At nominal temperature, RON is limited to 70-e^- RMS for short ITs and reaches 170 e^- for the highest IT. The detector RON and Operability are described in Table 11. A pixel was considered operable if the measured response is within a range of 3-σ with respect to the mean response of the array.

7.4 Radiometric Calibration

The radiometric calibration can be performed after the characterization of the detector dark current. A known uniform radiance source, i.e., an integrating sphere (IS), is used as input and the relation between the IS radiance (in physical units) and the values in DN detected can be calculated. The radiometric calibration function has been derived for each pixel. Figure 18 represents the mean values of the radiometric function in the detector linearity range, for each filter of the STC detector. To calculate the error that affects the measurement, the uncertainty of the integrating sphere, the detector efficiency, the filter transmittance, and the optics transmittance have been taken into account. The relative error calculated for the radiometric function span from 21% to 28%.

The radiometric function obtained has been checked with a test image. Figure 19 shows a test image taken with one of the panchromatic filters before and after the radiometric calibration. The "weft-effect" visible in the left-side image is the PRNU. After the radiometric calibration, this effect disappears, so that the final image represents the actual flux coming from the object observed and detected by the CMOS detector.

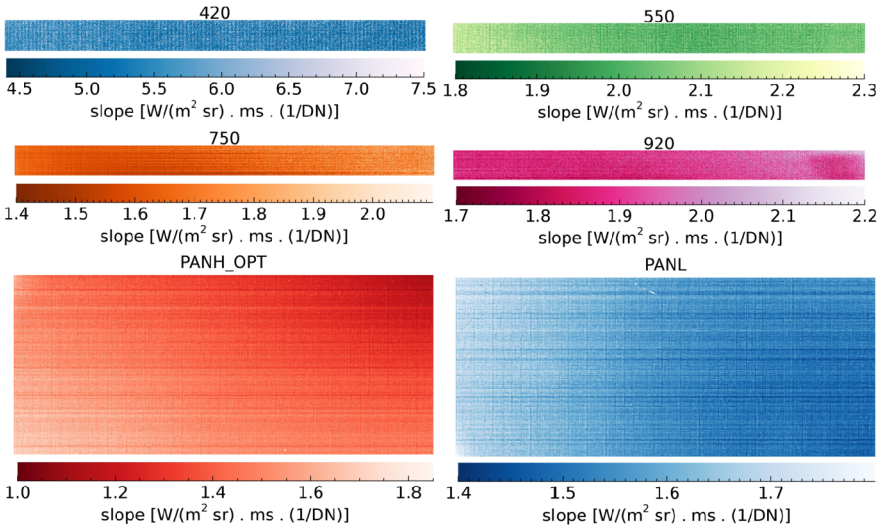

Fig. 18 Mean values of the slopes of the radiometric function in the linearity range for each filter of the STC detector. For each filter, two stripes are depicted. The upper stripe corresponds to the area covered by the filter on the detector, where the color shows the calculated values of the slope. The bottom stripe corresponds to the color coding

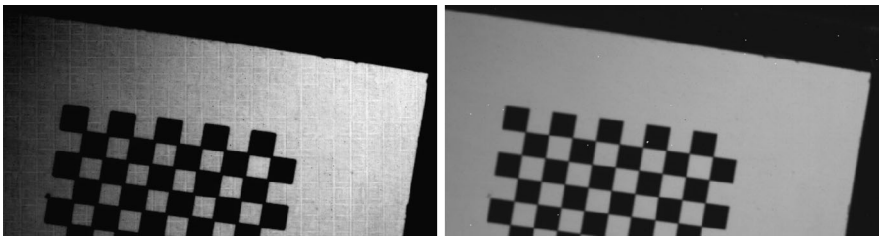

Fig. 19 A panchromatic image before (left) and after the radiometric calibration (right)

7.5 Spectral Calibration

The spectral calibration consists of the determination of the transmittance curve that characterizes the STC filter performance. The theoretical transmittance curve has been obtained by measuring the filters before mounting them in the optical system (dashed lines in Fig. 20). The wings of the transmittance function are the ascending and descending parts of the curve.

The data have been acquired by dividing each filter into three sub-windows, which illuminate the left-side, central, and right-side part of each filter, respectively. For each subwindow, a series of images has been taken. The wavelength of the light-beam spans the band width of each filter with a step that differs for the PAN and BB filters. The images have been acquired with two different integration times: a long IT for the wings of the transmittance function and a short IT for the plateau region.

In order to obtain the transmittance curve, it is necessary to characterize the input source. A spectroradiometer has been used to calibrate the input source, i.e., to verify that the wavelength of the monochromator corresponds exactly to the chosen one. The results obtained for the STC spectral calibration response are shown in Fig. 20. The DN/ms values mea-

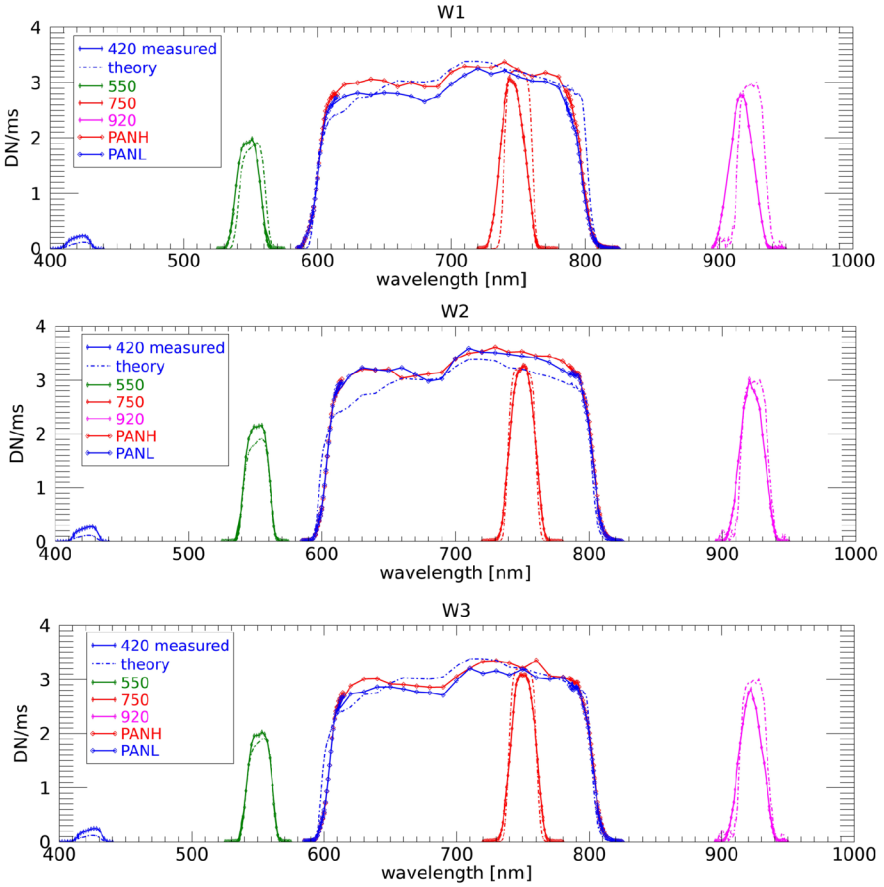

Fig. 20 Comparison between the flux per unit of time detected by the CMOS sensor and those estimated with the theoretical transmittance curve. The titles "W1", "W2", and "W3" refer, respectively, to the left-side, central, and right-side sub-windows. The solid lines refer to the measured flux per unit of time, whereas the dashed lines represent the values obtained with the theoretical transmittance curve

sured by the detector as function of the wavelength are shown. The transmittance curve of all filters is normalized for the IT of acquisition. The three plots are named "W1", "W2", and "W3" and refer, respectively, to the left-side, central, and right-side sub-window used to illuminate each filter. The solid lines show the flux values measured, whereas the dashed lines represent the DN/ms obtained with the theoretical transmittance for each filter.

The transmittance curves obtained for W1 and W3 are slightly shifted in wavelength with respect to the theoretical ones. In fact, the transmittance properties of each filter depend also on the incidence angle of the incoming light. For a detailed analysis, see Slemer et al. (2019b).

7.6 Stereo Validation

STC is based on a new and innovative concept of stereo camera both for original optical design and for the stereo acquisition mode, based on the push frame. This is the reason why a stereo validation on ground was required to verify the capability of providing stereo pairs

Table 12 Main geometrical parameters of the Mercury acquisition (upper part) and the scaled SVS (bottom part): Ground Sample Distance (GSD); camera-target distance along the nadir direction (Z); accuracy in height determination (Vertical accuracy); and stereo baseline (B)

Mercury scale	
GSD (m/pix)	50
Z (km)	400
Vertical accuracy (m)	80
B (km)	313
Focal length (mm)	95.2
Stereo validation setup scale	
GSD (mm/pix)	0.095
Z (m)	1.51
Vertical accuracy (mm)	0.19
B (m)	1.17
Focal length (mm)	170

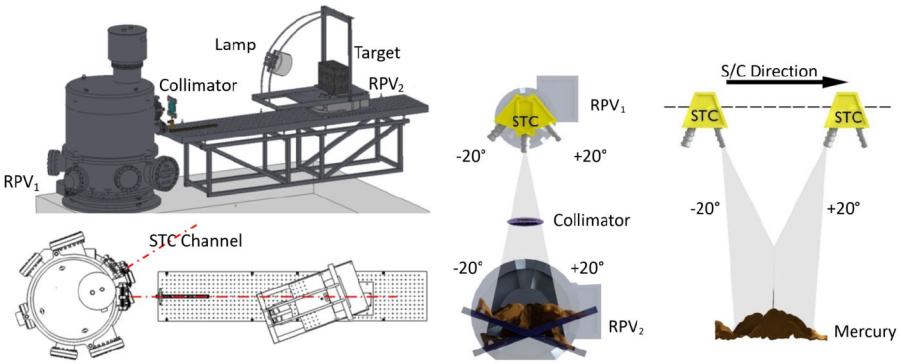

Fig. 21 Stereo validation setup (left). The halogen lamp is mounted on the rotational stage 2 where the target sample is positioned. A collimator, in front of the TVC, mounted on the rotational stage 1, completes the optical system. Laboratory simulation (right) of STC observing with forward channel and backward channel at periherm by means of the SVS. Two rotational stages rotate the STC FM and the target

for the consequent generation of the DTM. The stereo validation procedures have been realized in laboratory with a specific Stereo Validation Setup (SVS) to give a much greater confidence for the novel instrument design and to obtain an on-ground verification of the actual accuracies in obtaining elevation information from stereo pairs. The SVS is a combination of optical and mechanical components that allows the indoors reproduction of the instrument observing conditions: the same object area is imaged first by the forward-looking channel and, in a second moment, by the backward-looking channel. The reduction of the observing distance involves a scaling of the instrument requirements in terms of horizontal resolution (proportional to the ratio between the in-flight and the indoors target distance) and of vertical accuracy (Simioni et al. 2014) (see Table 12).

The main components of the SVS (Fig. 21) are:

– a collimator lens (achromatic doublet with focal length of 1000 mm and with a diameter of 80 mm) that collimates the light rays coming from the target;
– a motorized rotation stage which simulates the stereo angle of STC;
– a rotation stage for the simulation of active channel's relative point of view;

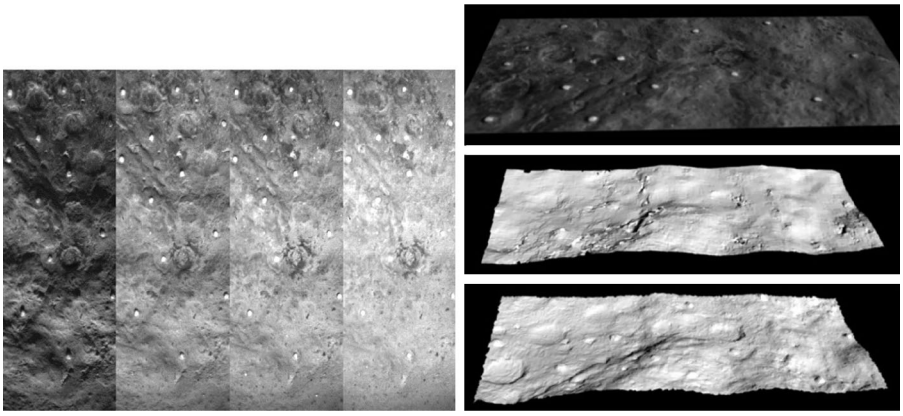

Fig. 22 The effect of four different illumination conditions for the anorthosite sample (left), with incidence angles of 10°, 30°, 50°, and 70° from left to right. The image obtained by one STC channel of the anorthosite target (top right), the photogrammetric DTM (middle right), and the DTM generated by the laser scanner (bottom right)

– a target positioned on the rotation stage;
– a light source mounted over a curved rail system conceived to rotate together with the target support plate, maintaining a constant lighting condition.

Everything is mounted on an optical bench making the integration with the OGSE easier. The indoors simulation of the spacecraft trajectory (for the sake of simplicity only the periherm is considered) is provided by the two high-precision motorized rotation stages. The support has been designed in order to reproduce some of the possible incidence angles of light (10°, 30°, 50°, 70°), corresponding to the possible solar rays incident on the Mercury surface, when the spacecraft is at periherm. A series of stereo pairs of an anorthosite stone sample and of a modelled piece of concrete, acquired in calibration clean room under the four different incidence angles (Fig. 22), have been processed in the photogrammetric pipeline using image correlation for the 3D model generation (Re et al. 2017). A series of white pins are visible on the image pairs set. The pins attached to the target surfaces allowed an easy, accurate, and unambiguous identification of Ground Control Points (GCP) both in the images and in the reference DTM. The GCPs have been useful to estimate the exterior orientation parameters by a bundle block adjustment procedure.

The stereo reconstruction validation has been performed by comparing the STC photogrammetric DTMs to a high-resolution laser-scanning 3D model of the stone samples as reference data. The latter has a much higher precision (ca. 20 μm) than the expected in-lab STC DTM (190 μm). The processing parameters have been varied in order to test their influence on the DTM generation accuracy. The tests suggest that the range of illumination angles (from 50° up to 70°) provides better accuracy and coverage of the 3D products, while, at the same time, meeting some of the requirements of the scientific community working on 2D images. The obtained Root Mean Square Error (RMSE) values are all well below the 190 μm that represents the requirement for STC at the breadboard scale, in the range of 60-95 μm. The same results can be converted to the Mercury scale by providing a consistent indication of the estimated accuracy in the determination of the planet's topography. The vertical accuracy can be expected to be in the range of $25 - 40$ m, considering a pixel on ground of about 50 m computed at 400 km from the surface (periherm). The stereo pairs acquired by means of the SVS have been also used to test the effects of the compression

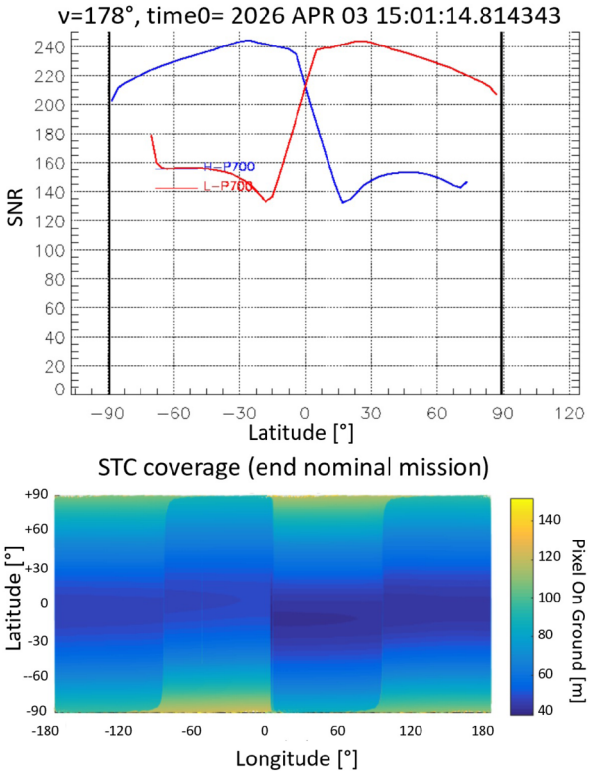

Fig. 23 Examples of simulator outputs. The SNR calculated for one orbit for the panchromatic filters (left) and the on-ground coverage at day 352 (right), corresponding to the end of the nominal mission

algorithm, implemented in the ME, on the accuracy of the DTM produced by dense image matching. In a previous work (Re et al. 2017), it has been demonstrated that the DTM degradation due to higher compression ratios would be acceptable and the consequent savings of the data volumes might be compensated by a higher number of images of the same regions and by applying a different observing strategy.

7.7 Optical Parameters and Performance

The measured mean optical MTF is 0.64 (@50 lines/mm), including the detector sampling. It achieves a minimum value of 0.57 on the 550-nm filter and a maximum value of 0.74 on the 750-nm one. The PSF of the STC telescope has been measured at the nominal operating temperature by the dithering technique (10 times of oversampling) using a 50- μm diameter pinhole. The derived PSF calculated for the center of the PANL filter is slightly elliptical with a FWHM of 1.38 and 1.49 pixels, including diffraction effects. Dithering will not be used in flight.

The main STC optical parameters are summarized in Table 4. The acquisition performance of the instrument can be evaluated via simulation (Simioni et al. 2019b; Slemer et al. 2020). An ad-hoc software simulator has been built using the Spice Kernels and considering the Mercury surface reflectance derived by the Hapke model and the STC channel characteristics (Hapke 2002, 2012). The simulator helps to define the integration time to be used for each MPO orbit, and to calculate the related expected SNR and also the on-ground pixel size, during the entire BepiColombo mission lifetime. The SNR (Slemer et al. 2019c) (see Fig. 23

Table 13 Sequence of calibration activities performed during the development of the VIHI instrument

Phase	Measurements	References
1a	System Requirements Validation	Not available
1b	Full-Well Capacity (T=210, 220, 225 K) Dark Current (T=210, 220, 225 K) Noise (T=210, 220, 225 K) 1/F Noise (T=210, 220, 225 K) Conversion factor (T=210 K) High-Low Flux response (T=210, 220, 225 K) Wavelength response (T=210 K)	Hello et al. (2009)
2	Boresight and Reference mirror Spectral Calibration Geometry Calibration Flat field Radiometric Calibration Linearity Internal Calibration Unit	Capaccioni et al. (2013) Da Deppo et al. (2014) Filacchione et al. (2017) Altieri et al. (2017) Filacchione et al. (2018)
3	Radiometric Cross-Calibration Radiometric Absolute Calibration Straylight Spectral Check on Mineral Samples Internal Calibration Unit	Poulet et al. (2015)

left panel) is obtained by considering the photon shot noise, the RON and DC: the nominal IT has been defined as the minimum between the IT needed to reach the best possible SNR, still remaining inside the linearity region of the filter response, and the smearing time. See Fig. 23 for an example of the simulator output for the on-ground coverage at day 352.

8 VIHI Calibration

The VIHI pre-launch calibration has been performed in three successive steps aiming to fully characterize the instrument performance. The first set of measurements were dedicated to measuring the VIS-NIR detector's performance with the scope to verify accordance to system requirements: these activities have been completed at the Raytheon Video Systems premises (detector manufacturer) to select the Flight and Spare models from the production lot and in LESIA-Meudon Observatory to further characterize the two detectors. The next set of measurements were completed on the integrated VIHI optical head at operative temperatures in Leonardo SpA with the scope to fully characterize the optical performance. Finally, tests at system level, e.g., with all three optical channels (HRIC, STC, VIHI) and Main Electronics integrated and stabilized at operative temperatures, were carried out at IAS, Orsay. A summary of the measurements completed in each phase is reported in Table 13. Since a detailed description of the laboratory setups used to perform the calibration measurements were already discussed earlier (Hello et al. 2009; Da Deppo et al. 2014; Filacchione et al. 2017; Altieri et al. 2017; Poulet et al. 2015), we focus here on the determination of the key data parameters necessary for the scientific conversion of the raw data numbers into physical units of spectral radiance.

Table 14 The VIHI Spectral Calibration Key Data Parameters, including the keystone and smile aberration estimates as explained in the text

Number of spectral bands	256
Full spectral range	408.03 - 2006.34 nm
Spectral sampling (at band b)	$6.248 + 6.244 \cdot 10^{-4} \cdot b + 2.747 \cdot 10^{-6} \cdot b^2$ (nm)
Spectral response function	$6 \leq \text{FWHM} \leq 7$ nm
Keystone maximum shift	≤ 2 nm
Smile maximum shift	≤ 2 nm

8.1 Spectral Calibration

The VIHI spectral calibration, including the full spectral range, sampling, and spectral response function, is determined by acquiring calibrated light emitted by a monochromator and by comparison with the spectral sources of the internal calibration unit. The monochromator scan is performed continuously across the entire spectral range at steps of 1 nm by illuminating the entire spectrometer's field of view with a collimated beam. The measurements and related data processing are described in detail in Altieri et al. (2017). The resulting spectral parameters are summarized in Table 14.

The VIHI spectral sampling is not constant: it follows a quadratic dispersion along the band axis. As a result of this effect, the minimum sampling interval is 6.248 nm (band = 0) and the maximum one is 6.451 nm (band = 181). The spectral response function has Gaussian-like shape across the entire spectral axis (see Fig. 24) with a variability range of 6 nm $\leq$ FWHM $\leq$ 7 nm. Some fluctuations of the FWHM visible near 1400 and 1900 nm are caused by water vapor absorption residuals introduced by the ambient air along the optical path from the monochromator to TVC. Imaging spectrometers are affected by two typical aberrations: keystone and smile effects. The ideal optical response is such that the optical beam is focalized in an area matching the detector's spatial (along sample axis, or s) and spectral dimensions (along band axis, or b), Conversely, a real instrument response shall be affected by the smile (variable curvature of the slit image across the spectral range) and keystone aberrations (a band-to-band spatial misregistration). As a consequence of these effects, the resulting spectral profiles would appear smeared by mixing the spatial and spectral information on the single pixel and degrading the overall response. The maximum distortion caused by the aberrations (keystone, smile) as measured on the VIHI response is $\leq$2 nm across the full spectral range, and within the scientific requirements (see Table 14).

8.2 Geometric Calibration

The instrument geometric performances are determined by means of controlled, subpixel spatial scans of point sources with the aim to measure the FOV and the Instantaneous Field of View (IFoV) along and across the slit direction. A detailed description of the measurements setups and data processing is reported in Filacchione et al. (2017). In the slit (pixel) function, an illuminated test slit is placed parallel (perpendicular) to the VIHI slit during the scan. The collimated optical beam emitted by the test slit is moved at subpixel steps for each acquisition with the aim to oversample the angular resolution. This method has been already used to characterize geometrical performance of similar VIS-IR imaging spectrometers, like

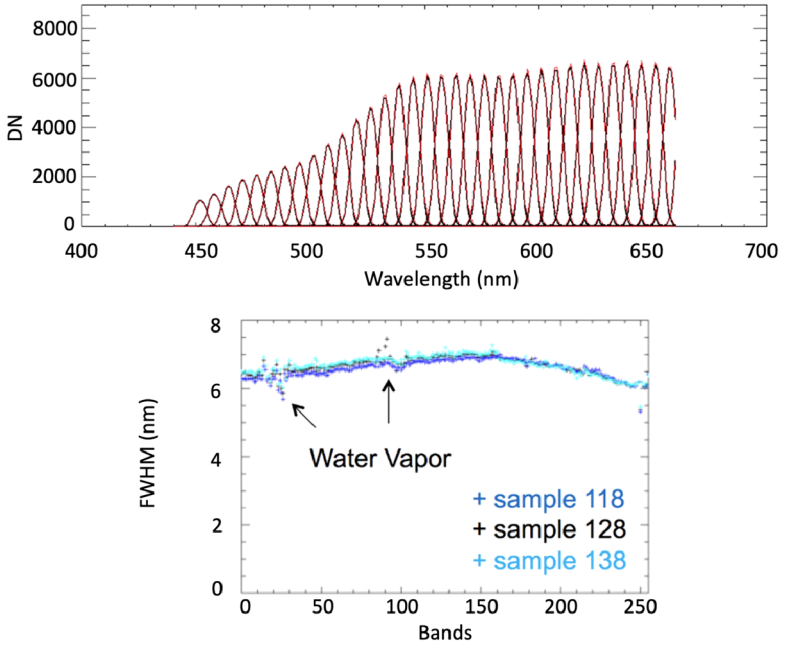

Fig. 24 Signal of the monochromator (top, black lines) acquired during the spectral scan at boresight (sample s = 128) and spectral response function (red lines) derived from a Gaussian fit for the spectral range of 440 ≤ bands ≤ 660 nm. Variability of the spectral response width (bottom) at three samples along the spectral axis. Water vapor residuals are visible at bands ≈ 20 and ≈ 90. Adapted from Altieri et al. (2017)

Table 15 The VIHI geometric calibration key data parameters, where s represents the sample (pixel number along the spatial axis or slit) and b the band (band axis)

Number of spatial samples	256
FoV	3.62°
IFoV (slit function at b=151)	232.3 μrad at s=5 219.8 μrad at s=64 246,3 μrad at s=128 227.7 μrad at s=194 240.0 μrad at s=246
IFoV (pixel function at b=151)	254.7 μrad at s=5 249.7 μrad at s=65 250.6 μrad at s=128 247.7 μrad at s=195 253.5 μrad at s=250
MTF at Nyquist frequency (2.52 lines/mm)	0.47 (slit function) × 0.35 (pixel function)

VIRTIS on Rosetta (Ammannito et al. 2006) and JIRAM on Juno (Adriani et al. 2017). The geometric key data parameters are reported in Table 15. An example of the VIHI imaging capabilities is given by Fig. 25, where the image of a standard USAF mask is shown. This acquisition is used to derive MTF values.

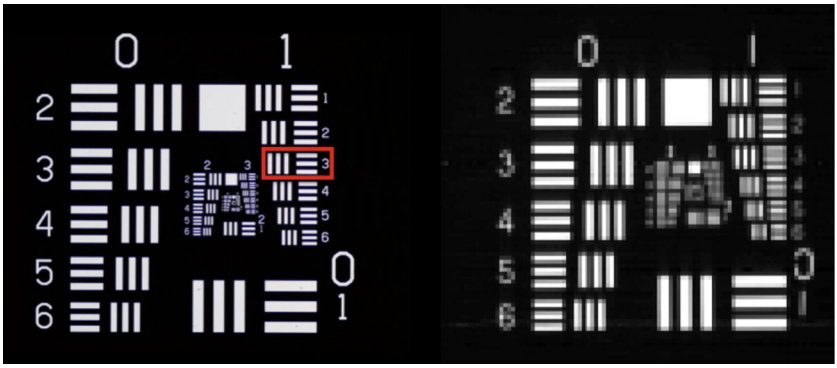

Fig. 25 USAF mask 1951 reference image (left). The pattern G = 1, E = 3 indicated by the red box corresponds to the VIHI theoretical frequency $f_{Nyquist}$ = 2.52 lines/mm. VIHI image of the mask (right) at wavelength λ = 590 nm. The VIHI slit (sample direction) is oriented towards the vertical axis and the image is acquired in time by scanning at one IFoV step along the horizontal axis. From Filacchione et al. (2017)

8.3 Radiometric Calibration, Linearity and Flat Field

The VIHI radiometric response is determined by acquiring the flux emitted by a radiometrically calibrated integrating sphere (Da Deppo et al. 2014) and by using the methodology discussed in Filacchione et al. (2017). The acquisitions are performed in a wide range of input spectral radiance (from 150 to 500 W m^{-2} μm^{-1} sr^{-1} at λ = 0.98 μm) and integration times (from 68.5 μs to 0.5 s) in order to simulate the expected operative conditions occurring during the mission at Mercury. Moreover, the instrument response has been characterized as a function of the expected operative temperature range of the detector by stabilizing it at $T_{cold} = 210.1K$, $T_{nominal} = 219.9\ K$, $T_{warm} = 225.0\ K$. In particular, for each temperature, the corresponding median dark-current signal across the detector is determined (Fig. 26). To perform radiometric calibration computation, the corresponding dark-current value is subtracted from the signal measured on the integrating sphere.

Given the good linearity of the detector, as seen in the dark-current trends shown in Fig. 26, the VIHI responsivity $R(s, \lambda)$ on sample s and wavelength λ is computed as:

$$R(s,\lambda) = \frac{DS(s,\lambda)}{S(\lambda)\cdot\tau(\lambda)\cdot t} \tag{1}$$

where DS is the difference between the integrating sphere signal and the background measured by closing the integrating sphere aperture at the same integration time t, S is the radiance emitted by the IS, and τ is the optical transmittance of the setup (collimator, folding mirror, and TVC's entrance window). The responsivity shown in Fig. 27 is computed for all spatial pixels by exploiting the high spatial homogeneity of the beam emitted by the integrating sphere: according to Da Deppo et al. (2014) the uniformity of the beam is in fact better than 99.2 % for the 500 W m^{-2} μm^{-1} sr^{-1} flux case and better than 97.9 % for the 150 W m^{-2} μm^{-1} sr^{-1} at λ = 0.98 μm. Given the high spatial uniformity of the integrating sphere beam, within the field of view, the derived responsivity array R(s, λ) includes also the flat-field, e.g. the pixel to pixel relative response (Filacchione et al. 2006). With the availability of the responsivity function and dark-current statistics, it is possible to derive the instrumental Noise-Equivalent Spectral Radiance (NESR) which corresponds to the minimum spectral radiance in W m^{-2} μm^{-1} sr^{-1} at which VIHI is sensitive, e.g., the

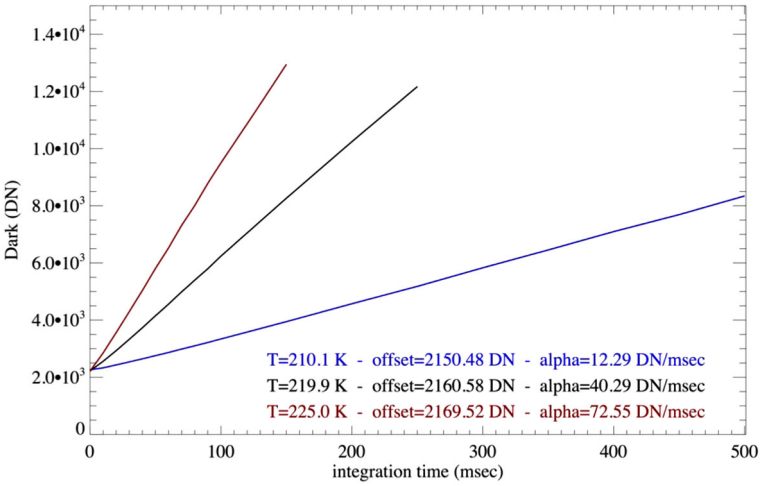

Fig. 26 Trends of the VIHI median dark-current values measured on the full detector for the temperature cases $T_{cold} = 210.1\ K$, $T_{nominal} = 219.9\ K$, and $T_{warm} = 225.0\ K$. The offset and dark-current rate (alpha) as a function of integration time are calculated by means of a linear fit are shown for each case. Detector's saturation occurs at about 13200 DN. From Filacchione et al. (2017)

spectral radiance corresponding to a signal of 1 DN (Filacchione et al. 2018). This is the minimum signal which can be measured by the detector. The NESR is defined as the ratio of the standard deviation of the sum of the dark current and external background divided by the responsivity:

$$NESR = \frac{STDEV[D(\lambda) + B(\lambda)]}{R(\lambda)} \tag{2}$$

where $D(\lambda)$ is the dark current, $B(\lambda)$ is the background, equivalent to the sky, and $R(\lambda)$ is the instrument's responsivity at wavelength λ. As a consequence of the strong dependence of the dark-current rate on the detector's temperature which increases from 12.29 to 40.29 up to 72.55 DN/msec at T_{cold}, $T_{nominal}$, T_{warm}, respectively (Fig. 26), the NESR deteriorates at longer integration times and higher temperatures, because it depends on the fluctuations of the dark current. In these conditions, VIHI shows a worse sensitivity to lower radiances. For a typical 50-ms integration time at $\lambda = 1.3$ µm, where the instrument's response is at its maximum, the resulting NESR is equal to $6 \cdot 10^{-3}$ W m^{-2} µm^{-1} sr^{-1} at $T_{cold} = 210$ K, $1.5 \cdot 10^{-2}$ W m^{-2} µm^{-1} sr^{-1} at $T_{nominal} = 220$ K, and $2.5 \cdot 10^{-2}$ W m^{-2} µm^{-1} sr^{-1} at $T_{warm} = 225$ K. In all three operative temperature cases, the allowable NESR upper values are limited by the detector's full-well capacity (2 Me$^-$ per pixel) corresponding to a saturation level of about 13200 DN after digitalization of the signal.

8.4 Internal Calibration Unit

The capability to obtain high-quality hyperspectral data of the hermean surface largely depends on the reliability of the calibration process. Whereas an accurate instrumental calibration can be completed during the on-ground tests, several effects can occur in flight conditions, resulting in possible changes of the instrumental response. Among these are the aging of the optical surfaces, the interaction with charged particles in the hermean orbit and in cruise, and the degradation of the focal plane performance. For these reasons, VIHI is

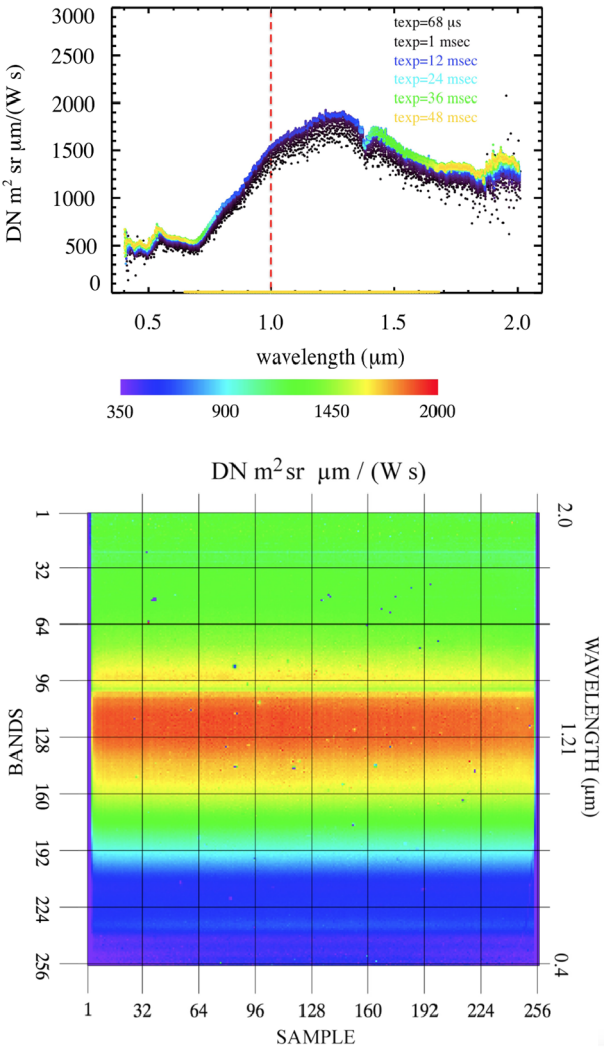

Fig. 27 The VIHI responsivity at sample = 128 (top) for integration times between 68 µs and 48 ms and the VIHI responsivity array (bottom) as derived for the integration time $t = 10$ ms. From Filacchione et al. (2017)

equipped with an internal calibration unit (ICU) basically consisting of a 45° (respect to the optical axis) semi-reflective window placed on the telescope pupil which can be illuminated by two different sources: a white LED, optimized for the visible spectral range and an IR lamp (Capaccioni et al. 2010, 2013). Both sources are powered by stabilized currents in order to guarantee a high reproducibility of their fluxes. The signal coming from the source is diffused and then collimated to illuminate the whole optical pupil, allowing to perform several instrumental checks during the development of the mission:

– Spectral response check. This task becomes possible by measuring the spectral position of some well-defined features of the LED's emitted signal; moreover, the IR lamp is equipped with a didymium filter with the scope to introduce several absorption features on the measured spectrum. As the spectral positions of the absorption bands of the filter and the LED spectrum are spectrally characterized during on-ground tests, it is possible to use these features to estimate the occurrence of possible changes during the mission.

– Flat-field check. As the lamps' spots illuminate in a uniform way the optical pupil, the resulting signals on the focal plane are roughly homogeneous along the spatial direction; by comparing in-flight with on-ground acquisitions of the two lamps, it is possible to verify if any changes are occurring on the flat-field response.
– Monitoring the evolution of defective pixels. Their response and number could change as a consequence of the interaction of cosmic/solar charged particles on the detector.
– Relative radiometric response check. The instrumental radiometric response can be monitored because both sources are powered by on board PU with stabilized currents to have a reproducible photon flux during the mission. Again, the comparison with on-ground acquisitions made with the same in-flight conditions can be used to compensate for any changes which could occur in the instrumental responsivity.

The ICU will be operated by executing a dedicated mode on the onboard software which will be commanded when the instrument boresight is oriented towards a dark source (S/C internal bus during the cruise); sky or Mercury's surface during nightside portion of the orbits). In this mode, the following sequence of acquisitions are commanded: 1) Readout offset: acquisition of the detector signal with a null integration time. In this condition, it is possible to evaluate the contribution of the electronic chain on the signal (A/D converter noise, electronic offsets and gains). 2) Dark frames: acquisition of the dark-current signals measured with the spectrometer's shutter closed at integration times t_{LED} and t_{Lamp}. This frame contains also the internal background, e.g., the contribution of the spectrometer's mechanical structure to the signal. 3) LED frame: acquisition of the VIS LED source signal with the shutter open at integration time t_{LED}. 4) IR lamp frame: acquisition of the IR lamp source signal with the shutter open at integration time t_{Lamp}. 5) Dark frame: acquisition of the dark-current signal measured with the shutter closed at integration times t_{LED} and t_{Lamp}. This is a repetition of the step 2 and is necessary to evaluate possible thermal drifts of the dark and background during the sequence. Depending on the availability of the data volume, a similar sequence can be repeated several times to improve the statistics. The reference signals of the LED and IR lamp at the slit's center and across the entire detector acquired during the pre-launch calibrations are shown in Figs. 28 and 29, respectively.

9 Electrical Ground Support Equipment

The SIMBIO-SYS Ground Segment software has two main objectives: the conversion of the telemetry packets into the PDS4 products (TM2RAW pipeline) and to check the consistency of the telecommand timeline and the data produced. The software will also generate the event list and a report of the errors. Figure 30 shows the block diagram. The spacecraft sends the packets to the EDDS server (ESA Ground Operation System's Data Dissemination System) that orders them, following the generation time, and provides them to the instrument team in XML format.

The XML file, produced by the EDDS, is one of the pipeline inputs. The pipeline is designed by following a modular programming approach. Each module has a specific functionality and the communication between the modules is based on files (Fig. 30).

The bash script simGen is the pipeline orchestrator. The execution is completely customizable by a command line or by a configuration file, useful for the automatic process. The main purpose of the software is the validation of the inputs and the configuration of the execution environment. During the input validation process, the software checks that all the required input files are present. The pipeline has two different branches: TM2RAW and

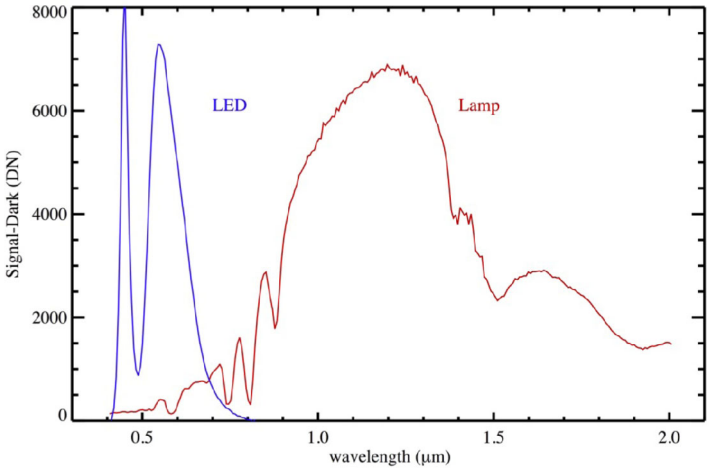

Fig. 28 The VIHI internal calibration unit reference spectral signals from the LED and IR lamp as measured at boresight (s = 128). Note the position of the absorption features on the LED and IR Lamp spectra used to check the spectral response stability. From Filacchione et al. (2017)

RAW2CAL. The former branch generates the raw data from the telemetry file, whereas the latter starts from the raw data and produces the calibrated data. Normally, the two branches work sequentially, but they can work separately, e.g., for checking or recalibration purposes. The inputs are different for each branch. At the time of writing the paper, the TM2RAW is the only branch completed and tested. The inputs of TM2RAW are: the telemetry XML file and the command history report of the SPICE kernels. The first one contains the packets coming from the spacecraft (data, housekeeping, events, and acknowledgment). They are stored in the file in the SCOSS 2000/CCSDS format and written in a hexadecimal system. If the file is not present, the pipeline exits with error. The Telecommand History Report contains all the commands sent to the instrument, with all the parameters, the execution time, and the univocal id of each TC. If this file is not present, the software produces a warning message and skips the process of cross correlation between the acknowledgment or TC errors and the command instruction. The last input is the SPICE kernels that contains the information to calculate the spacecraft position, the FoV of the channels and the parameters for the time conversions. If the kernel files are not in the input folder, the pipeline stops the process with an error message. The simGen script runs two main modules: simEvent and simAir:

– simEvent is a python module that filters the packets and selects only the events and the acknowledgments message. It produces a log file containing a brief description of the event and a correlation between the acknowledgment and the corresponding TC. To simplify the block diagram in Fig. 30, the module is not reported but is included in the generic "check" block.
– simAir is a C++ module. It reads all the telemetry files and splits the packet by the Application Process IDentifier (APID). Every packet is converted, the images are assembled and decompressed, the house-keeping are converted ito physical units using a LiteSQL database. Using the information in the header of the packets, an integrity and completeness test is performed. If the data is incomplete or damaged (e.g., corrupted telemetry file or handling of data gap or incomplete product), the software will set the missing pixels to a special value (-999) in order to complete the data.

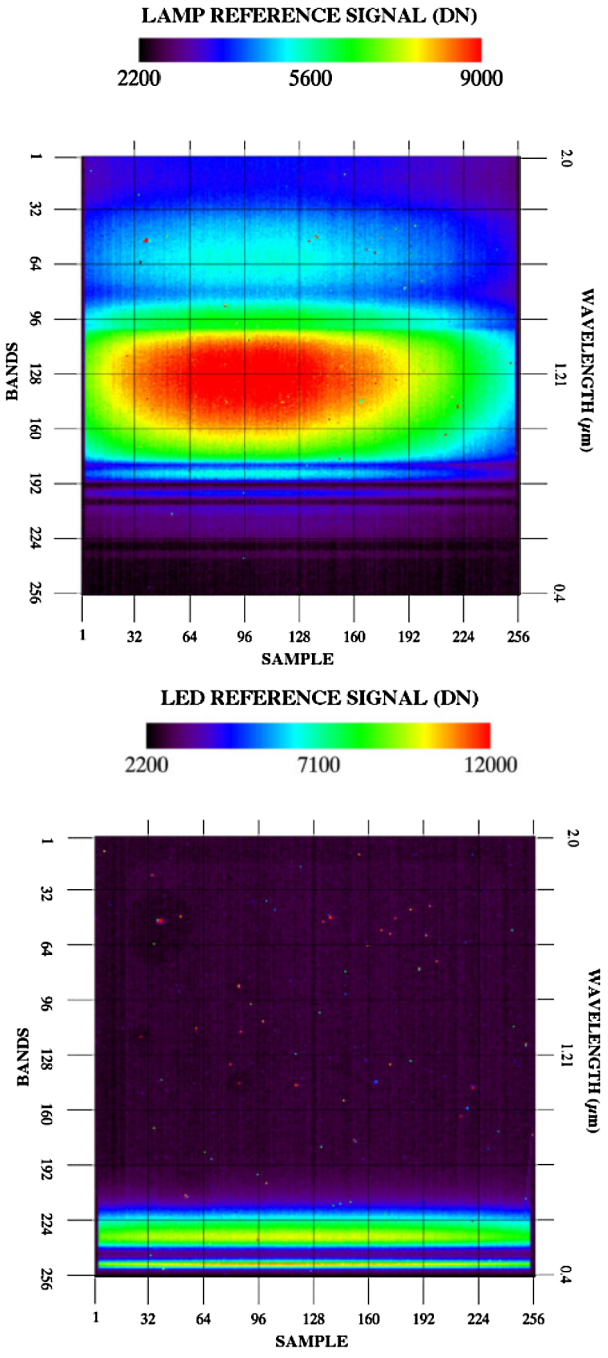

Fig. 29 Distribution of the VIHI internal calibration unit reference signals from the IR lamp and LED as measured on the focal plane. From Filacchione et al. (2017)

The pipeline will produce the output data in PDS4 format. The SIMBIO-SYS team, with the collaboration of the ESA SGS team, projects the structure of the PDS label and the parameters to characterize and contextualize the data as much as possible.

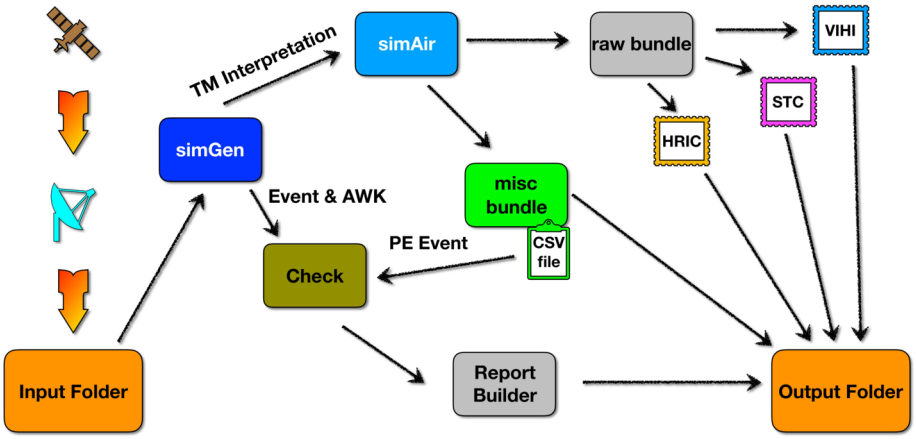

Fig. 30 Block diagram from the spacecraft to the PDS4 products

Table 16 Failed TCs

Channel	Failed TC
HRIC	10
STC	28
VIHI	0

The data coming from simAir are formatted in PDS4 format by a specific module. This module provides also a statistics file containing, e.g., the number of sessions and the number of acquisitions for each session. The PDS4 files are moved to the output folder. The statistics file and the event log are the input for the check module. This module performs some tests that are grouped in four categories:

- TC checks. The software uses as input the TC stack and extracts from it how many scientific sessions are planned, the id of each TC in the timeline, and the number of images that will be produced. The software cross-checks the output of the TC checks with the events file and verifies that all the telecommands planned are accepted and executed and, in the case of a failure, reports an error message.
- ME checks. The software uses as input the event file and the house-keeping (HK) file produced by the ME.
- PE checks. The software uses the HK files generated by the PE of each channel.
- Data checks. The software verifies that the generated products are the expected ones. If some anomalies are found, the software identifies the session with the missing data and reports the errors.

The check results are sent to a report builder that assembles all the information in human readable PDF file in the output folder.

During the NECP, 22 test cases were executed and, for each case, the EGSE performed the operations reported above. At the end, the EGSE identified 21949 TCs, including 597 science activations. Table 16 reports the failed TCs of each channel coming from the TC check. The TCs failed were analyzed to look for the reasons for the errors. Two types of problems were found. The first type is due to a command error: some acquisitions were

Table 17 Summary of images and data volume produced by each channel

Channel	# of images	Data volume [GB]
HRIC	7001	4.217
STC	20431	3.305
VIHI	37393	1.245

commanded on an area of the detector that was not compatible with the onboard software. The second type of error was due to a communication problem between the ME and the PE.

The TC failed, reported in Table 16, were analyzed to look for the reasons for the errors. Two problems were found. The first one is due to a command error, some acquisitions were commanded on an area of the detector whose shape was not compatible with the on-board software. The second source of error was due to a communication problem between the ME and the PE.

The ME and PE checks identified 1 ME error, with low severity label, 1 from the VIHI PE and 1 from HRIC PE.

SIMBIO-SYS produced 1163839 packets (110 lost during STC session) that were converted into 64825 images for a total amount of 8.767 GB. Table 17 reports the details for each channel.

10 Near-Earth Commissioning Phase

In November/December 2018, after the launch in 20 October 2018, the BepiColombo spacecraft underwent the initial commissioning phase, during which the health status and the monitoring of the expected performance of the spacecraft systems and scientific payload have been verified. During this phase, the SIMBIO-SYS instrument has taken advantage of a 3-day window to be switched on and to operate for the first time after the launch. The three channels of SIMBIO-SYS have validated their functionality through two kinds of tests:

- the SIMBIO-SYS health has been checked after the demanding launch phase;
- a long sequence of performance checks and measurements have been carried out (considering the available resources) to integrate and confirm the on-ground data.

The instrument was commanded to execute timelines simulating all the operational modes that will be performed during the scientific phase of the mission. In these simulations, both single-channel operations and/or simultaneous use of all three channels have been tested. In particular:

- Functional Tests. The SIMBIO-SYS functionality has been verified by means of dedicated procedures on the following elements:
  - ME, with the verification of
    - MAIN and REDUNDANT channel operability
    - loaded ASW version
  - all channels, the verification on the MAIN and REDUNDANT ME operability of
    - PE, TEC, and detector activation
    - memory/register status
    - science acquisition capability
- Performance Tests. The SIMBIO-SYS shall be verified by means of minimal performance procedures on the following elements:

* HRIC, with the measurements of
  - Compression module
  - Dark current
  - Spurious Charge (SC)
  - detector reset behavior
* STC, with the measurements of
  - DC campaign for the Color Mode and Global Mapping operation modes
  - SC
  - detector reset capabilities
* VIHI, with the measurements of
  - internal calibration unit performance
  - DC performance

The tests have been carried out by means of the execution of Flight Operation Procedure (FOP), On-Board Control Procedures (OBCPs), and Payload Direct Operation Requests (PDORs) properly prepared. In total, 11 FOPs, 10 PDORs, and 6 OBCPs have been used and grouped as follows:

– All functional tests together with the VIHI performance tests have been done by means of FOP;
– HRIC and STC performance tests have been executed by means of PDORs;
– ME and channel switch-on/off during performance tests have been done by means of OBCP.

Finally, NECP tests have also allowed the validation of the EGSE and data tools developed by the team for the conversion and visualization of the scientific and HK data.

10.1 HRIC Results

HRIC performed several image acquisitions during the NECP with the aim of checking the channel performance and to confirm the calibration measurements performed on ground during the AIV phase. Due to the S/C configuration, HRIC was unable to take images of light sources, thus the only parameters that were retrieved with dark acquisitions were the RON, the FPN, and the DC. In addition to these tests, we acquired similar images (window dimensions and integration times) at different compression ratios in order to check the impact of the compressor on image characteristics. We also performed a test reset to investigate if the detector is affected by noise drift when switched on with long times between acquisitions.

10.1.1 Test of Data Compression

Using some images obtained with the same integration times, we have performed some compression tests in order to evaluate the differences. We have used 5 values of the instantaneous bit rate (ibr) as 0, 1, 16, 32, 56. During this test, the same detector was used with the same integration time (96 ms) and 5 different values of the compression factors (instantaneous bit rate = 0, 1, 16, 32, 56 corresponding to the compression levels of bit-packing, lossless, 14, 7, and 3.5). Figure 31 shows the differences between the acquisitions considering that the average and the standard deviation on the pixel values are negligible for the acquired scene (almost uniform dark image). Analyzing the histograms, it is possible to note the reduction of the standard deviation with increasing compression factor. It means that higher compression smoothens the image spatial frequency by removing spikes in the frame.

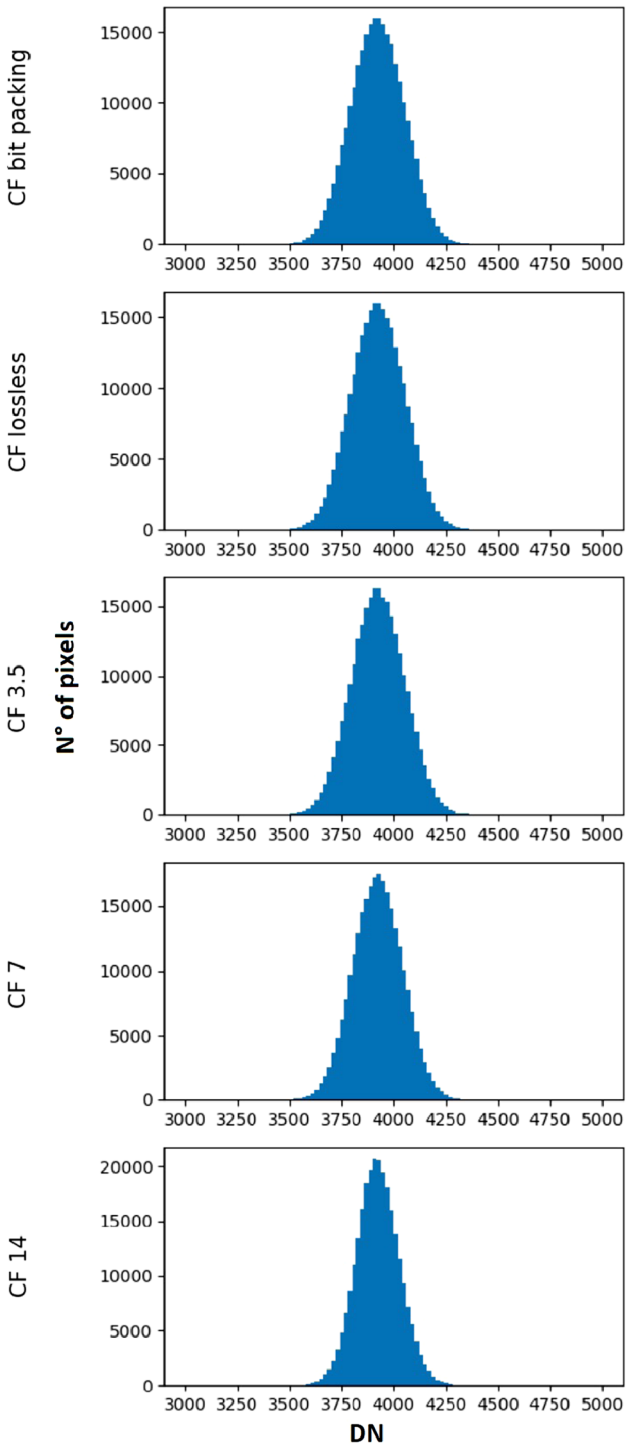

Fig. 31 Plot of the histograms of the analyzed frames at different compression factors

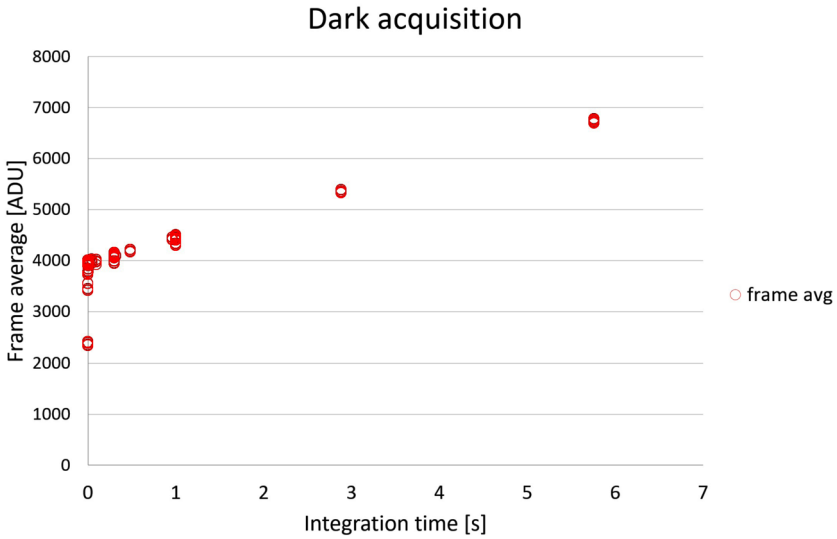

Fig. 32 Panchromatic DC trend, the average value of the frames acquired at different integration times. For each exposure time, several measurements (open circles) are reported, because 10 images have been acquired. The data are compatible with the behavior already observed during ground calibration, including the peculiar trend for IT < 0.05 ms (see Fig. 12)

10.1.2 Dark Measurements

During the dark test and measurements, the areas of the detector corresponding to the PAN, and to the three BB filters have been acquired with different integration times, starting from the minimum (400 ns in the configuration used for the ROIC) and increasing up to about 6 s. The values of the average of the PAN acquired frames are reported in Fig. 32. The trend shown in the plot is compatible with the trends measured during the calibration campaign on ground and reported in Della Corte et al. (2018). Using the data collected during the dark measurements, also the FPN and the RON of the detector have been checked with respect to the values obtained during the calibration campaign. The values obtained for both FPN and RON are in good agreement with the values obtained in Della Corte et al. (2018) (Fig. 33, Fig. 34). In particular, the histograms reported in Fig. 34 show that the RON mean value slightly decreases at higher integration times, confirming the data obtained during the on-ground test campaign.

10.1.3 Test Detector Reset

The outcome of this test indicates that the mean value of the detector pixels is stable with respect to the combination of integration and repetition times, with no drifts. The only difference between the series is due to the DC behavior. The test confirmed the results obtained during the on-ground test campaign where no issue on the HRIC detector reset have been raised.

10.2 STC Results

During the NECP phase, STC performed different tests to validate the calibration measurements performed on ground. The tests included the measurement of the FPN, DSNU, and

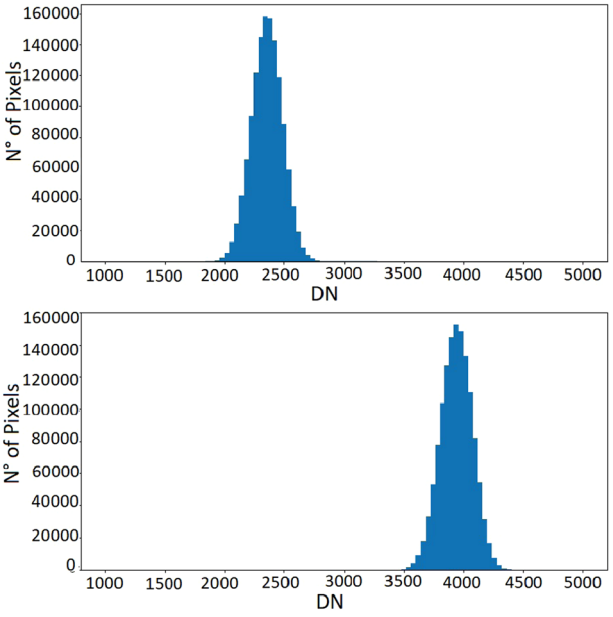

Fig. 33 FPN histograms averaged over 10 acquisitions, at the minimum integration time (top) and 48 µs (bottom)

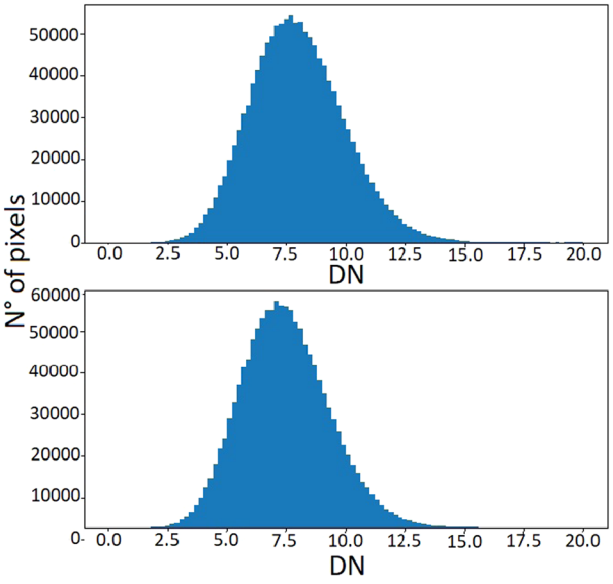

Fig. 34 RON histograms averaged over 10 acquisitions, at the minimum integration time (top) and 48 µs (bottom)

RON for different acquisition modes, among which there were the nominal ones of global mapping and color mode. The two acquisition modes consider the acquisition, respectively, of the two panchromatic filters and the broad-band filters. An example is shown in Fig. 35. As measured on ground, the DSNU is limited to 120 DN (for filter 750) and reaches maximum value on filter 920 (137 DN). The RON (for nominal integration times) has an upper limit of 9.3 DN. The comparison with on-ground images shows an uncertainty of 21 DN in the FPN.

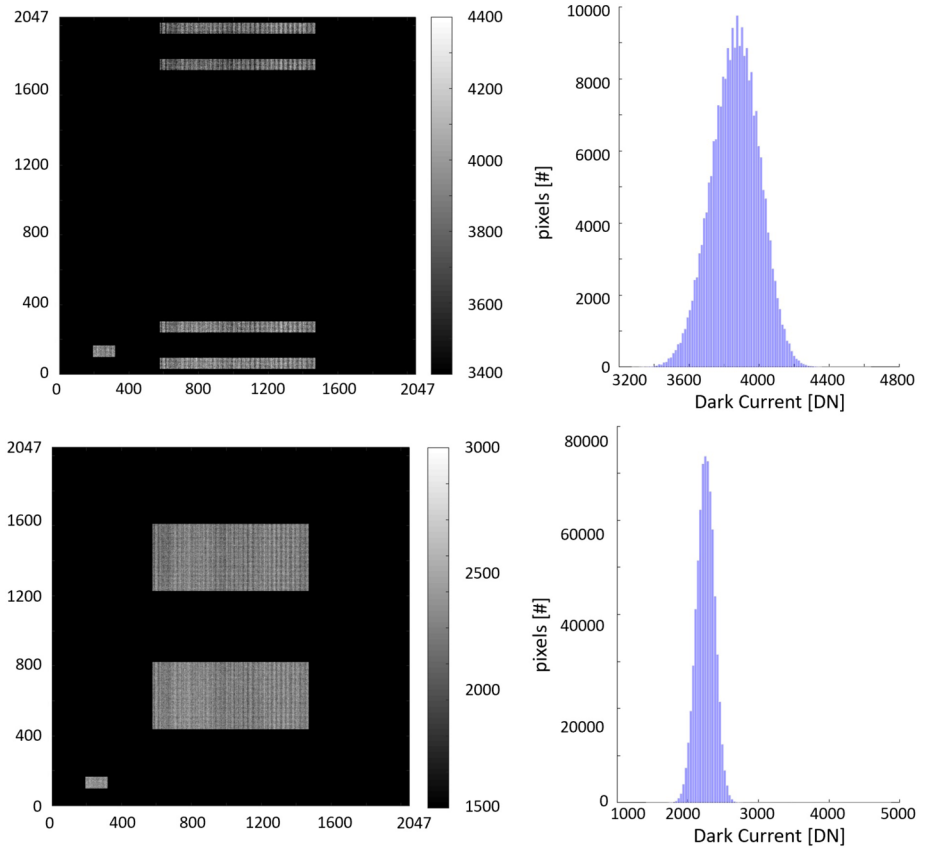

Fig. 35 Two examples of acquisition for STC during the NECP: the global mapping mode (top) and the color mode (bottom). The STC detector is shown on the left and the dark signal distribution on the right. In both cases, the histogram has a width around 800 DN corresponding to a foreseen standard deviation of 135 DN

10.2.1 Dark Measurements

The dark current has been measured for each pixel, considering different acquisition strategies. In particular, we tested the IT between 0 and 2 ms for the PAN acquisitions, that is lower than 30 ms for the color-mode acquisitions and the few seconds for stellar observations that will be used in the inflight calibrations.

IT has been calculated using the radiometric model of SIMBIO-SYS (Slemer et al. 2018), which takes into account the Hapke reflectance model (Hapke et al. 2012) with parameters calculated by Domingue et al. (2016) for the Mercury surface. To have a complete simulation of the nominal configuration, different repetition times were used in the range between 1 s and 4 s for the color mode and between 7 s and 15 s for the global mapping.

10.3 VIHI Results

The VIHI spectrometer performed a number of measurements to confirm its functionality and its performance after launch. We could not perform a full set of calibration measure-

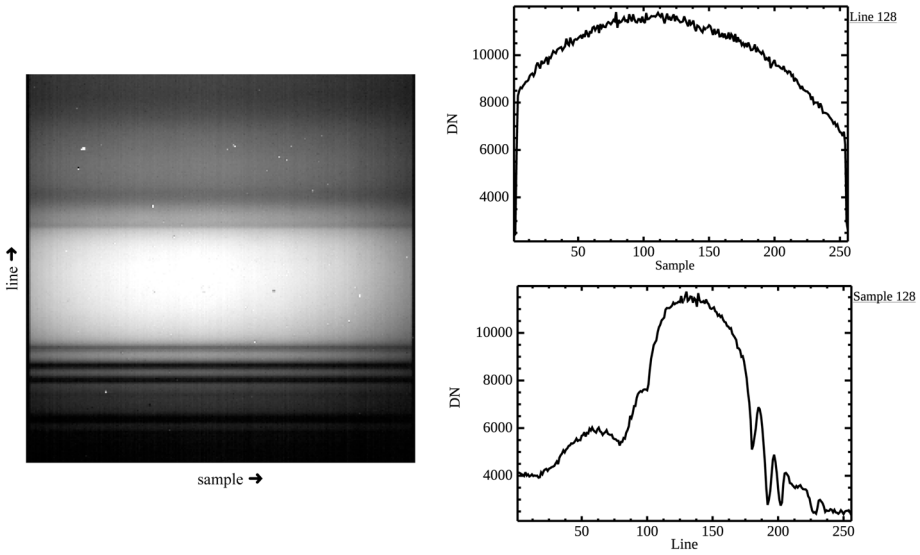

Fig. 36 VIHI internal calibration lamp signal. The image of the Focal Plane (left) shows spectral information in the vertical direction and spatial information in the horizontal direction. Two profiles show spatial variability (top right) across the FoV and the spectrum (bottom right) from 400 nm (band 255) to 2000 nm (band 0)

ments as the specific configuration of the spacecraft during cruise prevents the observation of external sources (the FoVs of the SIMBIO-SYS channels are blocked by the presence of the Mercury Transfer Module), but, due to the presence of the shutter and of the internal calibration unit, we were able to measure the dark current and the internal calibration source signals and compare them to those measured during pre-launch calibrations. VIHI also operated, along with the other channels, to verify interoperability in various configurations. The interoperability results are consistent with expectations and shall not be described here.

10.3.1 Internal Calibration

We performed the first in-flight run of the calibration routine on 12 December 2018. The in-flight calibration signal of the lamp source is shown in Fig. 36.

The signal distribution across the FoV is shown in Fig. 37 and displays a darkening at the edges of the FoV consistent with the ground observations. The observed darkening along the spatial direction is the result of a trade-off performed during the mounting and alignment of the two independent sources (Lamp and LED). The selected alignment maximizes the signal of the two sources. At any rate, the resulting signal in the full FoV and in the full spectral range for both sources is more than adequate to meet the goals of the internal calibration. The spectrum, reported in Fig. 37, clearly displays the reference absorption bands introduced by the Didymium filter deposited on the elliptic window of the lamp. The NECP measurements have shown a discrepancy of the signal measured during pre-launch tests (Filacchione et al. 2017), as reported in Fig. 37; the signal measured in flight is about 30% higher than the one on ground for the same integration time and current of the lamp. This ratio is approximately constant within the full FoV for a given wavelength. As described in the previous section, to avoid moving parts and to guarantee that all the optical elements in the VIHI optical path are tested, most of the signal (about 92%) from the calibration sources is lost into

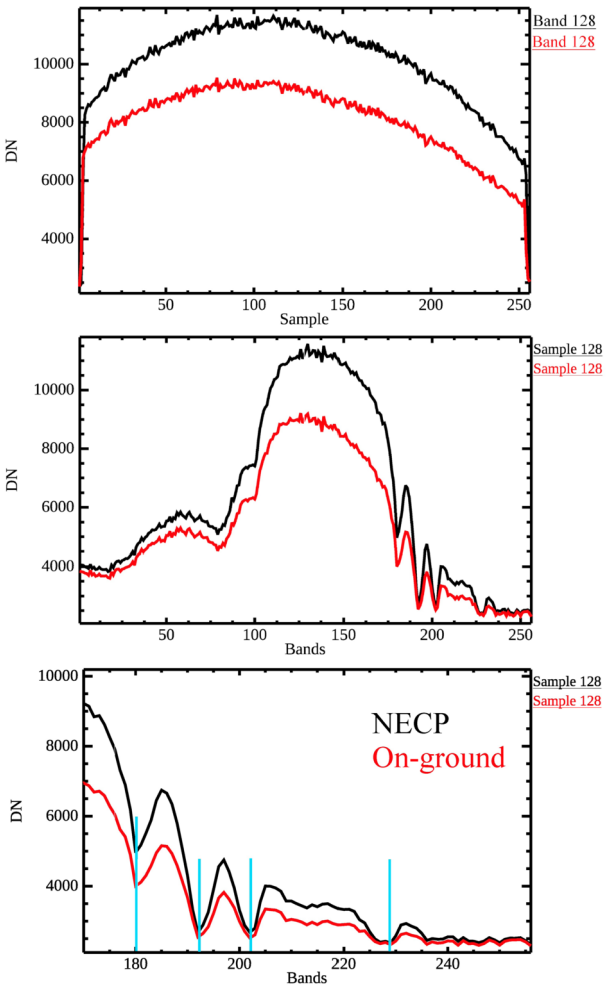

Fig. 37 The VIHI spectral response verification. The comparisons between the NECP tests (top and middle, black lines) and the on-ground ones (red lines). The two profiles show spatial variability (top) across the FoV and the spectrum (central), from 400 nm (band 255) to 2000 nm (band 0). A spectral profile zoom above the constant position of the Didymium filter absorption bands is also shown before and after launch (bottom)

space. On ground, the configuration was such that the channel FoV was unobstructed; but, in the current inflight configuration, VIHI's boresight, after mating the MPO to the MTM, is screened by a baffle cover (to prevent contaminants entering VIHI's FoV during launch and cruise). In this case, the radiation from the source is diffusively reflected inside the instrument, and part of the light, after multiple reflections, is able to re-enter the boresight of the VIHI channel. This is the most probable cause of the observed signal increase. On the other hand, the reference spectral absorptions of the Didymium filter of the lamp are stable on the same bands (see Fig. 37), an indication that VIHI spectral response has not changed after the launch.

A similar comparison has been performed also on the LED source signal and is reported in Figs. 38 and 39. Figure 38 shows the spectral distribution of the LED signal, showing that emission is limited to about 600 nm. In this case, we note a reduced darkening of the signal at the edges of the FoV and also that the on-ground and inflight performances are fairly similar in intensity. In the case of the LED, the spectral registration is verified using the spectral position of the LED features: two strong emission peaks at $\lambda = 0.451$ and 0.551 μm are

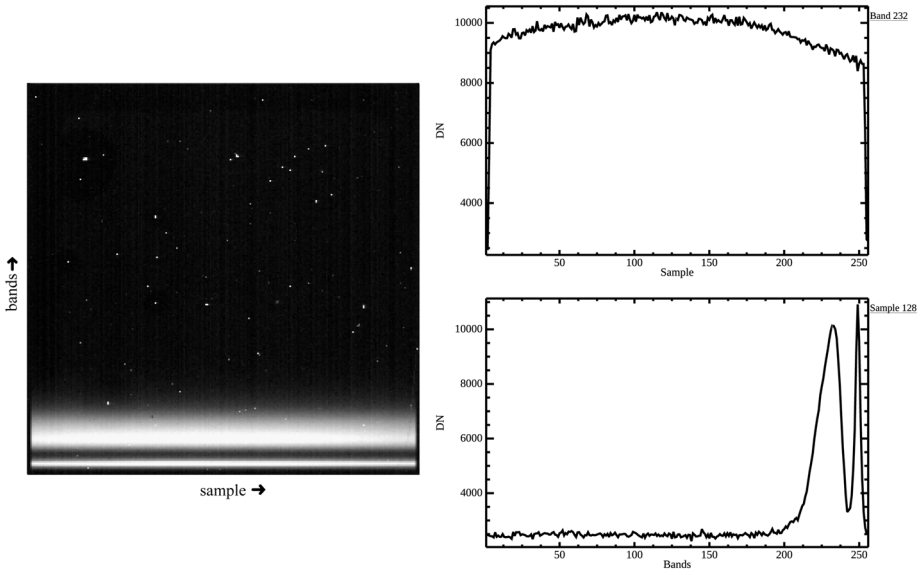

Fig. 38 The VIHI internal calibration LED source signal measured during commissioning: the signal on the detector frame (left, spectral information along the vertical direction and spatial information along the horizontal direction) and the spatial variability across the FoV (top right) and the spectrum (bottom right) from 400 nm (band 255) to 2000 nm (band 0)

separated by a minimum at $\lambda = 0.488$ µm. The bright spot randomly distributed across the frame (Fig. 38) are single nonoperative pixels which have been assigned the saturation value.

10.3.2 Dark Current

The dark current of the channel, in the in-flight conditions, was additionally acquired and compared to the on-ground results. Two runs were performed to verify the DC behavior: the first with the shutter closed (Dark) and the second with the shutter opened (Background). Normally dark and background not necessarily return the same signal as the shutter limits the input flux to the spectrometer. However, as VIHI FoV is obstructed by the presence of the MTM spacecraft module, the two observations are indeed identical within the estimated errors. However, we report them in two separate plots for future comparisons during the operative phases at Mercury, when the MTM obstruction will be removed.

We measured the DC for seven integration times: 0.2, 10, 40, 50, 70, 100, 200 ms and in the following thermal conditions: FPA temperature 215 K, spectrometer temperature 225 K, and PE temperature 284-286 K. The analysis of the dark signal is shown in Fig. 40. The mean signal on the detector shows the effect of the noise with fluctuations increasing with integration time. The angular coefficients of the best linear fits representing the dark-current signal rate for a given operating temperature of the detector is 22.35 DN/ms. The value obtained in flight is, as expected, in good agreement with the measurements performed during the on-ground calibration at 210, 220, and 225 K (Fig. 41).

10.4 Inter-Channel Tests

To verify the real capability of the interoperability of the three channels, three types of tests were prepared:

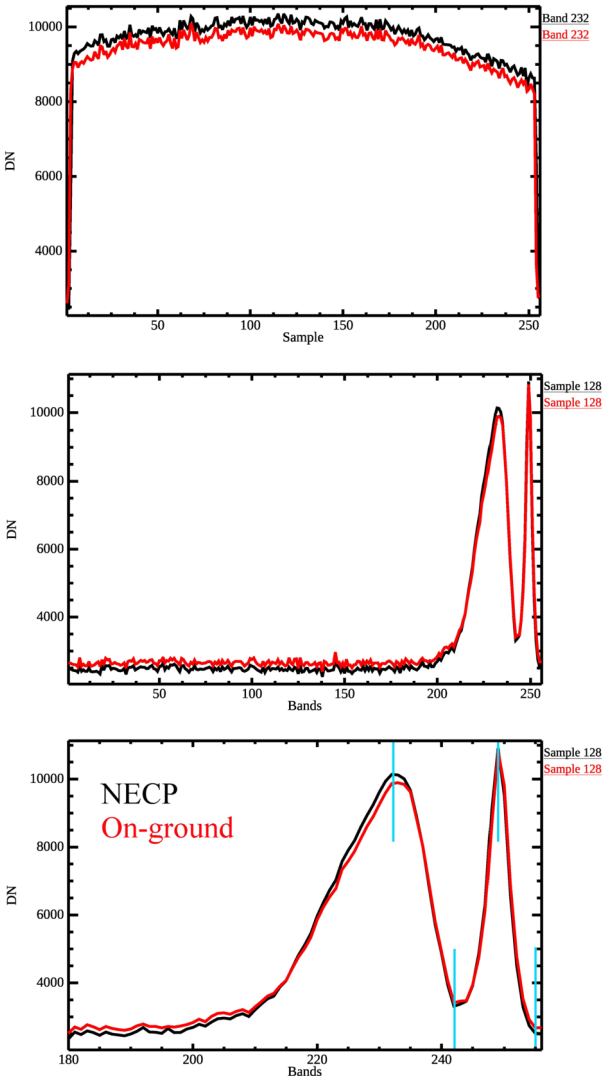

Fig. 39 Comparison between the VIHI internal calibration LED source signal measured during commissioning (black lines) and in on-ground tests (red lines). Spatial variability across the FoV (top) and the spectrum (middle) from 400 nm (band 255) to 2000 nm (band 0), as well as a spectral profile zoom showing the emission peaks of the LED as compared to the ground measurements (bottom)

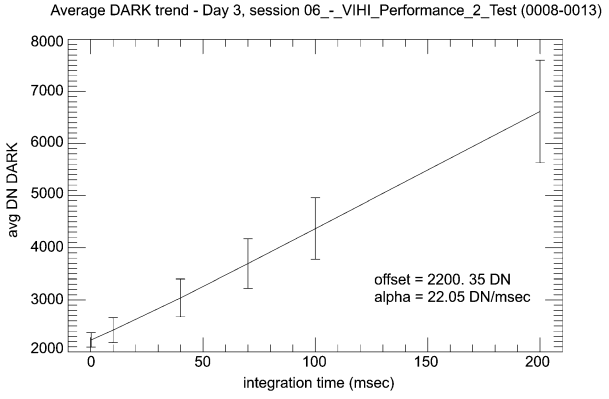

Fig. 40 The VIHI dark-current signal vs. integration time

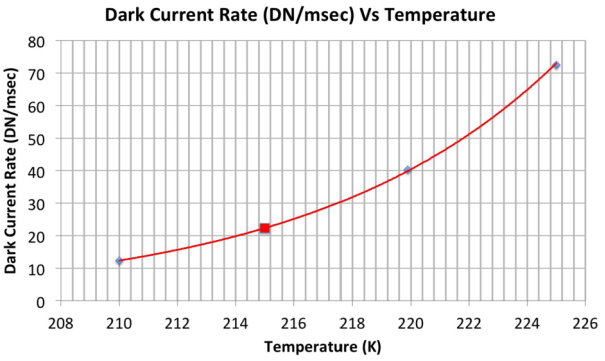

Fig. 41 The VIHI dark-current rate vs. focal-plane temperature. The in-flight value is reported in red, while the cyan losanges represent the ground calibration measurements

– Maximum stress test: the aim of this test is to command in science mode all the three channels of SIMBIO-SYS in a configuration that stresses at maximum all the units (i.e., PE and ME) involved during acquisitions;
– Maximum data-rate test: the aim of this test is to command in science mode all the three channels conveniently configured to evaluate ME behavior during acquisitions at maximum data rate;
– Orbit test: the aim of this test is to command, in science mode, all the three channels configured in the primary operation mode of global mapping phase.

In the following subsections, the obtained results for each test are reported and discussed.

10.4.1 Max Stress Test

This test was performed by putting each channel in continuous science acquisition for 10 minutes with the following configurations:

– HRIC, acquisition of an area of 512×512 pixels with 8×8 binning, ibr = 63 and RT 0.5 s;
– STC, acquisitions in CM with 3.9375 bit/px and RT 0.2 s;
– VIHI, full-frame acquisition with dark subtraction and RT 0.04 s.

The test was executed with no evidence of errors indicating that the system (i.e., ME) is capable of managing the operability of all the channels even in such a stressing configuration. The only drawback came from the fact that some of the STC data were lost due to errors in the Solid State Mass Memory management.

10.4.2 Data Rate Stress Test

This test was performed putting each channel in continuous science acquisition for 1 min with the following configurations:

– HRIC, PAN acquisition with 3.9375 bit/px and RT 1.115 s;
– STC, acquisitions in CM with 3.9375 bit/px and RT 0.2 s;
– VIHI, full-frame acquisition with 7 bit/px and RT 0.04 s.

The test was executed with no evidence of errors indicating that the system (i.e., ME) is capable of managing the operability of all the channels when producing their maximum data rate.

10.4.3 Orbit Test

This test was performed simulating a nominal orbit acquiring images with all the three channels as follows:

- HRIC acquired images in target mode with the PAN filter in lossy (2 bit/px) compression.
- STC acquired images continuously changing integration time, repetition time, and cross-track window for 9 different sections of orbit. It acquired in global mapping mode in lossy compression (2 bit/px), changing its cross-track window size from 128 px to 640 px.
- VIHI acquired images continuously changing integration time and repetition time for 8 different sections of orbit.

The test was executed with no evidence of errors indicating that the system (i.e., ME) is capable of operating in its primary operative mode.

11 Conclusion

SIMBIO-SYS is a suite composed by three channels, the high-resolution camera (HRIC), the stereo camera (STC), and the visible and near-infrared hyperspectral imager (VIHI), sharing the same main electronics (ME). Each channel has been calibrated at channel level in Leonardo SpA, the prime industrial contractor, and at system level in Orsay in the facility of the Institut de Astrophysique Spatial. The on-ground calibrations allowed to determine the performance of the instrument demonstrating that it satisfies the scientific requirements reported in the former documents, at mission level, and discussed in the design phase. The HRIC calibration has been demanding because of the long focal length that will allow to obtain high-resolution images of the Mercury surface, at best with 6 m/pixel. The results on accurately determining the detector performance have been promising considering the details we want to study on the planet. The STC calibration has been long and partially new, as it has been optically calibrated, as a usual optical head, and stereo validated because of the new stereo acquisition introduced, based on the push frame. The measured DTM accuracy is better than the requirement defined in the design phase. The VIHI calibration has been complex due to the wide spectral range of the detector performance from 400 to 2000 nm. In particular, the measurements of the internal calibration unit, composed of an IR lamp and a LED, have been very accurate. The internal calibration is crucial for the IR observations that will allow new discoveries on the surface composition.

The on-ground calibrations showed that most of the scientific requirements reported in the former documents, at mission level, and discussed in the design phase, at instrument level, will be satisfied. In some cases, the performance appears better than expected, as, for instance, for the global DTM and the DTM quality (Re et al. 2017).

The results of the first commissioning (NECP) have been positive, confirming what we have measured during the on-ground calibrations, taking into account that the instrument will not see light before the insertion in orbit around Mercury in the beginning of 2026. Minor adjustments of the onboard software will be applied during future upload.

In conclusion, it is reasonable to report a comparison between the MESSENGER observations, obtained by the cameras and the visible-NIR spectrometer, and the measurements that will be performed by SIMBIO-SYS on the Mercury surface.

MESSENGER has been in orbit around the planet for 4 years (2011-2015), providing global mapping and high-resolution images allowing to discover new surface features and processes that were not expected. SIMBIO-SYS will improve the resolution and coverage

Table 18 Comparison between the mapping performances of the MESSENGER cameras (MDIS) and laser altimeter (MLA) and SIMBIO-SYS, showing the percentages of the surface covered

Instrument	High res. coverage	Mapping	DTM	Composition	Note
MDIS		62.5%			(50-120 m/px)
MDIS 3-color		12%			<120 m/px
MDIS	2%				5-12 m/px, Northern hemisphere
MDIS (USGS)		100%	665 m		
MDIS (DLR)		regional mapping	222 m		
MLA		Northern hemisphere	665 m		250 m at North Pole
STC		100%			50-120 m/px
STC		100%	<120 m		
STC 3-color		20%			<120 m/px
HRIC	20%				5-12 m/px
VIHI		100%		400-2000 nm	at 480 m/px
VIHI	20%			400-2000 nm	at 120 m/px

Table 19 Comparison between MASCS-VIRS and SIMBIOSYS-VIHI spectrometer performances

Parameter	MASCS-VIRS	SIMBIOSYS-VIHI
Telescope Focal Length (mm)	257.6	160
Aperture (mm)	50.3 × 52.8	25
Grating (lines/mm)	100	62
Dispersion (nm/mm)	50	156
Detector	1D 512 px InGaAs	2D 512 × 512 HgCdTe
Pixel pitch (μm)	50 × 2500	40 × 40
Spectral Range (μm)	0.3-1.45	0.4-2.0
Spectral Sampling (nm/band)	5	6.25
FoV (deg)	0.023 (circular)	$3.67 \times 1.43 \cdot 10^{-2}$
IFoV (deg)	0.023 (circular)	$1.43 \cdot 10^{-2}$ (square)
Responsivity (DN m^2 μm sr/(W s)) at 0.5 μm	13	500
Responsivity (DN m^2 μm sr/(W s)) at 1.0 μm	5	1500
Responsivity (DN m^2 μm sr/(W s)) at 1.5 μm	3.5	1500
Peak Responsivity (DN m^2 μm sr/(W s))	19 (at 0.45 μm)	1800 (at 1.25 μm)

allowing to discover new features and allowing to obtain a better statistical distribution. Tables 18 and 19 report a comparison between SIMBIO-SYS and the MESSENGER instruments devoted to remote sensing measurements.

Acknowledgements We gratefully acknowledge funding from the Italian Space Agency (ASI) under ASI-INAF agreement 2017-47-H.0. The SIMBIO-SYS instrument has been developed by Leonardo under ASI contract I/054/10/0.

Publisher's Note Springer Nature remains neutral with regard to jurisdictional claims in published maps and institutional affiliations.

Open Access This article is licensed under a Creative Commons Attribution 4.0 International License, which permits use, sharing, adaptation, distribution and reproduction in any medium or format, as long as you give appropriate credit to the original author(s) and the source, provide a link to the Creative Commons licence, and indicate if changes were made. The images or other third party material in this article are included in the article's Creative Commons licence, unless indicated otherwise in a credit line to the material. If material is not included in the article's Creative Commons licence and your intended use is not permitted by statutory regulation or exceeds the permitted use, you will need to obtain permission directly from the copyright holder. To view a copy of this licence, visit http://creativecommons.org/licenses/by/4.0/.

References

A. Adriani, G. Filacchione, T. Di Iorio, D. Turrini, R. Noschese, A. Cicchetti, D. Grassi, A. Mura, G. Sindoni, M. Zambelli, JIRAM, the Jovian infrared auroral mapper. Space Sci. Rev. **213**(1–4), 393–446 (2017). https://doi.org/10.1007/s11214-014-0094-y

F. Altieri, G. Filacchione, F. Capaccioni, C. Carli, M. Dami, L. Tommasi, G. Aroldi, D. Borrelli, A. Barbis, M. Baroni, The pre-launch characterization of SIMBIO-SYS/VIHI imaging spectrometer for the BepiColombo mission to Mercury. II. Spectral calibrations. Rev. Sci. Instrum. **88**(9), 094503 (2017). https://doi.org/10.1063/1.4996857

E. Ammannito, G. Filacchione, A. Coradini, F. Capaccioni, G. Piccioni, M.C. de Sanctis, M. Dami, A. Barbis, On-ground characterization of Rosetta/VIRTIS-M. I. Spectral and geometrical calibrations. Rev. Sci. Instrum. **77**(9), 093109 (2006). https://doi.org/10.1063/1.2349308

M.E. Banks, Z. Xiao, T.R. Watters, R.G. Strom, S.E. Braden, C.R. Chapman, S.C. Solomon, C. Klimczak, P.K. Byrne, Duration of activity on lobate-scarp thrust faults on Mercury. J. Geophys. Res., Planets **120**(11), 1751–1762 (2015). https://doi.org/10.1002/2015JE004828

M. Barilli, A. Bartoli, M. Dami, E. Flamini, R. Formaro, F. Grifoni, F. Longo, C. Pompei, An un-obscured four spherical mirrors based" collimator as a tradeoff solution for the Optical Ground Support Equipment (OGSE) of the High Resolution Camera (HRIC) of Simbio-Sys, in *Proceedings of SPIE*. Society of Photo-Optical Instrumentation Engineers (SPIE) Conference Series, vol. 8446 (2012), p. 84463. https://doi.org/10.1117/12.925954

S. Besse, A. Doressoundiram, J. Benkhoff, Spectroscopic properties of explosive volcanism within the Caloris basin with MESSENGER observations. J. Geophys. Res., Planets **120**(12), 2102–2117 (2015). https://doi.org/10.1002/2015JE004819

M. Beuthe, B. Charlier, O. Namur, A. Rivoldini, T. Van Hoolst, Mercury's crustal thickness correlates with lateral variations in mantle melt production. Geophys. Res. Lett. **47**(9), e2020GL087261 (2020). https://doi.org/10.1029/2020GL087261

D.T. Blewett, N.L. Chabot, B.W. Denevi, C.M. Ernst, J.W. Head, N.R. Izenberg, S.L. Murchie, S.C. Solomon, L.R. Nittler, T.J. McCoy, Z. Xiao, D.M.H. Baker, C.I. Fassett, S.E. Braden, J. Oberst, F. Scholten, F. Preusker, D.M. Hurwitz, Hollows on Mercury: MESSENGER evidence for geologically recent volatile-related activity. Science **333**(6051), 1856 (2011). https://doi.org/10.1126/science.1211681

D.T. Blewett, C.L. Levy, N.L. Chabot, B.W. Denevi, C.M. Ernst, S.L. Murchie, Phase-ratio images of the surface of Mercury: evidence for differences in sub-resolution texture. Icarus **242**, 142–148 (2014). https://doi.org/10.1016/j.icarus.2014.08.024

S.E. Braden, M.S. Robinson, Relative rates of optical maturation of regolith on Mercury and the Moon. J. Geophys. Res., Planets **118**(9), 1903–1914 (2013). https://doi.org/10.1002/jgre.20143

Bunce et al., Space Sci. Rev. (2020, this issue)

P.K. Byrne, C. Klimczak, D.A. Williams, D.M. Hurwitz, S.C. Solomon, J.W. Head, F. Preusker, J. Oberst, An assemblage of lava flow features on Mercury. J. Geophys. Res., Planets **118**(6), 1303–1322 (2013). https://doi.org/10.1002/jgre.20052

P.K. Byrne, C. Klimczak, A.M. Celâl Şengör, S.C. Solomon, T.R. Watters, S.A. Hauck II, Mercury's global contraction much greater than earlier estimates. Nat. Geosci. **7**(4), 301–307 (2014). https://doi.org/10.1038/ngeo2097

P.K. Byrne, L.R. Ostrach, C.I. Fassett, C.R. Chapman, B.W. Denevi, A.J. Evans, C. Klimczak, M.E. Banks, J.W. Head, S.C. Solomon, Widespread effusive volcanism on Mercury likely ended by about 3.5 Ga. Geophys. Res. Lett. **43**(14), 7408–7416 (2016). https://doi.org/10.1002/2016GL069412

F. Capaccioni, M.C. de Sanctis, G. Filacchione, G. Piccioni, E. Ammannito, L. Tommasi, I. Ficai Veltroni, M. Cosi, S. Debei, L. Calamai, VIS-NIR imaging spectroscopy of Mercury's surface: SIMBIO-SYS/VIHI experiment onboard the BepiColombo. IEEE Trans. Geosci. Remote Sens. **48**, 3932–3940 (2010). https://doi.org/10.1109/TGRS.2010.2051676

F. Capaccioni, G. Filacchione, G. Piccioni, M. Dami, L. Tommasi, A. Barbis, I. Ficai-Veltroni, Pre-launch calibrations of the Vis-IR Hyperspectral Imager (VIHI) onboard BepiColombo, the ESA mission to Mercury, in *Proceedings of SPIE*. Society of Photo-Optical Instrumentation Engineers (SPIE) Conference Series, vol. 8867 (2013), p. 886704. https://doi.org/10.1117/12.2024142

C. Carli, T.L. Roush, G. Pedrazzi, F. Capaccioni, Visible and Near-Infrared (VNIR) reflectance spectroscopy of glassy igneous material: spectral variation, retrieving optical constants and particle sizes by Hapke model. Icarus **266**, 267–278 (2016). https://doi.org/10.1016/j.icarus.2015.10.032

C. Carli, G. Pratesi, V. Moggi-Cecchi, F. Zambon, F. Capaccioni, S. Santoro, Northwest Africa 6232: visible-near infrared reflectance spectra variability of an olivine diogenite. Meteorit. Planet. Sci. **53**(10), 2228–2242 (2018). https://doi.org/10.1111/maps.13056

N.L. Chabot, E.A. Wollack, R.L. Klima, M.E. Minitti, Experimental constraints on Mercury's core composition. Earth Planet. Sci. Lett. **390**, 199–208 (2014). https://doi.org/10.1016/j.epsl.2014.01.004

N.L. Chabot, E.E. Shread, J.K. Harmon, Investigating Mercury's South polar deposits: Arecibo radar observations and high-resolution determination of illumination conditions. J. Geophys. Res., Planets **123**(2), 666–681 (2018). https://doi.org/10.1002/2017JE005500

D. Claus, A.W. Fitzgibbon, A rational function lens distortion model for general cameras, in *2005 IEEE Computer Society Conference on Computer Vision and Pattern Recognition (CVPR'05)*, vol. 1 (IEEE Press, New York, 2005), pp. 213–219

F. Cucciarre', Numerical and experimental methods for design and test of units and devices on BepiColombo mission. PhD thesis, University of Padova (2013)

V. Da Deppo, G. Naletto, G. Cremonese, L. Calamai, Optical design of the single-detector planetary stereo camera for the BepiColombo European Space Agency mission to Mercury. Appl. Opt. **49**(15), 2910 (2010). https://doi.org/10.1364/AO.49.002910

V. Da Deppo, G. Cremonese, G. Naletto, Ghost images determination for the stereoscopic imaging channel of SIMBIOSYS for the BepiColombo ESA mission, in *Proceedings of SPIE*. Society of Photo-Optical Instrumentation Engineers (SPIE) Conference Series, vol. 8167 (2011), p. 81671. https://doi.org/10.1117/12.896896

V. Da Deppo, E. Martellato, G. Rossi, G. Naletto, V. Della Corte, F. Capaccioni, G. Filacchione, M. Zusi, P. Palumbo, G. Aroldi, M. Baroni, D. Borrelli, L. Tommasi, M. Dami, I. Ficai Veltroni, E. Flamini, G. Cremonese, Characterization of the integrating sphere for the on-ground calibration of the SIMBIOSYS instrument for the BepiColombo ESA mission, in *Proceedings of SPIE*. Society of Photo-Optical Instrumentation Engineers (SPIE) Conference Series, vol. 9143 (2014), p. 914344. https://doi.org/10.1117/12.2057349

V. Da Deppo, E. Simioni, G. Naletto, G. Cremonese, Distortion definition and correction in off-axis systems, in *Proceedings of SPIE*. Society of Photo-Optical Instrumentation Engineers (SPIE) Conference Series, vol. 9626 (2015), p. 962634. https://doi.org/10.1117/12.2191332

V. Da Deppo, E. Pace, G. Morgante, M. Focardi, M. Terraneo, F. Zocchi, G. Bianucci, G. Micela, A prototype for the primary mirror of the ESA ARIEL mission: design and development of an off-axis 1-m diameter aluminum mirror for infrared space applications, in *Proceedings of SPIE*. Society of Photo-Optical Instrumentation Engineers (SPIE) Conference Series, vol. 10706 (2018), p. 1070632. https://doi.org/10.1117/12.2313392

V. Della Corte, P. Palumbo, M. Zusi, M. Baroni, G. Cremonese, R. Mugnuolo, Performances of the SIMBIO-SYS high resolution imaging channel on board BepiColombo/ESA spacecraft channel performance parameters as derived by on ground calibration measurements, in *2018 5th IEEE International Workshop on Metrology for AeroSpace (MetroAeroSpace)* (IEEE Press, New York, 2018), pp. 516–520

B.W. Denevi, C.M. Ernst, H.M. Meyer, M.S. Robinson, S.L. Murchie, J.L. Whitten, J.W. Head, T.R. Watters, S.C. Solomon, L.R. Ostrach, C.R. Chapman, P.K. Byrne, C. Klimczak, P.N. Peplowski, The distribution and origin of smooth plains on Mercury. J. Geophys. Res., Planets **118**(5), 891–907 (2013). https://doi.org/10.1002/jgre.20075

B.W. Denevi, N.L. Chabot, S.L. Murchie, K.J. Becker, D.T. Blewett, D.L. Domingue, C.M. Ernst, C.D. Hash, S.E. Hawkins, M.R. Keller, N.R. Laslo, H. Nair, M.S. Robinson, F.P. Seelos, G.K. Stephens, F.S. Turner, S.C. Solomon, Calibration, projection, and final image products of MESSENGER's Mercury dual imaging system. Space Sci. Rev. **214**(1), 2 (2018). https://doi.org/10.1007/s11214-017-0440-y

G. Di Achille, C. Popa, M. Massironi, E. Mazzotta Epifani, M. Zusi, G. Cremonese, P. Palumbo, Mercury's radius change estimates revisited using MESSENGER data. Icarus **221**(1), 456–460 (2012). https://doi.org/10.1016/j.icarus.2012.07.005

D.L. Domingue, B.W. Denevi, S.L. Murchie, C.D. Hash, Application of multiple photometric models to disk-resolved measurements of Mercury's surface: insights into Mercury's regolith characteristics. Icarus **268**, 172–203 (2016). https://doi.org/10.1016/j.icarus.2015.11.040

C.I. Fassett, J.W. Head, S.J. Kadish, E. Mazarico, G.A. Neumann, D.E. Smith, M.T. Zuber, Lunar impact basins: stratigraphy, sequence and ages from superposed impact crater populations mea-

sured from Lunar Orbiter Laser Altimeter (LOLA) data. J. Geophys. Res., Planets **117**, 00 (2012). https://doi.org/10.1029/2011JE003951
E.R. Fegan, D.A. Rothery, S. Marchi, M. Massironi, S.J. Conway, M. Anand, Late movement of basin-edge lobate scarps on Mercury. Icarus **288**, 226–234 (2017). https://doi.org/10.1016/j.icarus.2017.01.005
G. Filacchione, E. Ammannito, A. Coradini, F. Capaccioni, G. Piccioni, M.C. de Sanctis, M. Dami, A. Barbis, On-ground characterization of Rosetta/VIRTIS-M. II. Spatial and radiometric calibrations. Rev. Sci. Instrum. **77**(10), 103106 (2006). https://doi.org/10.1063/1.2360786
G. Filacchione, F. Capaccioni, F. Altieri, C. Carli, I. Ficai Veltroni, M. Dami, L. Tommasi, G. Aroldi, D. Borrelli, A. Barbis, The pre-launch characterization of SIMBIO-SYS/VIHI imaging spectrometer for the BepiColombo mission to Mercury. I. Linearity, radiometry, and geometry calibrations. Rev. Sci. Instrum. **88**(9), 094502 (2017). https://doi.org/10.1063/1.4989968
G. Filacchione, F. Capaccioni, F. Altieri, C. Carli, L. Tommasi, I. Ficai Veltroni, M. Dami, G. Aroldi, D. Borrelli, A. Barbis, The measurement of the noise-equivalent spectral radiance of SIMBIO-SYS/VIHI spectrometer, in *5th IEEE International Workshop on Metrology for AeroSpace (MetroAeroSpace)*, Rome (2018), pp. 252–256
E. Friso, Thermal effects reduction techniques for the SIMBIO-SYS scientific suite of BepiColombo mission. PhD thesis, University of Padova (2010)
V. Galluzzi, G. Di Achille, L. Ferranti, C. Popa, P. Palumbo, Faulted craters as indicators for thrust motions on Mercury. Geol. Soc. (Lond.) Spec. Publ. **401**(1), 313 (2015). https://doi.org/10.1144/SP401.17
V. Galluzzi, L. Ferranti, M. Massironi, L. Giacomini, L. Guzzetta, P. Palumbo, Structural analysis of the Victoria quadrangle fault systems on Mercury: timing, geometries, kinematics, and relationship with the High-Mg region. J. Geophys. Res., Planets **124**(10), 2543–2562 (2019). https://doi.org/10.1029/2019JE005953
A. Genova, S. Goossens, E. Mazarico, F.G. Lemoine, G.A. Neumann, W. Kuang, T.J. Sabaka, S.A. Hauck, D.E. Smith, S.C. Solomon, M.T. Zuber, Geodetic evidence that Mercury has a solid inner core. Geophys. Res. Lett. **46**(7), 3625–3633 (2019). https://doi.org/10.1029/2018GL081135
L. Giacomini, M. Massironi, S. Marchi, C.I. Fassett, G. Di Achille, G. Cremonese, Age dating of an extensive thrust system on Mercury: implications for the planet's thermal evolution. Geol. Soc. (Lond.) Spec. Publ. **401**(1), 291 (2015). https://doi.org/10.1144/SP401.21
T.A. Goudge, J.W. Head, L. Kerber, D.T. Blewett, B.W. Denevi, D.L. Domingue, J.J. Gillis-Davis, K. Gwinner, J. Helbert, G.M. Holsclaw, N.R. Izenberg, R.L. Klima, W.E. McClintock, S.L. Murchie, G.A. Neumann, D.E. Smith, R.G. Strom, Z. Xiao, M.T. Zuber, S.C. Solomon, Global inventory and characterization of pyroclastic deposits on Mercury: new insights into pyroclastic activity from MESSENGER orbital data. J. Geophys. Res., Planets **119**(3), 635–658 (2014). https://doi.org/10.1002/2013JE004480
B. Hapke, Bidirectional reflectance spectroscopy. 5. The coherent backscatter opposition effect and anisotropic scattering. Icarus **157**(2), 523–534 (2002). https://doi.org/10.1006/icar.2002.6853
B. Hapke, Bidirectional reflectance spectroscopy 7. The single particle phase function hockey stick relation. Icarus **221**(2), 1079–1083 (2012). https://doi.org/10.1016/j.icarus.2012.10.022
B. Hapke, B. Denevi, H. Sato, S. Braden, M. Robinson, The wavelength dependence of the lunar phase curve as seen by the Lunar Reconnaissance Orbiter wide-angle camera. J. Geophys. Res., Planets **117**, 00 (2012). https://doi.org/10.1029/2011JE003916
S.A. Hauck, J.-L. Margot, S.C. Solomon, R.J. Phillips, C.L. Johnson, F.G. Lemoine, E. Mazarico, T.J. McCoy, S. Padovan, S.J. Peale, M.E. Perry, D.E. Smith, M.T. Zuber, The curious case of Mercury's internal structure. J. Geophys. Res., Planets **118**(6), 1204–1220 (2013). https://doi.org/10.1002/jgre.20091
J.W. Head, C.R. Chapman, R.G. Strom, C.I. Fassett, B.W. Denevi, D.T. Blewett, C.M. Ernst, T.R. Watters, S.C. Solomon, S.L. Murchie, L.M. Prockter, N.L. Chabot, J.J. Gillis-Davis, J.L. Whitten, T.A. Goudge, D.M.H. Baker, D.M. Hurwitz, L.R. Ostrach, Z. Xiao, W.J. Merline, L. Kerber, J.L. Dickson, J. Oberst, P.K. Byrne, C. Klimczak, L.R. Nittler, Flood volcanism in the northern high latitudes of Mercury revealed by MESSENGER. Science **333**(6051), 1853 (2011). https://doi.org/10.1126/science.1211997
J. Helbert, A. Maturilli, M. D'Amore, Visible and near-infrared reflectance spectra of thermally processed synthetic sulfides as a potential analog for the hollow forming materials on Mercury. Earth Planet. Sci. Lett. **369**, 233–238 (2013). https://doi.org/10.1016/j.epsl.2013.03.045
Y. Hello, J.F. Roig, A. Doressoundiram, F. Capaccioni, M. Cosi, L. Tommasi, E. Beuville, E. Corrales, R. Peralta, C. Rabkin, Visible and near infrared detector for BepiColombos spectrometer VIHI, in *EAS Publications Series*, vol. 37, ed. by P. Kern (2009), pp. 391–395. https://doi.org/10.1051/eas/0937045
Hiesinger et al., Space Sci. Rev. (2020, this issue)
Hussmann et al., Space Sci. Rev. (2020, this issue)
Iess et al., Space Sci. Rev. (2020, this issue)
N.R. Izenberg, R.L. Klima, S.L. Murchie, D.T. Blewett, G.M. Holsclaw, W.E. McClintock, E. Malaret, C. Mauceri, F. Vilas, A.L. Sprague, J. Helbert, D.L. Domingue, J.W. Head, T.A. Goudge, S.C. Solomon,

C.A. Hibbitts, M.D. Dyar, The low-iron, reduced surface of Mercury as seen in spectral reflectance by MESSENGER. Icarus **228**, 364–374 (2014). https://doi.org/10.1016/j.icarus.2013.10.023

L. Kerber, J.W. Head, S.C. Solomon, S.L. Murchie, D.T. Blewett, L. Wilson, Explosive volcanic eruptions on Mercury: eruption conditions, magma volatile content, and implications for interior volatile abundances. Earth Planet. Sci. Lett. **285**(3–4), 263–271 (2009). https://doi.org/10.1016/j.epsl.2009.04.037

C. Klimczak, P.K. Byrne, S.C. Solomon, A rock-mechanical assessment of Mercury's global tectonic fabric. Earth Planet. Sci. Lett. **416**, 82–90 (2015). https://doi.org/10.1016/j.epsl.2015.02.003

Y. Langevin, O. Forni, Image and spectral image compression for four experiments on the ROSETTA and Mars Express missions of ESA, in *Proceedings of SPIE*, ed. by A.G. Tescher. Society of Photo-Optical Instrumentation Engineers (SPIE) Conference Series, vol. 4115 (2000), pp. 364–373. https://doi.org/10.1117/12.411561

D.J. Lawrence, W.C. Feldman, J.O. Goldsten, S. Maurice, P.N. Peplowski, B.J. Anderson, D. Bazell, R.L. McNutt, L.R. Nittler, T.H. Prettyman, D.J. Rodgers, S.C. Solomon, S.Z. Weider, Evidence for water ice near Mercury's North Pole from MESSENGER neutron spectrometer measurements. Science **339**(6117), 292 (2013). https://doi.org/10.1126/science.1229953

D.J. Lawrence, W.C. Feldman, P.N. Peplowski, S.C. Solomon, The 4 June 2011 neutron event at Mercury: a defense of the solar origin hypothesis. J. Geophys. Res. Space Phys. **120**(7), 5284–5289 (2015). https://doi.org/10.1002/2015JA021069.

F. Leblanc, R.E. Johnson, Mercury exosphere I. Global circulation model of its sodium component. Icarus **209**(2), 280–300 (2010). https://doi.org/10.1016/j.icarus.2010.04.020

A. Lucchetti, M. Pajola, V. Galluzzi, L. Giacomini, C. Carli, G. Cremonese, G.A. Marzo, S. Ferrari, M. Massironi, P. Palumbo, Mercury hollows as remnants of original bedrock materials and devolatilization processes: a spectral clustering and geomorphological analysis. J. Geophys. Res., Planets **123**(9), 2365–2379 (2018). https://doi.org/10.1029/2018JE005722

C.C. Malliband, S.J. Conway, D.A. Rothery, M.R. Balme, Potential identification of downslope mass movements on Mercury driven by volatile-loss, in *Lunar and Planetary Science Conference* (2019), p. 1804

P. Mancinelli, F. Minelli, A. Mondini, C. Pauselli, C. Federico, A downscaling approach for geological characterization of the raditladi basin of mercury. Geol. Soc. (Lond.) Spec. Publ. **401**(1), 57–75 (2015). https://doi.org/10.1144/SP401.10

S. Marchi, C.R. Chapman, C.I. Fassett, J.W. Head, W.F. Bottke, R.G. Strom, Global resurfacing of Mercury 4.0-4.1 billion years ago by heavy bombardment and volcanism. Nature **499**(7456), 59–61 (2013). https://doi.org/10.1038/nature12280

J.-L. Margot, S.J. Peale, S.C. Solomon, S.A. Hauck II, F.D. Ghigo, R.F. Jurgens, M. Yseboodt, J.D. Giorgini, S. Padovan, D.B. Campbell, Mercury's moment of inertia from spin and gravity data. J. Geophys. Res., Planets **117**, 00 (2012). https://doi.org/10.1029/2012JE004161

M. Massironi, G. Di Achille, D.A. Rothery, V. Galluzzi, L. Giacomini, S. Ferrari, M. Zusi, G. Cremonese, P. Palumbo, Lateral ramps and strike-slip kinematics on Mercury. Geol. Soc. (Lond.) Spec. Publ. **401**(1), 269 (2015). https://doi.org/10.1144/SP401.16

E. Mazarico, A. Genova, S. Goossens, F.G. Lemoine, G.A. Neumann, M.T. Zuber, D.E. Smith, S.C. Solomon, The gravity field, orientation, and ephemeris of Mercury from MESSENGER observations after three years in orbit. J. Geophys. Res., Planets **119**(12), 2417–2436 (2014). https://doi.org/10.1002/2014JE004675

W.E. McClintock, M.R. Lankton, The Mercury atmospheric and surface composition spectrometer for the MESSENGER mission. Space Sci. Rev. **131**(1–4), 481–521 (2007). https://doi.org/10.1007/s11214-007-9264-5

F.M. McCubbin, K.E. Vander Kaaden, P.N. Peplowski, A.S. Bell, L.R. Nittler, J.W. Boyce, L.G. Evans, L.P. Keller, S.M. Elardo, T.J. McCoy, A low O/Si ratio on the surface of Mercury: evidence for silicon smelting? J. Geophys. Res., Planets **122**(10), 2053–2076 (2017). https://doi.org/10.1002/2017JE005367

Milillo et al., Space Sci. Rev. (2020, this issue)

R.E. Mills, J.J. Drab, A. Gin, Advanced staring Si PIN visible sensor chip assembly for Bepi-Colombo mission to Mercury, in *Proceedings of SPIE*. Society of Photo-Optical Instrumentation Engineers (SPIE) Conference Series, vol. 7439 (2009), p. 74390. https://doi.org/10.1117/12.827036

Mitrofanov et al., Space Sci. Rev. (2020, this issue)

A. Morlok, C. Hamann, D. Martin, I. Weber, K.H. Joy, H. Hiesinger, R. Wogelius, A.N. Stojic, J. Helbert, Mid-infrared spectroscopy of laser-produced basalt melts for remote sensing application. Icarus **335**, 113410 (2020). https://doi.org/10.1016/j.icarus.2019.113410

L.R. Nittler, R.D. Starr, S.Z. Weider, T.J. McCoy, W.V. Boynton, D.S. Ebel, C.M. Ernst, L.G. Evans, J.O. Goldsten, D.K. Hamara, D.J. Lawrence, R.L. McNutt, C.E. Schlemm, S.C. Solomon, A.L. Sprague, The major-element composition of Mercury's surface from MESSENGER X-ray spectrometry. Science **333**(6051), 1847 (2011). https://doi.org/10.1126/science.1211567

Orsini et al., Space Sci. Rev. (2020, this issue)

S. Padovan, M.A. Wieczorek, J.-L. Margot, N. Tosi, S.C. Solomon, Thickness of the crust of Mercury from geoid-to-topography ratios. Geophys. Res. Lett. **42**(4), 1029–1038 (2015). https://doi.org/10.1002/2014GL062487

P.N. Peplowski, D.J. Lawrence, L.G. Evans, R.L. Klima, D.T. Blewett, J.O. Goldsten, S.L. Murchie, T.J. McCoy, L.R. Nittler, S.C. Solomon, R.D. Starr, S.Z. Weider, Constraints on the abundance of carbon in near-surface materials on Mercury: results from the MESSENGER gamma-ray spectrometer. Planet. Space Sci. **108**, 98–107 (2015). https://doi.org/10.1016/j.pss.2015.01.008

E.H. Phillips, K.W.W. Sims, J. Blichert-Toft, R.C. Aster, G.A. Gaetani, P.R. Kyle, P.J. Wallace, D.J. Rasmussen, The nature and evolution of mantle upwelling at Ross Island, Antarctica, with implications for the source of HIMU lavas. Earth Planet. Sci. Lett. **498**, 38–53 (2018). https://doi.org/10.1016/j.epsl.2018.05.049

F. Poulet, J. Rodriguez-Ferreira, A. Arondel, K. Dassas, P. Eng, P. Lami, Y. Langevin, Y. Longval, P. Pradel, M. Dami, The pre-flight calibration setup of the instrument SIMBIO-SYS onboard the mission Bepi-Colombo. Planet. Space Sci. **117**, 82–95 (2015). https://doi.org/10.1016/j.pss.2015.05.013

L.M. Prockter, C.M. Ernst, B.W. Denevi, C.R. Chapman, J.W. Head, C.I. Fassett, W.J. Merline, S.C. Solomon, T.R. Watters, R.G. Strom, G. Cremonese, S. Marchi, M. Massironi, Evidence for young volcanism on Mercury from the third MESSENGER Flyby. Science **329**(5992), 668 (2010). https://doi.org/10.1126/science.1188186

Quemerais et al., Space Sci. Rev. (2020, this issue)

C. Re, E. Simioni, G. Cremonese, R. Roncella, G. Forlani, V. Da Deppo, G. Naletto, G. Salemi, DTM generation from STC-SIMBIO-SYS images, in *Proceedings of SPIE*. Society of Photo-Optical Instrumentation Engineers (SPIE) Conference Series, vol. 9528 (2015), p. 95280. https://doi.org/10.1117/12.2184745

C. Re, E. Simioni, G. Cremonese, R. Roncella, G. Forlani, Y. Langevin, V. Da Deppo, G. Naletto, G. Salemi, Effects of image compression and illumination on digital terrain models for the stereo camera of the BepiColombo mission. Planet. Space Sci. **136**, 1–14 (2017). https://doi.org/10.1016/j.pss.2016.10.018

D.A. Rothery, M. Massironi, G. Alemanno, O. Barraud, S. Besse, N. Bott, R. Brunetto, E. Bunce, P. Byrne, F. Capaccioni, M.T. Capria, C. Carli, B. Charlier, T. Cornet, G. Cremonese, M. D'Amore, M.C. De Sanctis, A. Doressoundiram, L. Ferranti, G. Filacchione, V. Galluzzi, L. Giacomini, M. Grande, L.G. Guzzetta, J. Helbert, D. Heyner, H. Hiesinger, H. Hussmann, R. Hyodo, T. Kohout, A. Kozyrev, M. Litvak, A. Lucchetti, A. Malakhov, C. Malliband, P. Mancinelli, J. Martikainen, A. Martindale, A. Maturilli, A. Milillo, I. Mitrofanov, M. Mokrousov, A. Morlok, K. Muinonen, O. Namur, A. Owens, L.R. Nittler, J.S. Oliveira, P. Palumbo, M. Pajola, D.L. Pegg, A. Penttila, R. Politi, F. Quarati, C. Re, A. Sanin, R. Schulz, C. Stangarone, A. Stojic, V. Tretiyakov, T. Vaisanen, I. Varatharajan, I. Weber, J. Wright, P. Wurz, F. Zambon, Rationale for BepiColombo studies of Mercury's surface and composition. Space Sci. Rev. **216**(4), 66 (2020). https://doi.org/10.1007/s11214-020-00694-7

D.A. Rothery, M. Massironi, Beagle rupes - evidence for a basal decollement of regional extent in Mercury's lithosphere. Icarus **209**(1), 256–261 (2010). https://doi.org/10.1016/j.icarus.2009.12.009

D.A. Rothery, R.J. Thomas, L. Kerber, Prolonged eruptive history of a compound volcano on Mercury: volcanic and tectonic implications. Earth Planet. Sci. Lett. **385**, 59–67 (2014). https://doi.org/10.1016/j.epsl.2013.10.023

A. Said, W.A. Pearlman et al., A new, fast, and efficient image codec based on set partitioning in hierarchical trees. IEEE Trans. Circuits Syst. Video Technol. **6**(3), 243–250 (1996)

H. Schleicher, G. Wiedemann, H. Wöhl, T. Berkefeld, D. Soltau, Detection of neutral sodium above Mercury during the transit on 2003 May 7. Astron. Astrophys. **425**, 1119–1124 (2004). https://doi.org/10.1051/0004-6361:20040477

E. Simioni, V. Da Deppo, G. Naletto, G. Cremonese, C. Re, Stereo camera for satellite application: a new testing method, in *Metrology for Aerospace (MetroAeroSpace)* (2014), pp. 582–587. https://doi.org/10.1109/MetroAeroSpace.2014.6865992

E. Simioni, V. Da Deppo, C. Re, G. Naletto, E. Martellato, D. Borrelli, M. Dami, G. Aroldi, I. Ficai Veltroni, G. Cremonese, Geometrical distortion calibration of the stereo camera for the BepiColombo mission to Mercury, in *Proceedings of SPIE*. Society of Photo-Optical Instrumentation Engineers (SPIE) Conference Series, vol. 9904 (2016), p. 990410. https://doi.org/10.1117/12.2232639

E. Simioni, A. De Sio, V. Da Deppo, G. Naletto, G. Cremonese, CMOS detectors: lessons learned during the STC stereo channel preflight calibration, in *Proceedings of SPIE*. Society of Photo-Optical Instrumentation Engineers (SPIE) Conference Series, vol. 10562 (2017a), p. 105622. https://doi.org/10.1117/12.2296147

E. Simioni, C. Re, V. Da Deppo, G. Naletto, D. Borrelli, M. Dami, I. Ficai Veltroni, G. Cremonese, Indoor calibration for stereoscopic camera STC: a new method, in *Proceedings of SPIE*. Society of Photo-Optical

Instrumentation Engineers (SPIE) Conference Series, vol. 10563 (2017b), p. 105634. https://doi.org/10.1117/12.2304188

E. Simioni, V. Da Deppo, C. Re, A. Slemer, M.T. Capria, I. Ficai Veltroni, D. Borrelli, M. Dami, L. Tommasi, R. Mugnuolo, M. Amoroso, F. Longo, G. Cremonese, SIMBIO-SYS/STC stereo camera calibration: geometrical distortion. Rev. Sci. Instrum. **90**(4), 043106 (2019a). https://doi.org/10.1063/1.5085710

E. Simioni, V. Da Deppo, C. Re, M.T. Capria, G. Naletto, G. Forlani, L. Tommasi, M. Dami, D. Borrelli, I.F. Veltroni et al., SIMBIOSYS-STC ready for launch: a technical recap, in *International Conference on Space Optics—ICSO 2018*, vol. 11180 (International Society for Optics, 2019b), p. 1118042.

A. Slemer, M. Zusi, E. Simioni, V. Da Deppo, C. Re, V. Della Corte, G. Filacchione, P. Palumbo, F. Capaccioni, G. Cremonese, A Mercury surface radiometric model for SIMBIO-SYS instrument suite on board of BepiColombo mission, in *Proceedings of SPIE*. Society of Photo-Optical Instrumentation Engineers (SPIE) Conference Series, vol. 10698 (2018), p. 106984. https://doi.org/10.1117/12.2314836

A. Slemer, E. Simioni, V. Da Deppo, C. Re, M. Dami, D. Borrelli, I. Ficai Veltroni, G. Aroldi, L. Tommasi, M.T. Capria, G. Naletto, R. Mugnolo, M. Amoroso, G. Cremonese, SIMBIO-SYS STC ready for the first light: the radiometric calibration, in *Proceedings of SPIE*. Society of Photo-Optical Instrumentation Engineers (SPIE) Conference Series, vol. 11180 (2019a), p. 111807. https://doi.org/10.1117/12.2536198

A. Slemer, V. Da Deppo, E. Simioni, P. Chioetto, P. Zuppella, C. Re, G. Aroldi, M. Dami, D. Borrelli, I. Ficai Veltroni, L. Tommasi, M.T. Capria, G. Naletto, R. Mugnuolo, M. Amoroso, G. Cremonese, Spectral response of the stereo imaging channel of SIMBIO-SYS on-board the ESA BepiColombo mission, in *Proceedings of SPIE*. Society of Photo-Optical Instrumentation Engineers (SPIE) Conference Series, vol. 11115 (2019b), p. 1111514. https://doi.org/10.1117/12.2528797

A. Slemer, E. Simioni, V. Da Deppo, M. Zusi, C. Re, A. Lucchetti, M. Dami, D. Borrelli, I.F. Veltroni, L. Tommasi et al., Performance evaluation of the simbio-sys stereo imaging channel on board bepicolombo/esa spacecraft. Measurement **135**, 828–835 (2019c)

A. Slemer, M. Zusi, E. Simioni, V. Da Deppo, C. Re, A. Lucchetti, V. Della Corte, G. Filacchione, P. Palumbo, F. Capaccioni, M.T. Capria, M. Amoroso, R. Mugnuolo, G. Cremonese, Development of a simulator of the SIMBIOSYS suite onboard the BepiColombo mission. Mon. Not. R. Astron. Soc. **491**(2), 1673–1689 (2020). https://doi.org/10.1093/mnras/stz3060

D.E. Smith, M.T. Zuber, R.J. Phillips, S.C. Solomon, S.A. Hauck, F.G. Lemoine, E. Mazarico, G.A. Neumann, S.J. Peale, J.-L. Margot, C.L. Johnson, M.H. Torrence, M.E. Perry, D.D. Rowlands, S. Goossens, J.W. Head, A.H. Taylor, Gravity field and internal structure of Mercury from MESSENGER. Science **336**(6078), 214 (2012). https://doi.org/10.1126/science.1218809

A. Stark, J. Oberst, F. Preusker, S.J. Peale, J.-L. Margot, R.J. Phillips, G.A. Neumann, D.E. Smith, M.T. Zuber, S.C. Solomon, First MESSENGER orbital observations of Mercury's librations. Geophys. Res. Lett. **42**(19), 7881–7889 (2015). https://doi.org/10.1002/2015GL065152

O.N. Stavroudis, L.D. Foo, System of reflective telescope baffles. Opt. Eng. **33**, 675–680 (1994). https://doi.org/10.1117/12.159338

R.J. Thomas, D.A. Rothery, S.J. Conway, M. Anand, Hollows on Mercury: materials and mechanisms involved in their formation. Icarus **229**, 221–235 (2014a). https://doi.org/10.1016/j.icarus.2013.11.018

R.J. Thomas, D.A. Rothery, S.J. Conway, M. Anand, Mechanisms of explosive volcanism on Mercury: implications from its global distribution and morphology. J. Geophys. Res., Planets **119**(10), 2239–2254 (2014b). https://doi.org/10.1002/2014JE004692

N. Thomas, G. Cremonese, R. Ziethe, M. Gerber, M. Brändli, G. Bruno, M. Erismann, L. Gambicorti, T. Gerber, K. Ghose, M. Gruber, P. Gubler, H. Mischler, J. Jost, D. Piazza, A. Pommerol, M. Rieder, V. Roloff, A. Servonet, W. Trottmann, T. Uthaicharoenpong, C. Zimmermann, D. Vernani, M. Johnson, E. Pelò, T. Weigel, J. Viertl, N. De Roux, P. Lochmatter, G. Sutter, A. Casciello, T. Hausner, I. Ficai Veltroni, V. Da Deppo, P. Orleanski, W. Nowosielski, T. Zawistowski, S. Szalai, B. Sodor, S. Tulyakov, G. Troznai, M. Banaskiewicz, J.C. Bridges, S. Byrne, S. Debei, M.R. El-Maarry, E. Hauber, C.J. Hansen, A. Ivanov, L. Keszthelyi, R. Kirk, R. Kuzmin, N. Mangold, L. Marinangeli, W.J. Markiewicz, M. Massironi, A.S. McEwen, C. Okubo, L.L. Tornabene, P. Wajer, J.J. Wray, The Colour and Stereo Surface Imaging System (CaSSIS) for the ExoMars Trace Gas Orbiter. Space Sci. Rev. **212**(3–4), 1897–1944 (2017). https://doi.org/10.1007/s11214-017-0421-1

H. Tian, Noise Analysis in CMOS image sensor. PhD thesis, Stanford University (2000)

F. Vilas, D.L. Domingue, J. Helbert, M. D'Amore, A. Maturilli, R.L. Klima, K.R. Stockstill-Cahill, S.L. Murchie, N.R. Izenberg, D.T. Blewett, W.M. Vaughan, J.W. Head, Mineralogical indicators of Mercury's hollows composition in MESSENGER color observations. Geophys. Res. Lett. **43**(4), 1450–1456 (2016). https://doi.org/10.1002/2015GL067515

T.R. Watters, K. Daud, M.E. Banks, M.M. Selvans, C.R. Chapman, C.M. Ernst, Recent tectonic activity on Mercury revealed by small thrust fault scarps. Nat. Geosci. **9**(10), 743–747 (2016). https://doi.org/10.1038/ngeo2814

S.Z. Weider, L.R. Nittler, R.D. Starr, E.J. Crapster-Pregont, P.N. Peplowski, B.W. Denevi, J.W. Head, P.K. Byrne, S.A. Hauck, D.S. Ebel, S.C. Solomon, Evidence for geochemical terranes on Mercury: global mapping of major elements with MESSENGER's X-Ray spectrometer. Earth Planet. Sci. Lett. **416**, 109–120 (2015). https://doi.org/10.1016/j.epsl.2015.01.023

S.Z. Weider, L.R. Nittler, S.L. Murchie, P.N. Peplowski, T.J. McCoy, L. Kerber, C. Klimczak, C.M. Ernst, T.A. Goudge, R.D. Starr, N.R. Izenberg, R.L. Klima, S.C. Solomon, Evidence from MESSENGER for sulfur- and carbon-driven explosive volcanism on Mercury. Geophys. Res. Lett. **43**(8), 3653–3661 (2016). https://doi.org/10.1002/2016GL068325

J. Wright, D.A. Rothery, M.R. Balme, S.J. Conway, The First Geological Map of the Hokusai Quadrangle (H05) of Mercury, in *Lunar and Planetary Science Conference* (2019), p. 1372

M. Zusi, The High Resolution Imaging Channel of the SIMBIO-SYS suite aboard the BepiColombo mission to Mercury. PhD thesis, University of Naples-Federico II (2009)

M. Zusi, L. Colangeli, P. Palumbo, E. Mazzotta Epifani, G. Marra, E. Flamini (SIMBIO-SYS International Team), Radiometric model and operation-define-tool for HRIC SIMBIO-SYS on the BepiColombo mission to Mercury. Mem. Soc. Astron. Ital. Suppl. **12**, 72 (2008)